A Search for Stop Squarks in $p\overline{p}$ Collisions at $\sqrt{s} = 1.8$TeV Utilizing the DØ Detector.

by

Carl LaVern Lundstedt

A DISSERTATION

Presented to the Faculty of

The Graduate College at the University of Nebraska

In Partial Fulfillment of Requirements

For the Degree of Doctor of Philosophy

Major: Physics and Astronomy

Under the Supervision of Professor Daniel R. Claes

Lincoln, Nebraska

December, 2001

This thesis entitled:
A Search for Stop Squarks in $p\overline{p}$ Collisions at $\sqrt{s} = 1.8$TeV Utilizing the DØ Detector.
written by Carl LaVern Lundstedt
has been approved for the Major: Physics and Astronomy

Dr. Dan Claes (Advisor)

Dr. Greg Snow

Dr. William Campbell

Dr. Edward Jones

Dr. Ronald J. Bonnstetter

Date _____

The final copy of this thesis has been examined by the signatories, and we find that both the content and the form meet acceptable presentation standards of scholarly work in the above mentioned discipline.

A Search for Stop Squarks in $p\overline{p}$ Collisions at $\sqrt{s} = 1.8$TeV Utilizing the DØ Detector.

Lundstedt, Carl LaVern (Ph. D.)

Adviser: Dr. Dan Claes (Advisor)

Reported here are the techniques and results of a search for the supersymmetric (SUSY) partner of the top quark. This search concentrates on stop/anti-stop($\widetilde{t}, \overline{\widetilde{t}}$) pair production with the dominant decay being $\widetilde{t} \rightarrow c + \widetilde{\chi_1}$, where c is the charm quark and $\widetilde{\chi_1}$ is the lightest supersymmetric particle(LSP). The signature in the DØ detector is 2 jets, from the $c, \overline{c}$ hadronization, and missing transverse energy from the escaping $\widetilde{\chi_1}$s. The result of this search is a limit on light stop production as a function of stop and LSP masses expressed as a 95% confidence curve in stop/LSP space.

Dedication

To my wife Karin, without whom this would not have been finished.

Acknowledgements

There are certainly a large number of people who deserve thanks for helping me to complete my dissertation. I'm sure that I'll not credit all the people who are due, but I'll do my best.

The DØ experiment is a huge collaboration of people who have come together to accomplish what a few would never be able to do. If I were at DØ from the start I could never begin to fully appreciate the effort countless people have made on my behalf. Sometimes I'll hear the name of some long lost collaborator mentioned with a breath of reverence or note a news article announcing the passing of another collaborator whose contribution to the experiment I'll never understand. I just have to take it on faith that they've found gratification on their own for their work and that any thanks from me are not needed. Needed or not, my thanks are humbly offered to those who have made DØ what it is.

While working with DØ I have read my fair share of DØ dissertations. I've always tried to make a point of reading the author's acknowledgements to see how they made it through. Often I've been quite envious as they list name after name of people that contributed to their individual effort. The number of DØ collaborators that have helped me with this analysis has been quite limited and that makes their contribution all the more important.

Certainly Chris Hays deserves my eternal gratitude. Although Chris and I rarely seemed to agree on things, it was only through his work and help that any of this analysis got finished. The construction of the W and Z backgrounds was entirely his work, I merely inherited his work and techniques to use. I've repeated the work, but I certainly would not have done as good a job on my own. I only wish I could have been at least half as helpful to him as he was to me.

John Krane is a person that seems to receive a great deal of attention in the acknowledgements of his contemporaries and with good reason. John helped more than he probably knows. More than any other person at DØ John is the reason I've finished. Whenever I think unkind things of the DØ collaboration I remember that John Krane is among them and realize that it can't be all bad. John is the embodiment of the sentiment that you can get more with a kind word and a 2x4 then you can with a 2x4 alone. John never forgets the kind word (or the 2x4).

Eric Flattum interacted with me briefly before heeding the call of free enterprise and moving on. For such a short amount of time spent with Eric, I sure learned a lot about the nuts and bolts of the analysis software. I often wonder how much sooner this would have been completed if Eric had stayed.

Greg Snow got me involved with the DØ experiment. Greg was willing to take a chance on a wholly unremarkable graduate student. I owe Greg a debt of gratitude for all the things he's done for me while I've been here at Nebraska.

When Nebraska hired a new particle physicist several years ago, I knew that I would be working with him, most probably as my advisor. I could not have known at the time how lucky I would be that they hired Dan Claes.

Dan has been the best advisor I could have hoped for. He often knows what I'm thinking and heads off any questions that I'm afraid to ask with the answers I need to hear. I know that if Dan had not become my advisor, I most certainly would not have finished.

Strangely enough there are many people not involved in a dissertation who, none the less, are crucial to its completion. From parents to spouses, past professors and friends, all are needed to help the individual finish. This large collaboration of people also has its share of unnamed contributors that will be neglected here. For those who I forget here, I'm sorry.

I grew up in a small town in Nebraska, North Loup. Everyone there grows up to be farmers, teachers and craftsmen. I can't say that I know of another scientist to come out of my home town. However, even without successful precedence, my parents never thought to tell me I might fail. I don't know if it ever occurred to them I might. I owe everything I am to my parents. From my mother I get all my sensitivities. Her kind, giving heart is truly unique. From my father I get my sense of duty. From dad I also know the value of hard work, even if I could never live up the example he sets. Even though they don't understand what I do, they never fail to ask how it is going. There is a quiet nobility in that. I don't think I'll ever be able to pay them back for all they've done.

In that same small town is a fellow named Phil Van Horn. Phil taught me about having fun and being kind. His soft spoken humor and boundless faith helped keep me going. Even though we never speak of it, its from Phil I get my faith in God.

The little, under-funded high school I graduated from had some excellent teachers when I passed through its doors. Mel Shoemaker helped me to

speak in front of people, even though I never thought I had anything to say. Lee Jacobsen gave me music, something I've come to neglect over the years but still value. Mike Tolfa taught me the value of science. He alone thought I could be a scientist, even when the career counselor thought I'd do better sweeping floors. These teachers allowed me the strength to make it through troubling times at the University of Dallas. I owe them a great deal and try to honor them when I teach my classes.

I received my college education from a small private university in Texas, the University of Dallas. There I met my undergraduate research advisor Sally Hicks. Sally and I never saw eye-to-eye, but I learned more from her than I realized. While doing shifts at the DØ test beam I realized that I was doing things I had no good reason to know how to do. I learned those things while doing shifts for Sally. She taught me what it means to be an experimenter. I didn't write an acknowledgement in my undergraduate thesis, so I never told her thanks. She deserves it.

While I was working on my masters degree at UNL I met a young woman working toward a masters degree in archeology. I didn't know at the time that she would become the single most important person in my life. More than any other person Karin Roberts is responsible for me finishing my degree, not because she helped me do it, but because she believed I could.

To all those named, and all those who I've forgotten, thank you.

Contents

Chapter

List of Figures

Figure

List of Tables

Table

Chapter 1

Introduction to Particle Physics

The study presented here is a search for the existence of a particle that would indicate physics beyond the standard model. This research was conducted at the Fermi National Accelerator Laboratory (Fermilab) in Batavia, Illinois in conjunction with the DØ experiment. The experiment described in the following text attempts to further our understanding of the science of particle physics in seeking to discover physics beyond our current understandings of the universe. What follows in this section is a brief introduction into particle physics and the standard model to help facilitate the understanding of the research presented here.

1.1 Particle Physics

The *concept* of particle physics can trace its roots back to Aristotle who contemplated the existence of indivisible "atomai", the fundamental building block of nature. It is from Aristotle's "atmos" that we get the word atom. Aristotle's understanding of particle physics was based solely on conjecture and reasoning and without experimental verification.

The *science* of particle physics had its beginnings in the discovery of radiation in the latter half of the 19th century. Particle physics describes

the interactions and properties of the smallest constituents of matter and the forces that influence them.

Early experiments in particle physics relied heavily on natural sources of particles and fields. An experiment that set the stage for experiments of the same nature as that conducted at Fermilab was the Rutherford scattering experiment. Utilizing the "alpha rays" from a natural source, Rutherford, Geiger and Marsden shaped our understanding of atomic structure. Alpha particles (helium nuclei) were directed at a barrier of dense material (gold, platinum or other heavy metals). The deflection of alpha particles as they passed through the barrier was recorded by observing flashes in a detector. The radius of an atom was already understood to be about $10^{-8}cm$, but its mass was assumed to be uniformly distributed throughout the volume. Large deflections of the alpha particles, or even recoils, off the barrier suggested that the properties of the atom were much different. These recoils could only be explained by the atom having a dense inner core that housed the bulk of the atomic mass. Thus the concept of the nucleus was born. In essence, the alpha particle was used to probe the atom to determine its structure. This was the start of using particles to examine the structure of the very small.

The Rutherford experiment was a success in that it discovered the nucleus, but was unable to probe the structure of the nucleus. To accurately probe distances on the order of the atomic nucleus would require particles of increasing energy[1]. To further probe the molecular, atomic, nuclear and subnuclear distance scales the design and construction of particles accelerators

[1]The connection between energy and probing distance is easily reconciled in the DeBroglie relationship which holds that the wavelength of a particle is inversely proportional to its momentum, $\lambda_{DeBroglie} = \frac{h}{p}$. Thus for a particle to have a wavelength short enough to probe the nuclear radius it must have a sufficiently high momentum.

Accelerator Type	Current Beam Energy limits	Physics Probed
Cockcroft/Walton	~100 keV	Nuclear disintigration
Van DeGraaff	<50 MeV	Nuclear Structure
Linear (Linacs)	<500 MeV	Light Meson Production
Tandem Van DeGraaff	~100 MeV	Nuclear Structure
Cyclotron	~500 MeV	Meson Production
Synchrotrons	~1000 GeV	Top or Higgs Production

Table 1.1: Energies reachable by various accelerators and the physics of interest in that energy range.

began.

1.2 Accelerator Physics

In the beginning of the discovery era of particle physics natural occurring radioactive sources were capable of supplying the mechanism necessary for making complete measurements. As early as the 1940s it became apparent that natural sources neither gave the control, statistics or precision to further the field. Cosmic rays could provide the energies needed for rudimentary high energy experiments, but with insufficient statistics for searches and occurred in random energy ranges. Natural source such as radioactive Lead, Uranium and Cobalt were well understood, emitted radiation with consistent rates and energies, but lacked the energy needed to breach the nuclear radius. To eliminate these problems, physicists began to create artificially accelerated particles to use in their experiments.

1.2.1 Electrostatic accelerators

Early particle accelerators used simple electrostatic potentials to accelerate charged particles. The earliest accelerator utilizing electrostatic potentials is the Cockcroft/Walton device. Designed and implemented in 1932

the Cockcroft/Walton accelerator could reach a potential of 800 kiloVolts (kV). Any particle with a charge equal to that of 1 electron could be accelerated to 800 kilo-electronVolts (keV[2]). With such energies the first artificially induced nuclear disintegration was observed. Using artificially accelerated particle a proton incident on a ^{7}Li nucleus produced two ^{4}He nuclei. The energies of the particles produced by this type of accelerators are much too small to facilitate the creation of new, massive particles. Cockcroft/Walton accelerators are now used mostly as pre-injectors for larger accelerators.

Limiting the Cockcroft/Walton design is its ability to hold its terminal voltage stable as well as its fairly small energy range. The accelerator design that supplanted the Cockcroft/Walton was the Van DeGraaff generator. The Van DeGraaff design was a vast improvement on the Cockcroft/Walton design. Using basic electrostatics, the Van DeGraaff charges a conductor by placing it in electrical contact with a charged insulator. The technique involves a moving belt which carries charge into contact with a large conducting sphere or cylinder. The only limit to the Van DeGraaff is on how much charge can accumulate on the conductor before it discharges to a nearby object. Van DeGraaff machines are utilized for examining nuclear structure, but cannot attain energies needed to probe the particles within the proton or neutron.

1.2.2 Magnetic Resonance Accelerators

Rather than the limited approach of the static electricity to accelerate charged particles, more dynamic devices can be utilized to facilitate high energy

[2]The electron volt is a common measure of energy in high energy particle physics. Often the standard prefixes are used to indicate large energies such as kilo-electron volts (keV), Mega-electron volts (MeV) and Giga-electron volts (GeV) ,which indicate x10^{3}, x10^{6} and x10^{9} respectively.

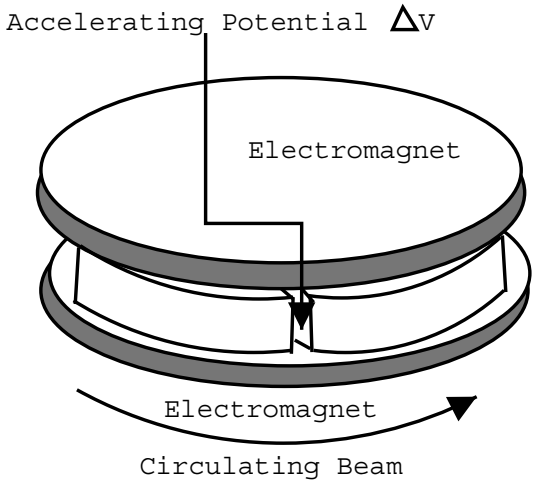

Figure 1.1: A simplified representation of a cyclotron accelerator.

particle production. A cyclotron accelerator is such a device. It uses a static magnet field to allow charged particles to circulate in circles of ever increasing radii, see figure 1.1. As the particle accelerates, the magnetic field becomes insufficient to hold it within the region of the magnet. Thus the physical size of the cyclotron as well as the field strength of the magnet impose an energy limit on any given device.

A natural extension of the cyclotron is to house magnets at a fixed radius where charged particles can be accelerated by varying the magnetic field as the particles accelerate to their final energies. This type of accelerator is called a synchrocyclotron. In order to accommodate the varying fields and speeds of the particles, a synchrocyclotron must use pulsed operation modes rather than a continuous mode. The major limits to synchrocyclotrons are magnet technologies and cost constraints. The Tevatron at Fermilab is based on this technology.

1.3 Detector Physics

As particle physics matured into the science that it is today the advancement in particle detectors was needed as well. Early particle detectors were simple devices that merely signalled the passage of a charged particle. Now particle detectors are massive systems of smaller detector subsystems that measure detailed features about complex interactions of particles. To fully appreciate the complex nature of the DØ experiment it is necessary to understand the functionality of various particle detectors.

1.3.1 Gas Filled Detectors

A simple detector used to detect the passage of a charged particle is the proportional counter or drift chamber. Figure 1.2 shows the simple geometry of such a device. Electrons created in the ionization of the gas travel from the gas down to the anode wire due to the electrostatic attraction of the potential difference. As the electrons impact the anode wire a current pulse is created in the wire. This pulse is read out by electronics boards. The amplitude of this pulse is proportional to the number of electrons released in the gas which is related to the energy of the incident particle. Proportional drift chambers have a accuracy of 50 to 300 μm and time resolution of 2ns and a dead time of 100ns.

Drift chambers are employed throughout the DØ detector.

1.3.2 Scintillators and Photomultiplier Tubes

A large class of detector type good for varying applications are scintillation detectors. A scintillator is any material that emits light while charged

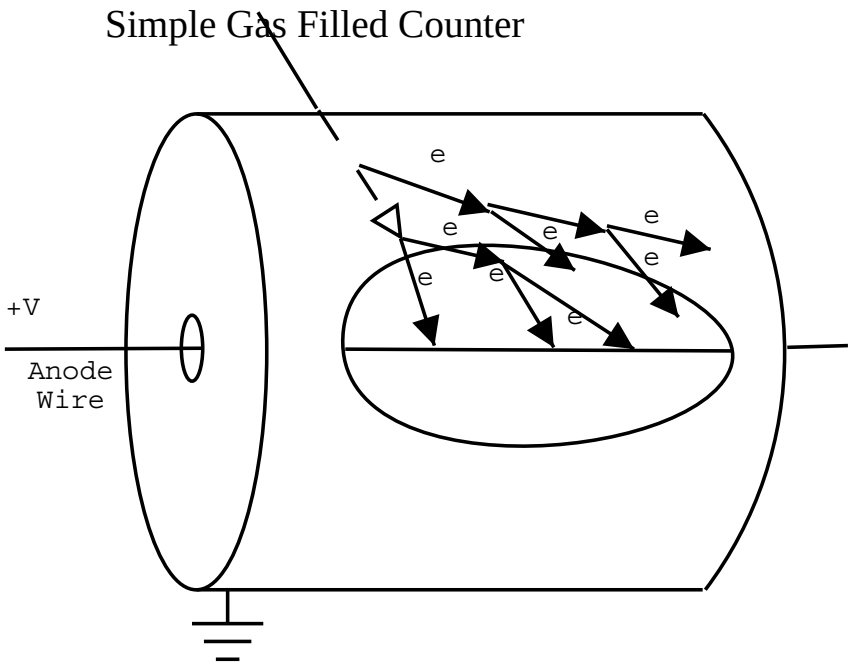

Figure 1.2: A sketch of a proportional counter. The gas within the canister ionizes as a charged particle passes through the volume.

particles pass through it. Scintillator material can be one of three types; crystalline, liquid or plastic. The flexibility of the material makes for a wide range of uses and applications. From simple square sheets of scintillating plastic to vast tanks of purified water scintillation detectors can be found in some shape or another in almost all nuclear and particle experiments.

The usefulness of a scintillating material is that it can be used to convert a single, hard to detect high energy charged particle into a large number of low energy, easily detected charged particles through the use of a photomultiplier tube. Photomultiplier tubes (PMT) are the most common of all particle detectors and work on a simple principle. The light emitted from the scintillation material is passed through a transparent aperature to a PMT (or to the PMT via a wavelength shifting material). The photon then strikes a photosensitive surface that emits a photoelectron. This electron then cascades down to another plate which emits several electrons. This process continues until a large number ($\sim 10^6 - 10^7$) electrons strike an anode which reads out a current spike. This current spike is generally proportional to the energy of the charged particle. Figure 1.3 shows a simple diagram of a PMT.

A typical scintillator detector will have a time resolution of 150 ps and a dead time of 10ns.

1.3.3 Calorimeters

To accurately measure the energy of a particle radiated from a collision calorimeters are employed. Calorimeters are detectors which are comprised of an energy sampling material located just behind a shower inducing material and an active, ionizing material. Calorimeters can utilize several different types of shower inducing materials but the higher the atomic number of the

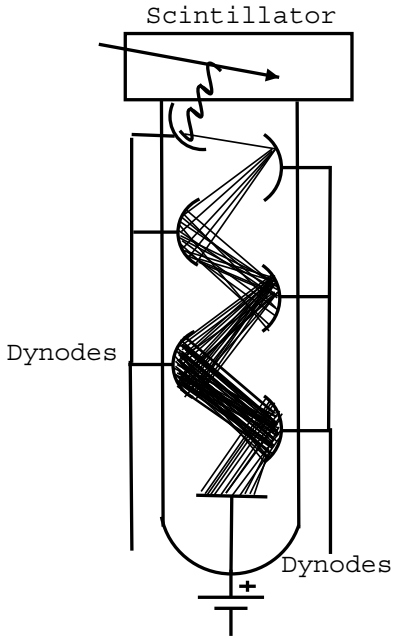

Figure 1.3: A photomultiplier tube. Each dynode creates a cascade of electrons.

First Generation	Second Generation	Third Generation	Charge
e (electron)	μ (Muon)	τ (Tau)	-1
ν_e	ν_μ	ν_τ	0
up	charm	top	$+\frac{2}{3}$
down	strange	bottom	$-\frac{1}{3}$

Table 1.3: The fermions of the standard model. The first two rows give the Leptons and the last two rows are the quarks. Each quark can exist in any of three color states, thus each quark represents three (3) particles. All fermions have corresponding anti-particles.

material, the better it is at inducing showers and less physical space is needed to allow for complete deposition of energy in the overall detector.

1.4 The Standard Model and Supersymmetry

Experimental and theoretical particle physics have worked to construct a complete theory of all observed phenomena, called the Standard Model (SM). To understand the need for physics beyond the standard model a basic overview of the SM itself is needed.

Our everyday experience gives us a small insight into the ideals behind the standard model. Nature exists as objects and the forces that act upon them. The standard model categorizes these two facets of nature as matter and fields.

1.4.1 Fermions

All matter is comprised of fermions. Fermions are particles that have $(1/2)\hbar$ units of angular momentum, called spin. Table 1.3 shows a comprehensive list of SM fermions. Being 1/2 integer spin particles, fermions obey the Pauli exclusion principle and cannot share a given quantum state with any other fermion. Fermions come it two distinct varieties, quarks and leptons.

Quarks are fermions that participate in the strong force, as well as the electromagnetic and weak but are never observed in an unbound state. Particles that consist of three (3) quarks are called Baryons and particles that consist of a quark and its antiquark are called mesons. Each individual quark type (up, down, etc.) comes in three distinct color flavors.

Color charge is a quantum number that distinguishes quarks in a bound state. Net Color is not observed in nature, so all combinations of bound quark states must be colorless. Color charge has three "polarities" named for the primary visible colors, red, green and blue (as with particles, there are also anti-color states, anti-blue, anti-green and anti-red). Interactions of colored particles are described by the SM sub-theory of Quantum ChromoDynamics (QCD) [more on this in section 1.4.3].

Charged leptons are fermions that participate in all interactions except the strong (and are thus colorless). Leptons can exist as free particles. For each electrically charged lepton state there is a charge neutral neutrino. These neutrinos only participate in the weak interaction and are very difficult to detect in experiments.

The fermions are categorized by generations in the table, and in nature. The first generation of fermions are all that are needed to account for all common forms of matter. The second and third generations of fermions must be produced in a high energy interactions, such as created at a high energy particle accelerator or in cosmic ray interactions. This breaking of generations of fermions is a strength of the SM. When the only known quarks in existence were the up, down and strange, a charm quark was predicted by the the observed suppression of flavor changing neutral weak interactions. After the discovery of the charm, a third generation of quarks was predicted by the SM

Particle Name	Force Exchanged	Rest Mass	Electric Charge
Photon (γ)	Electromagnetic	0	0
$W^{\pm}$	Weak	~80.2 GeV	± 1
Z^0	Weak	~91.2 GeV	0
Gluon	Strong	0	0
Higgs	Couples with Matter	Unknown	Varies by theory

Table 1.4: The bosons of the standard model. Not included is the graviton (spin=2) which, presumably, exchanges the force of gravity. Gravity is not currently explained by the standard model.

to allow for CP violation.

Both quarks and leptons carry a quantum number called weak isospin, represented by T. Weak isospin has deep significance in that it reflects a hidden symmetry of the electroweak interaction. All quarks and leptons belong to a T=1/2 doublet. Figure 1.4 shows a representation of the first generation of fermions in terms of their relationship to isospin.[3] Each fermion generation would have a similar diagram.

1.4.2 Bosons

The standard model also describes the interactions of all standard model particles[4]. These particle interactions are taken to be interactions between the fermionic particles and a gauge boson field. Thus the interaction can be described as an exchange of boson particles which represent the quantized states of the field. Each fundamental force is characterized by its own field and thus its own characteristic particle or particles. Table 1.4 shows a comprehen-

[3]The "prime" characterization on the d quarks in figure 1.4 is to indicate that the d quark in this representation is not a pure d quark state but is rather a linear combination of d and s quark states. This is needed so that a charge changing weak interaction only produces transitions between the two quark states in the generation, thus creating a pure T-doublet generation.

[4]It is important to note that gravity has not been successfully integrated into the Standard Model and thus is not considered here.

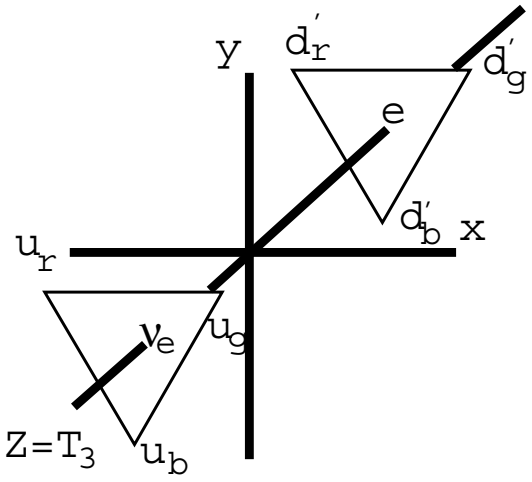

Figure 1.4: A Cartesian coordinate system representation of the first generation of fermions in the Standard Model. The X and Y axis denote shifts in color states (thus the colorless electron and neutrino are along the Z axis). The Z axis represents shifts in the T_3 component of weak isospin.

sive list of SM gauge bosons. The Higgs boson has not been observed in nature and may consist of a family of Higgs bosons rather than a single particle.

The strong interaction is mediated by the gluon and couples to a particle's color. Electromagnetic interactions are mediated by photons and couples to a particle's electric charge. The weak interaction is transmitted by W and Z bosons and is somewhat enigmatic in that it is neither a repulsive or attractive interaction, but rather is primarily seen in decay interactions such as beta decay. Presumably gravity is also mediated by a gauge boson, the graviton, but the interactions of gravity are not included in the Standard Model.

1.4.3 QED and QCD

Historically as physicists approached the interactions of particles they did so from the top down, explaining lower energy facets of the theory before being able to experiment on the higher energy portions of the theory. As such, there are two distinct names given to different interaction which dominate different characteristic energy scales. The theory that describes electromagnetic and weak interactions is called Electoweak and it contains the theory of Quantum ElectroDynamics (QED) and the theory that describes colored, or strong, interactions is called Quantum ChromoDynamics (QCD). Both of these theories are based on gauge invariant group theory.

For a theory to be "gauge invariant" the interaction terms of its Lagrangian must be invariant over local symmetry transformations. For the purposes of clarity, consider the photon, which couples to a particle's charge. Gauge invariance stipulates that the Schrödinger equation is invariant when the particles wavefuntion undergoes an arbitrary change of phase, i.e.:

$$\psi(\overrightarrow{r},t) \rightarrow e^{-i\chi(\overrightarrow{r},t)}\psi(\overrightarrow{r},t) \tag{1.1}$$

The invariance of the kinetic energy term is maintained by the introduction of a vector potential $A(\overrightarrow{r},t)$. This vector potential term is appended to the Schrödinger equation as an addition to the gradient:

$$\nabla - iQA \tag{1.2}$$

which, when equation 1.1 is applied undergoes the transformation:

$$A \rightarrow A - \frac{1}{Q}\nabla\chi \tag{1.3}$$

To be gauge invariant the observables of the theory must be independent of χ through gauge transformations. In the photon's case, this invariance is manifest in electromagnetic theory as the magnetic field being the curl of A and the energy density $\overrightarrow{j} \cdot A$.

The gauge definition of electromagnetic interactions is summarized in the theory QED which earned its authors Nobel prizes. The theory is based on a U(1) symmetry transformation of the fields corresponding to charged particles. In order for the field to remain gauge invariant the introduction of a neutral spin 1 field that couples to charged particles and whose coupling is proportional to the particles charge. The quantum of this field, as should be apparent, is the photon.

The coupling constant of the EM field is generally referred to as α_{EM} and has some strange properties. The electromagnetic coupling, α_{EM}, is generally constant at a value of about $\frac{1}{137}$, however as the interaction distance

decreases, α_{EM} increases. Often physicists explain this particular phenomena as a "screening" of the true electric charge of a particle. It is often stated that the true electron charge, for instance, is really infinite, but vacuum polarization about the electron screens the universe from this infinite charge. Thus infinite vacuum polarization screens the infinite "bare" charge to a finite, observable value. This mathematical trickery in which one infinity of a theory cancels another is called "renormalization" and is a characteristic of useful gauge theories.

QCD is the gauge theory which describes the interactions of colored particles as they participate in strong interactions. Since quarks, the colored fermions, come in three different colored states, the invariance must be over a SU(3) transformation of color charge. Local SU(3) invariance requires eight spin 1 mediating fields. Thus there are eight different gluons, six which correspond to color changing interactions and two that do not. Gluons also carry color, as SU(3) is non-Abelian and as such interact with themselves. As with QED, QCD has a coupling constant which is referred to as α_s.

The coupling constant α_s also has some oddities. As distance becomes smaller α_s becomes smaller. Thus colored objects that are very close together, quarks in a proton for instance, experience a very small interaction by the strong force. Quarks confined in a proton are almost non-interacting (in the scope of the strong force). This characteristic of the strong coupling constant is often referred to as asymptotic freedom since the interaction almost goes away as the particles approach each other. Likewise, α_s grows very strong as the particles separate. It is for this reason that colored particles are not observed free. The strong interaction of a colored particle to another colored particle a macroscopic distance away would be huge, so much so that it becomes energetically preferable for the universe to create a particle/anti-

particle pair out of the vacuum to bridge the distance and create bound states. This process of particle/anti-particle creation in the midst of separated colored particle is observed in particle detector as "jets" and is called "hadronization". Hadronization, which is a simple concept on the surface, is not well understood at a fundamental level.

1.4.4 Weak Interactions and the Higgs Mechanism

One of the more triumphant accomplishments of the standard model was the unification of the electromagnetic and weak interactions a unification proposed by Glashow in 1961 and further advanced by Weinberg and Salam[5]. Some noted that this would be highly unlikely as the electromagnetic and weak forces had such a difference of scale. What if the weak were mediated by a massive particle? If this were true than the disparity between the forces could be resolved. However, for local gauge invariance to hold in the weak sector (thereby allowing for it to remain renormalizable) the gauge bosons that mediate the interaction must be massless. Clearly from table 1.4 the W and Z bosons have been observed to have mass. This gives rise to a problem, how does one introduce mass into the weak interaction, retain local gauge invariance and unify it with electromagnetic interactions.

The answer lies in spontaneous symmetry breaking[6]. Consider the Lagrangian for a scalar field ϕ :

$$\mathcal{L} = \frac{1}{2}(\partial_\mu \phi)(\partial^\mu \phi) + e^{-(\alpha\phi)^2} \tag{1.4}$$

[5]The electroweak is sometimes referred to as GWS theory (Glashow-Weinberg-Salam).

[6]A full discussion of gauge theory is well beyond the scope of this document and readers are encouraged to seek out an undergraduate level text on particle physics, such as references [5, 6], to fully review the techniques involved.

where α is a real constant. At first glance this appears to be the Lagrangian of a massless field since there does not appear to be a massed term, however if you expand it out:

$$\mathcal{L} = \frac{1}{2}(\partial_\mu \phi)(\partial^\mu \phi) + 1 - (\alpha\phi)^2 + \frac{1}{2}\alpha^4\phi^4 - ... \tag{1.5}$$

the α^2 term appears to resembled a mass energy term (in the Klein-Gordon equation) except that its negative (implying an imaginary mass). What is really lurking here is that the scalar field in 1.4 is not in the ground state when $\phi = 0$ (as it is in the strong and electromagnetic forces), from which our theory should arise but is really in the ground state at $\phi = \pm\frac{\mu}{\lambda}$.[6, Page 360-362] Introducing a new field variable variable, $\eta = \phi \pm \frac{\mu}{\lambda}$, and writing the Lagrangian as:

$$\mathcal{L} = \frac{1}{2}(\partial_\mu \eta)(\partial^\mu \eta) - (\mu\eta)^2 \pm \mu\lambda\eta^3 - \frac{1}{4}\lambda^2\eta^4 + \frac{1}{4}(\frac{\mu^2}{\lambda^2}) \tag{1.6}$$

now has the proper sign on the mass term. The interaction has not changed during this change of variables, but a fundamental change has happened to the Lagrangian. Notice that in 1.4 the Lagrangian is even in ϕ (i.e. if $\phi \to -\phi$, $\mathcal{L} \to \mathcal{L}$). The Lagrangian in 1.6 is NOT even in η. In rewriting the Lagrangian in this new fashion the symmetry has been "spontaneously" broken, see figure 1.5 for a mechanical analog.

The story becomes more interesting when one considers that this new Lagrangian has two ground states, if one were to introduce another field, a continuum of ground states are created, a representation that is more rep-

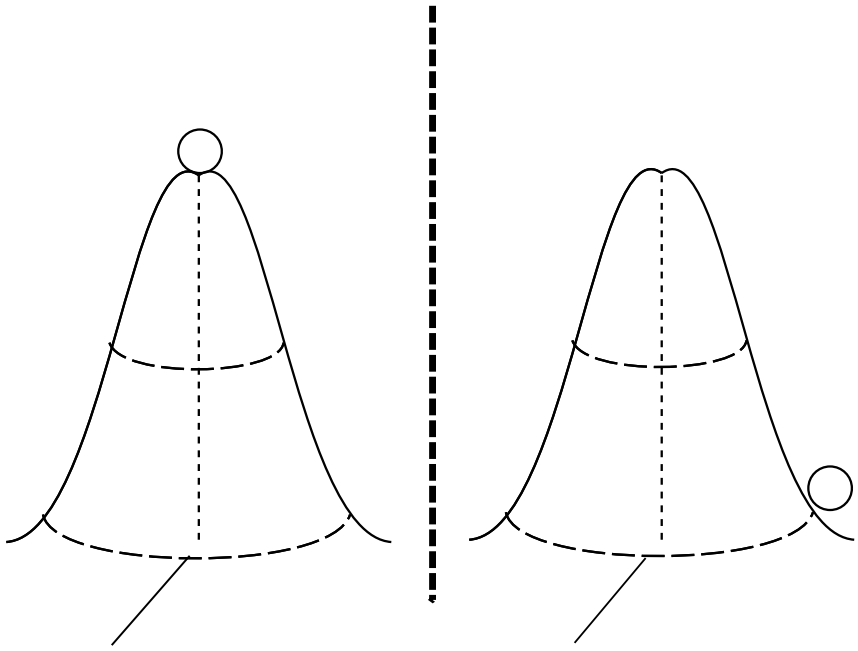

Figure 1.5: A cartoon representation of spontaneous symmetry breaking. In the situation on the left the hill/ball system is symmetric. After the ball rolls down the hill there is a distinct left/right asymmetry established. This occurs since the ball's preferred energy state is not the same as the symmetrical state.

resentative of reality. Without working through the mathematics, it can be shown that this new field does not introduce another massive mediator, but rather a massless boson. Although adding the second field add realism to the Lagrangian, it introduces a new massless particle to the mix which is not present in observations. The introduction of this second field has moved us further from reality, but there is a mechanism by which everything will come back around. By imposing *local* gauge invariance to and changing the choice of gauge of the system, again not working through the details, it happens that the theory will leave us with a single massive boson and a massive gauge field, eliminating the massless boson that came from the introduction of the second field.

What does all this have to do with weak interactions? The weak theory now has a way of having massive exchange particles but to still be gauge invariant. This mechanism is called the Higgs mechanism and it is no coincidence that the massive boson that flows from this argument in respect to the weak theory is called the Higgs boson. It is from the tools of spontaneous symmetry breaking and local gauge invariance (the Higgs mechanism) that the Z and W acquire mass in the standard model. Its from constructing a comprehensive weak interaction that the SM requires a Higgs boson[7].

1.5 Deficiencies of the Standard Model

The standard model of particle interactions is a highly successful theory. Although tested to precision greater that 0.1% the standard model still has some glaring omissions. Still unobserved is experimental evidence of a

[7]Yukawa interactions with all the SM fermions and the higgs boson also give mass to ordinary matter. However the theory gives no indication what the mass of the Higgs might be.

Higgs sector. Without the existence of a Higgs mechanism the standard model predicts massless particles which is in clear contradiction to reality. While the Higgs sector will complete the standard model, the theory carries with it problematic characteristics.

The addition of a Higgs sector to the standard model consisting of an $SU(2)_L$ doublet of Higgs bosons would provide the simplest completion to the standard model. Once the neutral component of the Higgs boson has a vacuum expectation value, the W and Z gauge bosons acquire mass through the breaking of the $SU(2)_L \times U(1)_Y$ gauge symmetry. Fermions would gain masses through the breaking of chiral symmetry forbidding their masses. This model also alleviates problematic infinities that arise in the electroweak radiative corrections through coupling the Higgs boson to gauge bosons and canceling the unitarity violation in the gauge boson scatter sector. For these reasons the Higgs sector seems to be a necessary and attractive addition to the standard model.

The addition of a simple Higgs sector carries with it problems of its own. The problems with a simple addition of a Higgs sector arise from the properties needed by the Higgs particles in order prevent unitarity violation in the scattering of longitudinal gauge bosons. To accomplish this, the mass of the Higgs must be less than ~800GeV[10]. Note the scalar potential for the Higgs field, h, is given by,

$$V \sim M_{h0}^2 h^2 + \lambda h^4 \tag{1.7}$$

Doing a single loop Feynmann calculation, the self-interactions of the Higgs creates a divergent contribution to the Higgs boson mass. The divergent con-

tribution can easily be countered by canceling it with a mass counter term δM_h^2, with the mass of the Higgs now being given by

$$M_h^2 \sim M_{h0}^2 + \frac{\lambda}{4\pi^2}\Lambda^2 + \delta M_h^2 \tag{1.8}$$

This would seem quite satisfactory and inline with the theory however if there is no new physics between the electroweak scale and the Plank scale, then Λ must also be of the Plank scale. Thus the large term in the Higgs mass that carries the Λ would then have to be canceled by the δM_h^2 term so that the overall mass of the Higgs is less than 800 GeV. This highly unlikely turn of events is called the *fine tuning* problem and would extend to every term in a perturbation theory, thus each term in an perturbation expansion would also carry its own fine tuning. Supersymmetry (SUSY) successfully removes the problem of fine tuning, and is thus an attractive theory to investigate.

1.6 Basic SUSY

Basically Supersymmetry is a symmetry which relates particles of differing spin. In a Supersymmetry the particles are combined in a super-field which contains fields differing by $(1/2)\hbar$ units of spin. In the simplest example this super-field would contain a complex scalar and a two-component Majorana[8] fermion. If we represent the complex scalar by S and the fermion by ψ then the simple SUSY Lagrangian is given by:

[8]A Majorana fermion is one which is equal to its charge conjugate.

$$L = -\delta_\mu S^* \delta^\mu S - i\overline{\psi}\overline{\sigma}^\mu \delta_\mu \psi - \frac{1}{2} m(\psi\psi + \overline{\psi\psi}) - cS\psi\psi - c^* S^* \overline{\psi\psi} \\ -|mS + cS^2|^2 \qquad (1.9)$$

Here σ is a 2x2 Pauli matrix and c is an arbitrary coupling constant. Since the fermions and scalars share the same coupling, the cancellation of quadratic divergences that occur in the Higgs sector are automatic.

An experienced eye will notice that in equation 1.9, the fermions and scalar particles will have the same mass. This fact is in clear contradiction to experimental evidence since physicists have yet to observe a particle with integer spin and the mass and charge of the electron (for instance). Thus SUSY, if it exists, would have to be a broken symmetry where particles and SUSY-particles (sparticles) no longer have degenerate mass states. Thus there would be ample evidence in the universe as to the veracity of SUSY since for every standard model particle there would be SUSY partner particle. For every standard model fermion there would be a SUSY scalar particle and for every standard model scalar particle there would exist a SUSY fermion. By convention the SUSY scalars are named after there standard model partners, but preceded by an 's'. Thus the SUSY partner to the electron is the selectron, the SUSY partners to the neutrino would be the sneutrino, etc. The fermion SUSY partners to standard model scalar particles share this convention except that the standard model particle name is ended with an 'ino' suffix. Thus the SUSY partner to the W boson is the 'wino' and the SUSY partner to a photon is called a photino, etc. As a whole the SUSY fermions are called gauginos. This duplicity of particles is present in all the various SUSY models.

1.6.1 SUSY Models

The spontaneous symmetry breaking of the SUSY theory leads to several different models for SUSY implementation. Although this search is mostly model independent (assuming only R-parity conservation), only making assumptions on relative branching fractions and sparticle masses, it is interesting to note how the SUSY theory is actualized in some of the leading model.

1.6.1.1 Minimal SUSY

The SUSY model that introduces the fewest new particles is Minimal Supersymmetry (MSSM). MSSM respects the same SU(3)xSU(2)$_L$xU(1) that the SM does. For each standard model particle a SUSY particle is assigned for each degree of freedom. For a SM charged lepton there is two sparticle scalers, for the neutrinos there would only be a single SUSY sneutrino since there is only one helicity state for SM neutrinos, and thus one degree of freedom. Gluons, which carry 16 degrees of freedom (2 for helicity by 8 colors) are associated with a massive spin $\frac{1}{2}$ gluino which also carries 16 degrees of freedom. MSSM creates a large zoo of SUSY particles.

MSSM does not leave the Higgs sector unaltered from its simple Higgs doublet implementation in the SM. In order for the up and down type quarks to gain mass there needs to be two Higgs doublets.[9] From these Higgs doublets arise five (5) Higgs particles, two charged scalars (called $H^{\pm}$, respectively), two neutral scalars (a lower mass h, and a higher mass H) and a single neutral pseudoscalar (A). This gives rise to a new SUSY parameter called $\tan\beta$. This parameter is the ratio of the two vacuum expectation values arising from the

[9]The up and down quark types are able to gain mass from a single Higgs field through its conjugate field. This conjugate field cannot be used in MSSM.[2]

two Higgs particles. Searches that require MSSM are often sensitive to $\tan\beta$, this search is not.

From MSSM there arises a SUSY quantum number called R-parity. R-parity is defined by:

$$R \equiv (-1)^{3(B-l)+2s} \tag{1.10}$$

with B is the particle's baryon number, l is the lepton number and s is simply its spin. R-parity is -1 for sparticles and +1 for SM particles. Whether R-parity is conserved is a question that often arises and is not demanded in the theory. If, however, R-parity is conserved, the lightest SUSY particle (LSP) cannot decay. R-parity is assumed true in this search to provide a stable LSP that does not react with the detector, giving rise to $\not\!\!E_T$.

If R-parity is conserved SUSY partners would only be pair produced from SM particle interactions and would decay to a stable LSP. This LSP would be neutral due to stringent cosmological bounds on light charged or colored particles which are stable[3, 4]. Being light and neutral the LSP would escape detection since the only way it can interact with matter is through exchange of virtual heavy SUSY particles. This interaction would be very similar to the interaction constraints on the neutrino and thus the LSP would appear only as missing energy in an interaction. Also, if R-parity is conserved it provides a symmetry that forbids lepton and baryon number violating terms in the superpotential terms of any SUSY Lagrangian[7].

The MSSM has several attractive qualities, but it introduces a very large number of unknown parameters into the theory. The MSSM is often extended by relating it to properties inspired by Grand Unification Theories

(GUT).

1.6.2 MSSM with GUT

To reduce the vast number of SUSY parameters that arise in MSSM the theory is often modified to reflect the physics that would arise from GUT unification at high energies. The unification of the SU(3)xSU(2)$_L$xU(1) gauge coupling constants are generally taken to be near $M_x = 10^{16}$ GeV (GUT scale). Gaugino masses are then also taken to unify. At lowest order the gaugino masses then scale as the corresponding coupling constants. SUSY GUTS also assume a common scalar mass and the Higgs boson masses are now degenerate. All these assumptions reduce the number of parameters to 5 at the M_x energy scale; a common scalar mass (m_0), a common gaugino mass ($m_{\frac{1}{2}}$), a single trilinear coupling (A$_o$), a Higgs mass parameter (μ) and a single Higgs mixing parameter (B). Since this reduction of parameters space takes place only at the M_x energy scale it may be hard to see how this helps at the Weak scale.

SUSY GUTS reduces the needed parameters at the Weak scale by a technique in which the free parameters listed above are inputted into the theory at the M_X energy scale then the renormalization group equations are used to evolve the parameters at the Weak scale. Once the Z mass is required to be equal to its measured value the parameters left at the Weak scale are simply m_0, $m_{\frac{1}{2}}$, A_0, $\tan\beta$ and the sign of μ.

SUSY using GUTS as a framework for the elimination of parameters creates a very predictive theory making it possible to construct the contours for the various SUSY particle masses for values of the SUSY GUT free parameters listed above. This extension of SUSY with GUT theory helps to promote its attractiveness to theorist and make proof of SUSY a high priority for particle

physicists.

1.7 Search Strategy

It is the intention of this analysis to observe the production of a SUSY particle, the stop squark (the scalar SUSY partner of the top quark). The massive nature of the top quark (~175GeV) and some mechanisms in some SUSY models have indicated the stop may be significantly lighter than other squarks. In particular a large mixing angle between the superpartners of the left-handed and right-handed top quarks, which form the lightest stop mass, could drive the stop mass low. Alternatively, a large Yukawa coupling enters the renormalization group equations and reduces the stop mass compared to other squarks. The stop squark has two decay channels of interest for direct searches

$$\widetilde{t} \rightarrow b + \chi_1^+ \rightarrow b f \overline{f}^{'} \widetilde{\chi}_i^0 \tag{1.11}$$

and

$$\widetilde{t} \rightarrow c \widetilde{\chi}_1^0 \tag{1.12}$$

Both of these decay chains have similar signals in a particle detector: jets + missing transverse energy ($\not\!\!E_T$). The first of these decays, equation 1.11, shares many similarities to a top to b quark decay. It is very difficult to separate this signal from top signals. The second channel, equation 1.12, is the focus of the present research. The decay of this light stop is to a standard model charm and the LSP, which escapes detection.

1.8 Searching for Stop

Previously a $\widetilde{t} \rightarrow c + \chi_0^1$ stop search was carried out at DØ using the Run 1a run set [21]. That search utilized 13.5±0.7 pb^{-1} of luminosity, however to control QCD background a rejection was made on events with more that one primary vertex found in an event. This cut reduced the data set to an integrated luminosity of 7.4±0.4pb^{-1}. The signal and motivation for that search are identical to those of this search.

Currently the best published limits on light stop production in hadronic collisions from a charm to LSP decay channel are from the Central Detector Facility (CDF) at Fermilab[8]. The CDF detector is a general purpose hadronic detector that employs excellent tracking. Since CDF's signal is identical to the signal searched for in this analysis they also had to compete with large contributions to the data set arising from QCD multijet events. To help separate possible signal from background they employed an ingenious technique called tagging. Tagging is a method by which a detector with superior tracking capabilities can differentiate between a primary interaction vertex and a secondary decay vertex. Tagging allows CDF to find the vertex created when the charm quark decays to the b. This technique allowed very good rejection against backgrounds, this criteria also reduces their available luminosity by nearly 80%. Since DØ does not possess the tracking resolution that CDF enjoys the technique of tagging is not an option for usage on this analysis.

Other light stop searches have been undertaken at other accelerator facilities. Lepton colliders can provide excellent search tools as their colliding beams are made of elementary particles with no internal structure and thus no large momentum distribution from collision to collision. Lepton colliders can

be "tuned" to a particular energy that resides on a particle's resonance and then be used as a "factory" for that particle's production. The best limits set by a lepton collider are those published by LEP. ALEPH (an experiment at LEP, ALEPH is to LEP what DØ is to the Tevatron) has set very stringent limits on light stop and LSP masses, but is sensitive to the $\tan\beta$ SUSY parameter, where as hadron colliders are not.

The current limits are shown in figure 1.6. It is the goal of this analysis to provide confirmation of these curves as well as to try and extend the coverage where possible.

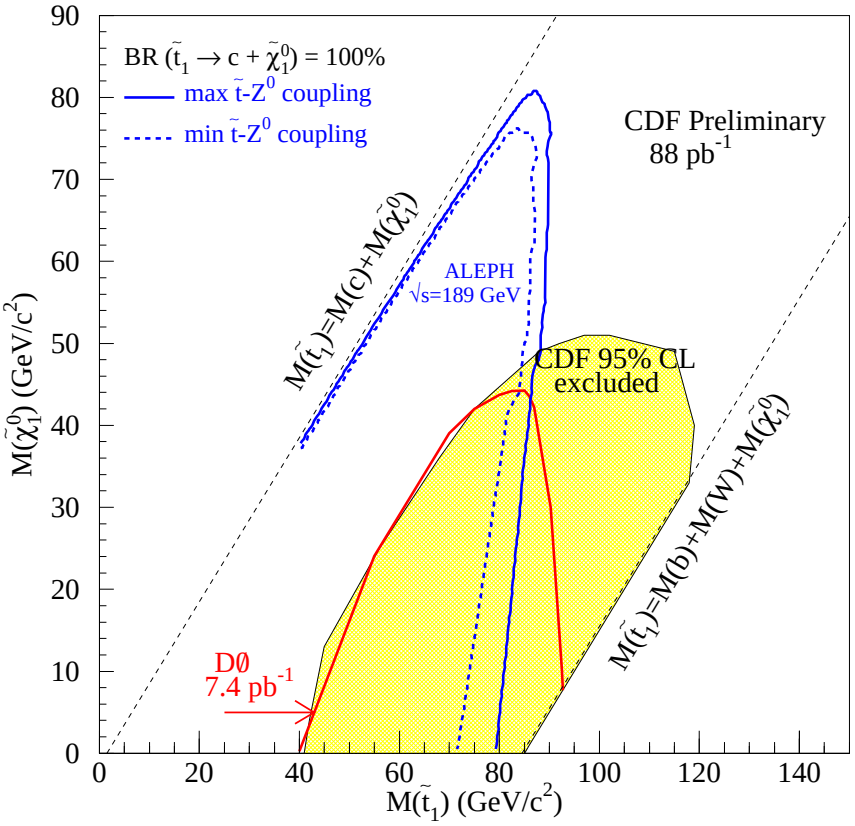

Figure 1.6: Limits from other light stop searches.

Chapter 2

Experimental Apparatus

The data set used in this analysis was taken using the DØ detector located on the Tevatron particle accelerator at Fermi National Accelerator Laboratory (FNAL or Fermilab) located near Batavia, Illinois. This Chapter will entail a general overview of the relevant features of the Tevatron and of the DØ detector.

2.1 Fermilab and the Tevatron

The reaction of quarks and anti-quarks in high energy collisions can facilitate the production of exotic sub-atomic particles. The Tevatron is but the last stage of Fermilab's particle accelerators, creating the $\sqrt{s} = 1800$ GeV proton - antiproton ($p\overline{p}$) center of mass collision used in this study. Each stage of acceleration of the protons and antiprotons is tied specifically to the effective energy ranges of the varying accelerators used in the acceleration process. For a simple layout of Fermilab see figure 2.1. For a more comprehensive and technical discussion of the Fermilab complex please read reference [1].

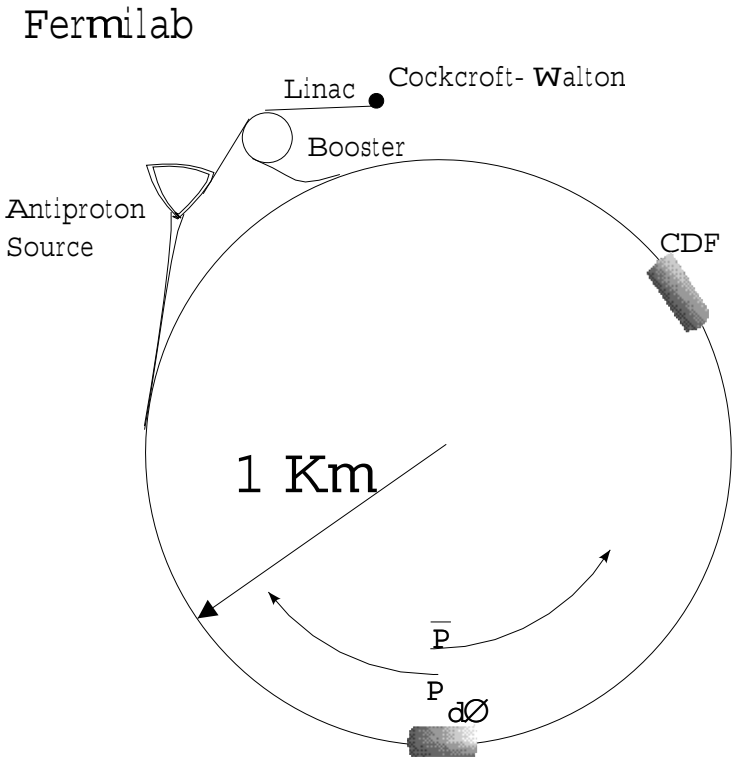

Figure 2.1: Layout of the Fermilab acceleration complex, not to scale.

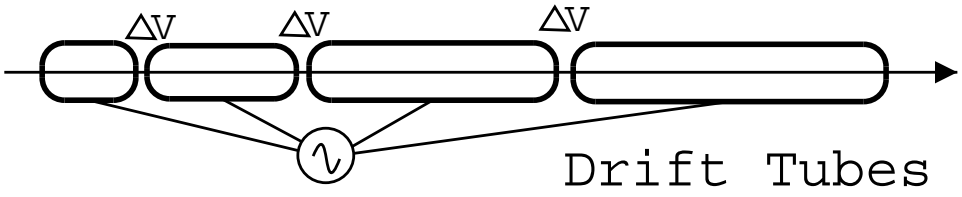

Figure 2.2: Schematic of an RF linac.

2.1.1 0 GeV to 750 KeV, pre-acceleration

The acceleration process begins with a simple diatomic hydrogen gas that is disassociated and ionized using a magnetron surface plasma source. The magnetron injects these produced H- ions into Cockcroft-Walton generator with a current of 50mA and an energy of 18keV.

The Cockcroft-Walton apparatus, whose simplistic design dates to 1932, generates a simple electrostatic potential by charging capacitors in parallel, but discharging them in series. This device accelerates the H- ions to 750 KeV.

Together these two steps are called the preaccelerator stage.

2.1.2 750 KeV to .4 GeV, the linac

The apparatus following the Cockcroft-Walton generator is the 146 meter linac. The linac (linear accelerator) is constructed of several radio-frequency (RF) cavities that serve to increase the energy of the H- ions.

The RF cavities receive their name due to the nature of the mechanism used to accelerate the particles inside the linac. The beam travels through a series of hollow tubular electrodes connected to the alternating poles of an AC voltage source. Particles are accelerated as they traverse the space between these electrodes. The electrode cavity is made of a conductor so that the beam

is not subject to an electrical field and merely drifts from the entrance of the cavity to the exit point. The time that it takes the beam to traverse the cavity is equal to the time it takes to change the polarity of the the electrodes. Thus the frequency of the alternating current is dictated by the geometry (length) of the cavity. If the AC source has a constant frequency then it becomes necessary to lengthen subsequent RF cavities since the particles in the beam are traveling faster and faster as they traverse the linac. Please note figure 2.2 for an artist conception of the linac. The AC frequency of the first stage of the Fermilab linac is 201.24 MHz, and the second stage operates at 805 MHz.

The linac accelerates the H- ions to an energy of .4 GeV or 400 MeV.

2.1.3 .4 GeV to 8 GeV, the Booster

It is at this stage that the H- ions are stripped of their electrons by being directed through a carbon foil. The resulting bare proton is injected into the booster. The booster is a synchrocyclotron with a radius of 76.2 meters. The theory of a cyclotron is very similar to a linac except that rather than the particles traversing RF cavities of ever increasing length, the particles are constrained to closed orbits by an external magnetic field whose strength varies as the particles increase in momentum. The effective energy range of the cyclotron is dictated by the strength of magnets available and the physical size of the effective magnetic field. The Fermilab booster accelerates protons to a final energy of 8 GeV.

The protons accelerated in the booster can either be sent on to the Main Ring for acceleration and injection to the Tevatron for experimental use or the protons may be sent to the Main Ring for use in the production of antiprotons.

2.1.4 8 GeV to 150 GeV, Main Ring

At a radius of 1000 meters and a final particle energy of 150 GeV the Main Ring (MR) is an impressive accelerator in its own right. Using 774 water cooled dipole magnets and 240 focusing quadrapole magnets the Main Ring serves the dual purpose of pre-accelerating particles for injection into the Tevatron and providing high energy protons for antiproton production (see section 2.1.6).

Of particular interest to this analysis is the physical location of the Main Ring beam pipe as it passes through the DØ collision hall. The Main Ring is only vertically separated from the Tevatron by a distance of 2 feet in the majority of the beam tunnels to allow for the two accelerators to share the same tunnel construct. This facilitates the efficient use of engineered tunnel space which comes at great monetary cost. This separation distance needs to be expanded to accommodate the physical presence of the large particle detectors located at collision points on the Tevatron. However, the physical separation of the two accelerators is only 2.26 meters in the DØ collision hall. This separation distance is not large enough to allow the Main Ring to pass outside the DØ detector, but rather it passes through the upper portion of the detector. Stray activity in the Main Ring creates significant background noise that must be accounted for in this analysis. This Main Ring noise will be discussed later.

2.1.5 The Tevatron

Particles from the MR are injected into the main accelerating system at Fermilab, the Tevatron. Both proton and antiproton beams are accelerated

by the Tevatron magnets. These two beams are kept physically separated except when focused to a collision point within a particle detector. This bending and focusing of the beams is facilitated by magnets located on either side of the collision halls at CDF and DØ .

The particles are coalesced into 6 separate bunches of about 10^{11} particles per bunch. These bunches then undergo the final acceleration from 120 GeV to their final 900 GeV. Once the protons and antiprotons reach 900 GeV, mechanical shutters scrape any excess particles from the beam. This energy state of the beam is called the *flat top*. The Tevatron can operate at this energy for some time before collisions of the particle bunches with beam pipes, residual gas in the beam line or in physics interactions finally dilute the bunches to such a level that new bunches need to be produced and accelerated. The time at which the Tevatron is running at flat top is called the *store*. It is during a store that data is accumulated at the detectors on the Tevatron.

The Tevatron physically shares the tunnel that houses the Main Ring, thus it too has a radius of 1000m, however the Tevatron enjoys significantly more advanced magnets. The Tevatron uses liquid helium cooled super-conducting magnets to accelerate the proton/antiprotons to their final energy. At the time of the data acquisition for this analysis the Tevatron enjoyed the prestige of being the highest energy particle collider ever constructed.

2.1.6 Antiproton production

A crucial element in this process that has so far been overlooked is the mechanism employed in producing the antiprotons ($\overline{p}$) used in the collisions. High energy protons (120 GeV) are directed from the Main Ring onto a nickel target. These protons interact with the nickel nuclei and produce a spray of

particles, some of which are 8 GeV antiprotons. The particles produced from the proton/nickel interaction are then passed through a lithium lens, which is basically a lithium cylinder carrying 0.5 x10^6amps of current. The lithium cylinder acts as a focusing magnet which focuses the charged particles along the axis of the cylinder.

A pulsed dipole magnet selects the 8 GeV antiprotons from the particle stream and directs them into a "debuncher" ring which acts to reduce the longitudinal and transverse spread of the beam, thus making a uniform momentum spread across all the antiprotons. The antiprotons are stored in the Accumulator ring from which they can be injected into the Main Ring for subsequent acceleration and injection into the Tevatron.

The production rate of antiprotons is very small: approximately 10^7 antiprotons are produced from 10^{12} incident protons. Thus it is necessary to store antiprotons until enough have accumulated for a full physics run. The antiprotons stored in the accumulator ring are called a *stack.* It may take more than a day of antiproton production in order to collect a stack of antiprotons of sufficient quantity for a useful physics run if no antiprotons are present in the accumulator to start with. During normal Tevatron operations, the particle bunches in the Tevatron usually last long enough to allow the stack to be replenished by the MR before a full stack is again needed.

2.1.7 Luminosity at the Tevatron

For meaningful measurements of reaction rates it is often convenient to use the concept of *luminosity and cross section,* represented as $\mathcal{L}$ *and* σ respectively. The cross section of an interaction is analogous to how likely it is to happen. The term historically has its root in the initial experiments

in particle physics where interactions were thought to have a probability that varied with the physical size of target particles. To reflect this thinking the standard unit of cross section is the barn (b) (as in "hitting the broad side of a..."), with 1b = 10^{-24} cm^2, a barn has units of area. The barn is a very large unit for high energy physics and often cross section are reported in milli-barn (mb=10^{-3} barns) or pico-barn (pb=10^{-9}barns).

Instantaneous luminosity ($\mathcal{L}$), or the measure of the particle flux, compliments cross section. For a given reaction of cross section σ the rate of reaction (R, events per second) is given by,

$$R \equiv \sigma * \mathcal{L} \tag{2.1}$$

Thus $\mathcal{L}$ must have units of cm^{-2}s^{-1}. For the 1993-1995 runs of the Tevatron typical runs had instantaneous luminosities ranging from $5 \times 10^{30} cm^{-2} s^{-1}$ to about $25 \times 10^{30} cm^{-2} s^{-1}$. This luminosity decreases over time for each store as the bunches in the Tevatron are subjected to interactions. Typically, when the instantaneous luminosity reaches $8 \times 10^{30} cm^{-2} s^{-1}$ the store is aborted and a new store is produced for interactions.

To measure the total flux of beam during a given experiment it is useful to integrate the instantaneous luminosity over the time that data was obtained. The total integrated luminosity for the trigger used in this analysis, the JET_2_MISS[1] trigger, obtained an integrated luminosity of $92.9 pb^{-1}$.

[1]The JET_2_MISS trigger will be discussed in section 3.1.

2.2 The DØ Detector

The observation of high energy particle interactions can not be observed by the naked eye, nor would it be desirable to be in close proximity to such radioactive interactions. It is then the job of physicists to construct a device capable of recording the interesting characteristics of the interaction. The DØ detector is just such a device and a marvel of engineering and science. Weighing 5,500 tons and having 120,000 readout channels the DØ detector is a general purpose detector with 4π angular coverage. It was designed with an emphasis on superior energy measurement (calorimetry) and muon identification.

To preface any discussion of the detector it should be noted that collider detectors use a special coordinate system to describe positions within the detector. Although the coordinate system is based on a right handed system (where +z is down the beam pipe in the proton's direction, +y is pointing upwards and +x is directed toward the DØ assembly building, outward from the ring), these coordinates are generally changed to a more convenient set of parameters. Figure 2.3 shows how the coordinate system is transformed. The parameter η is called the pseudorapidity. Pseudorapidity is an low mass approximation to the rapidity angle which is defined by:

$$y \equiv \frac{1}{2}\ln\left(\frac{E+p_z}{E-p_z}\right) = \frac{1}{2}\ln\left(\frac{1+\beta\cos\theta}{1-\beta\cos\theta}\right) \tag{2.2}$$

where E, p_z and β are the object's energy, momentum in the z-direction and the standard relativistic term β, $(\frac{v}{c})$. Taken in the limit where the rest mass energy is small compared to the kinetic energy of the object, it is easy to see that

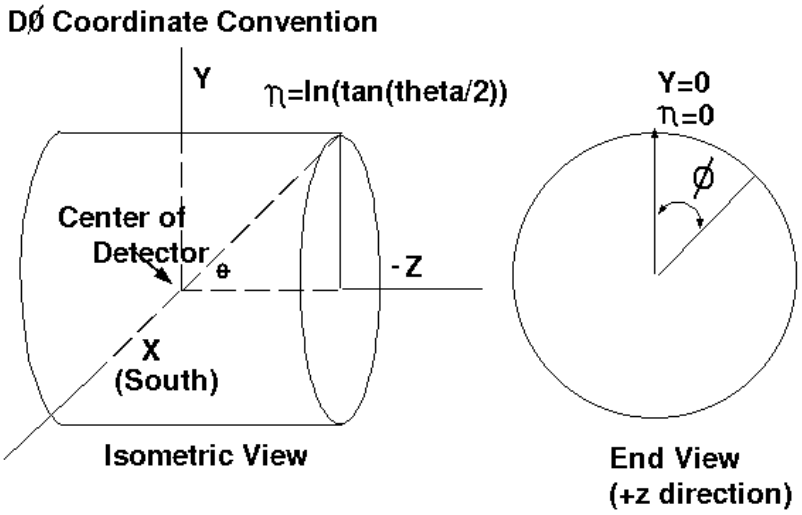

Figure 2.3: The DØ coordinate system.

$$\lim(m \ll E)\, y \rightarrow \eta = -\ln(\tan(\frac{\theta}{2})) \tag{2.3}$$

In this limit, rapidity (an energy dependent term) is approximated by pseudo-rapidity (a purely geometric term).

2.2.1 Detector Subsystems

To successfully instrument high energy reactions the DØ detector is comprised of several different subsystems whose design is driven by the basic underlying physics that they measure. The various portions of the detector can be categorized by their proximity to the reaction. Comprising the DØ detector is the central detector, the calorimeter and the muon system, each of which has several subsystems of its own.

2.2.2 The Central Detector

As its name implies, the central detector is located at the core of the DØ detector and its main purpose is to identify charged particles within the proton-antiproton collision, locate the point of interaction and track particle tracks as they pass through the detector. The central detector in Run 1 lacked a magnetic field, thus the central detector could not resolve charged particle momentum, rather the central detector employed drift chambers and transition radiation detectors to identify charged particles and their point of origin.

2.2.2.1 Vertex Detector

As figure 2.4 shows, the detector closest to the beam is the vertex drift chamber (VTX). The VTX detector uses wire drift chambers to determine

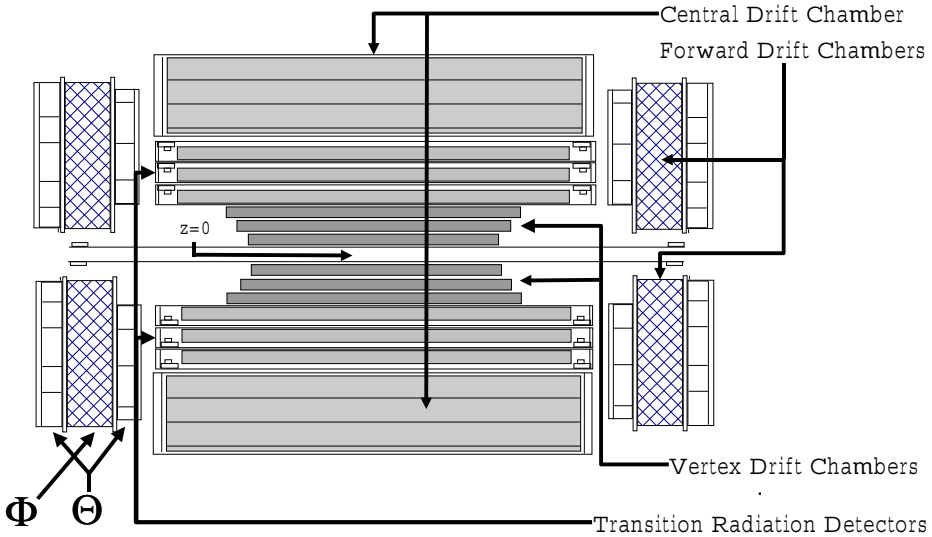

Figure 2.4: The DØ central detector.

charged particle position. A drift chamber contains a diffuse gas in a uniform electric field. The passage of charged particles creates ionization within the gas and thus a trail of charged particles. The electric field attracts the negatively charged particles to sense wires, where they create a current spike upon collision with the wire. By timing the particles as they traverse the gas, as well as knowing the properties of the gas (and thus the drift speed of the particles) it is relatively easy to determine the position of the passing charged particle. The VTX used 95% CO_2/5% C_2H_6 gas mix with a small admixture of water at 1 atmosphere of pressure. The drift velocity for this gas is a fairly slow ($7\frac{\mu m}{ns}$) enabling a good spatial resolution of $60\mu m$ in the r-ϕ plane and 1.5cm in the z direction [11].

2.2.2.2 Transition Radiation Detector

The Transition Radiation Detector (TRD) resides just outside the VTX. Its primary function is electron identification and the discrimination of electrons from $\pi^0 \rightarrow 2\gamma$ decays or direct photons.

The TRD detects the transition radiation caused by a relativistic charged particle crossing the interface between two materials with differing dielectric properties. (In the DØ environment this radiation is mostly X-rays with energies corresponding to 8 keV and largely less than 30 keV.) The TRD has a rejection factor of 50 against pions with 90% efficiency for isolated electrons [13]. The TRD is mentioned here for completeness as it does not play a significant role in the present analysis.

2.2.2.3 Central Drift Chamber

For the present analysis it is crucial to determine the primary vertex of interaction since missing energy can be erroneously introduced into any event where the vertex was misplaced. The Central Drift Chamber (CDC, figure 2.5) covers a region of $|\eta| \leq 1.2$ and provides crucial information about charged particle tracks immediately before interactions with the calorimeter.

The CDC is comprised of 4 concentric layers of drift cells with 32 cells per layer that form long strips of detecting media. Cells in consecutive layers are offset in ϕ by a half-cell in order to distinguish between left-right ambiguities that arise in track identification as well as helping in pattern recognition in the tracking algorithms. Each cell in the CDC has seven (7) sense wires to determine r-ϕ positioning. Near the sense wires are fourteen (14) grounding wires to ensure the uniformity of the electric field. Delay lines near the ends of the sense ground wire planes are used to determine z-positioning. The CDC can resolve tracks with a spatial resolution of ~2mm.

2.2.2.4 Forward Drift Chambers

The Forward Drift Chambers (FDC, see figure2.6) are located on either end of the central detector apparatus and cover the large angle region of the central detector ($1.5 < |\eta| < 3.1$). Each FDC is comprised of three distinct chambers stacked along the z-axis (beam pipe). The middle member of these chambers (called the Φ chamber) has 36 cells with 16 sense wires running radially to measure the ϕ-position of the track. The inner and outer chambers of the FDC (called the Θ chambers) have 24 instrumented cells located in 4 quadrants, 6 cells each, with wires traversing the azimuthal direction. The Θ

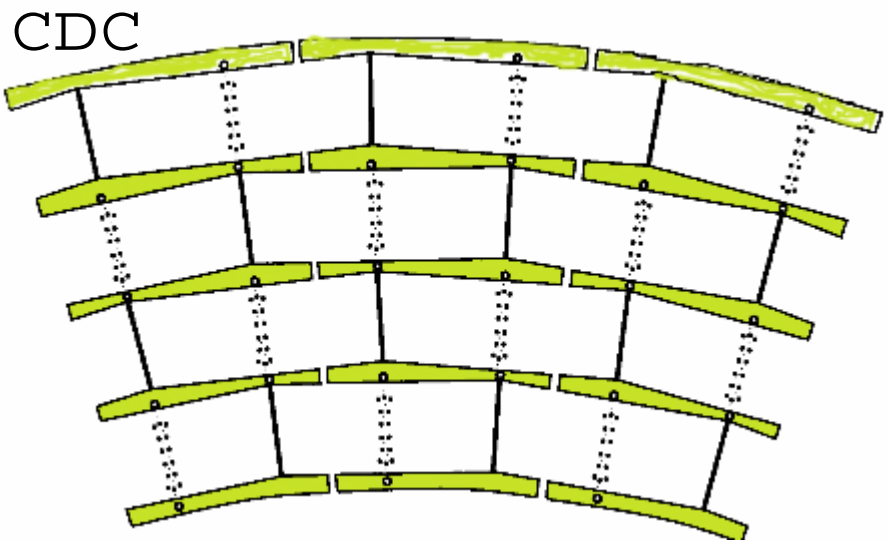

Figure 2.5: An end view of a single quadrant of the Central Drift Chamber. The CDC would extend into and out of the page.

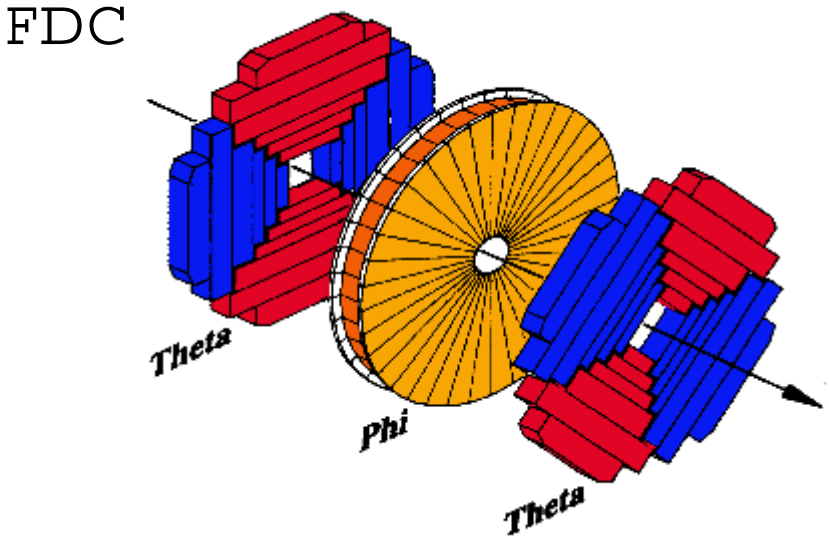

Figure 2.6: The Forward Drift chambers. These detectors are mirrored on either side of the interaction region within the DØ detector.

chambers measure the polar angle of tracks. The inner and outer Θ chambers are rotated by $\frac{\pi}{4}$ with respect to one another to help improve pattern recognition. Delay lines similar to those employed in the CDC are included in each cell of the Θ chambers to help with measuring the position of hits within member cells. The two track spatial resolution of the FDC detectors is ~2mm.

2.2.3 The Calorimeters

The true strength in the DØ detector when compared to its contemporary counterparts is its energy resolution and measurement. The lack of magnetic field in the interaction region and surrounding tracking detectors makes momentum measurement of inner tracks impossible at DØ and thus the importance of precise energy measurement within the calorimeter cannot be stressed enough. The collection of sub-detectors that provide the energy measurements at the DØ detector are the calorimeters. The calorimeters provide a full 4π solid angle of coverage over the interaction region (or as near as can be accomplished while allowing for engineering considerations such as the passage of the beam pipe and detector support structures). Each cell of the calorimeters follows the same basic design to allow for uniform response over all cells regardless of particular cells location in the detector.

The basic unit cell of the calorimeter is shown in figure 2.7. High Z absorber plates are grounded and immersed in liquid argon (at 78 Kelvin, -319 degrees F). The instrumentation is accomplished with a pair of signal boards comprised of two laminated sheets of 0.5 mm thick G10. Electronically cells that are located at the same η and ϕ are ganged together to form a single readout tower. These readout towers are shown in figure 2.8.

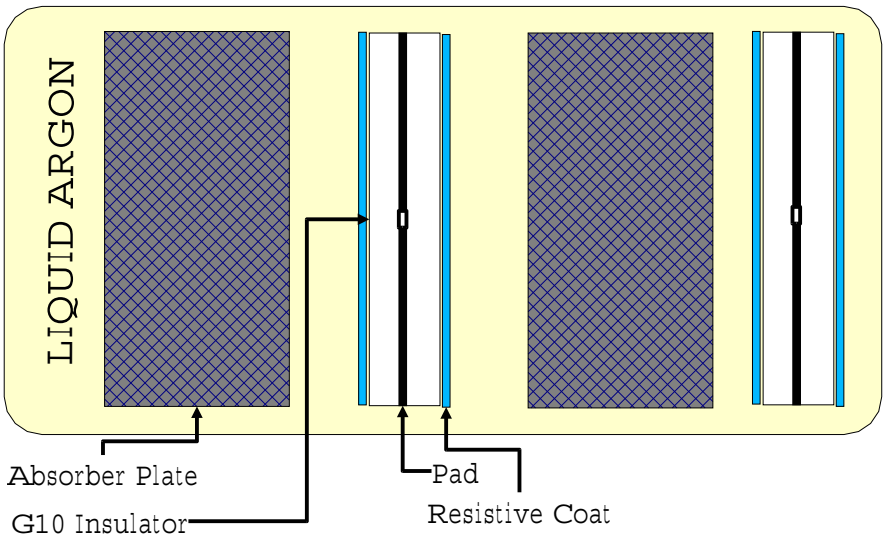

Figure 2.7: A single calorimeter cell in the DØ calorimeter. The elements on the right side of the cell are identical to those labeled on the left. Particles traverse the cell from left to right to allow them to interact with the absorber and then be read out by the electronics.

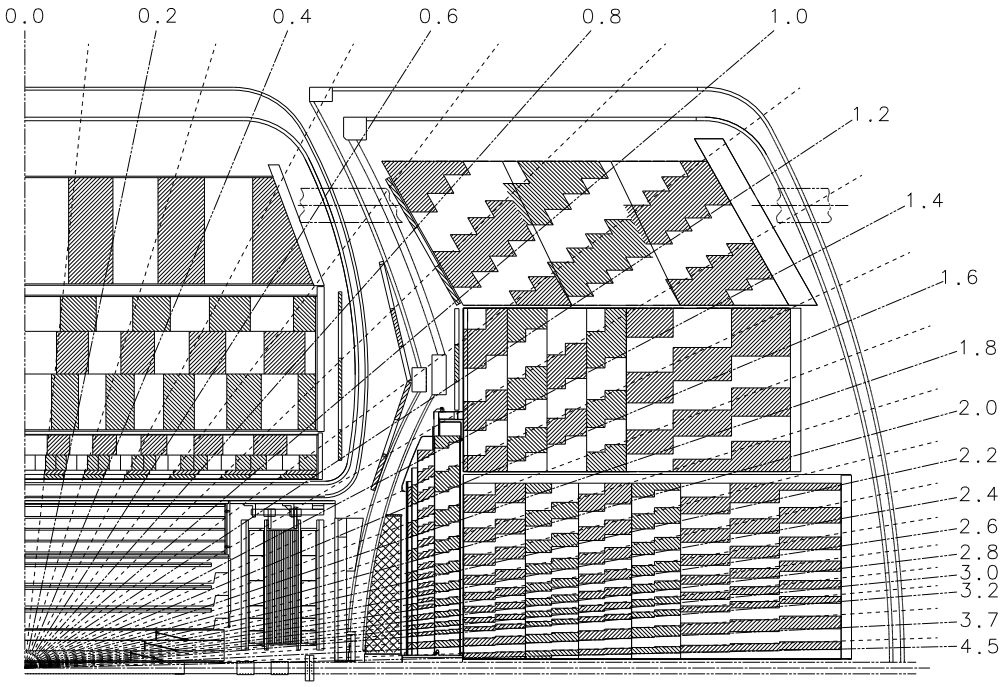

Figure 2.8: The calorimeter readout towers in the DØ detector. The central and endcap calorimeter are both shown.

2.2.3.1 The Central Calorimeter

The calorimeter is not a monolithic device, but rather it is comprised of subsystems designed to accomplish different physics measurements. The central calorimeter (CC) has three distinct layers distinguished by their proximity to the beam pipe.

The electromagnetic (CCEM) section in the CC consists of 32 modules and located nearest the beam pipe. Each CCEM module contains 21 radial cells arranged in four readout layers. Each layer is offset from the previous layer to remove cracks in the detector that would arise from aligned layer edges. The primary purpose of the CCEM calorimeter is to measure the energies of photons and electrons. The absorber plates in the CCEM are 4mm ^{238}U with the third layer in the CCEM located at a radiation depth corresponding to maximal EM shower likelihood. It is for this reason that, unlike the other layers in the CCEM in the CC which have an $\eta \times \phi$ segmentation of 0.1×0.1, the third layer has a finer resolution of 0.05×0.05. This finer resolution in the third layer helps to distinguish between electrons and hadronic showers.

The intermediate section of the CC is the Fine Hadronic (CCFH) section. The CCFH modules are located in three readout layers, each having 15 to 20 radial calorimeter cells with a total of 50 calorimeter cells for the module. The absorber plates in the CCFH layers comprise a total of 3.2 radiation lengths of material, thus the bulk of hadronic showers are measured here.

Completing the CC is the coarse hadronic (CCCH) detector. The CCCH is comprised of a single readout layer of nine calorimeter cells and is also 3.2 radiation lengths deep. The CCCH detects the tails of very hard showers to reduce energy loss through deep penetration.

2.2.3.2 The End Cap Calorimeters

Located at either side of the CC and housed in their own cryostats are the End Cap calorimeters (EC). These two detectors are mirror images of one another and serve to detect shower energies that fall in a range of $1.4 \leq \eta \leq 4.5$. The EC calorimeters share some commonalities with the CC in that they also have a finely segmented inner hadronic region (ECIH) and a much coarser middle hadronic (ECMH) region, much like the EC and CH. The EC also contains the outer hadronic section (ECOH) which is comprised of 46.5 mm stainless steel absorber plates. The ECOH helps to detect the tails of hard showers and reduce punch-through.

The EC also contain the forward electromagnetic (ECEM) section. The ECEM is comprised of two circular modules that cover a theta range of $3 < \theta < 27$ degrees.

All the cells in the EC have a resolution of 0.1x0.1 in $\eta \times \phi$ space except in the following cases. In the ECEM and the ECIH where the resolution must be reduced to 0.2x0.2 at $\eta \geq 3.2$ (due to the small cell size that would be required for resolution at regions that forward. Resolution is increased to 0.05x.05 for $\eta < 2.7$ in the third layer of the ECEM to help distinguish electrons from hadronic showers.

The entire calorimeter is shown in figure 2.9.

2.2.3.3 The Massless Gap and Inter-cryostat Detectors

Located between the CC and the EC is a region of un-instrumented material that is in place to support the massive detector. This region of the detector is called the inter-cryostat region (ICR) and it creates a difficult prob-

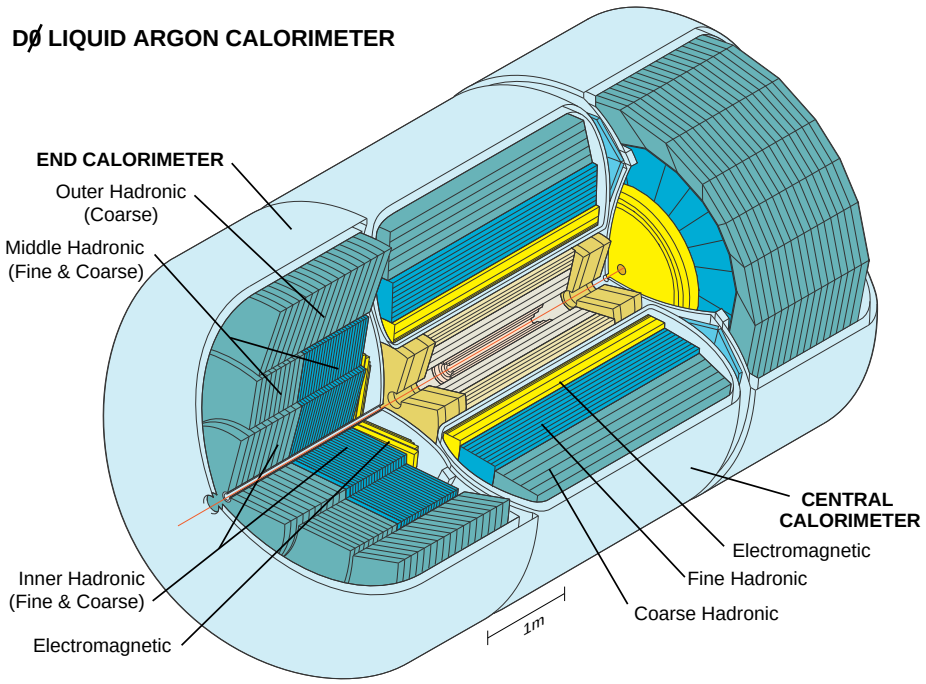

Figure 2.9: The DØ calorimeter shown in an isometric cut-away.

lem for the present analysis in that energy resolution in this region is quite poor. Two different types of detector are installed in the ICR to measure the energy of jets propagating into the region

The first type of detector placed in this region consists of calorimeter readout boards without absorbers. The lack of absorber gives these detectors their distinctive name, the Massless Gap (MG). These detectors sample shower energies before and after they pass through the inert material in the detector structure.

The second type of detector are the inter-cryostat detectors (ICD). The ICDs consist of 384 scintillation counter tiles placed on the front surface of each EC cryostat. These scintillating tiles are readout by 1.3cm phototubes.

2.2.4 The Muon System

The most physically imposing detector subsystem of the DØ detector is the muon system. The massive nature of the muon system is dictated by the penetrating properties of muons. Muons do not react strongly with material and thus easily pass through large amounts of matter before interacting, and rarely produce an EM shower. The muon system fully encompasses the DØ calorimeter as show in figure 2.10. The large radiation depth of the calorimeter itself should allow only muons to pass through to the muon system.

As with the calorimeter the muon system is comprised of subsystems, the wide angle muon spectrometer (WAMUS) and the small angle muon spectrometer (SAMUS). Both the WAMUS and SAMUS utilize proportional drift tubes (PDT) in three layers to detect muons.

The WAMUS itself is comprised of several separate magnets as well as the detectors themselves. The WAMUS magnets are the central toroid (CF)

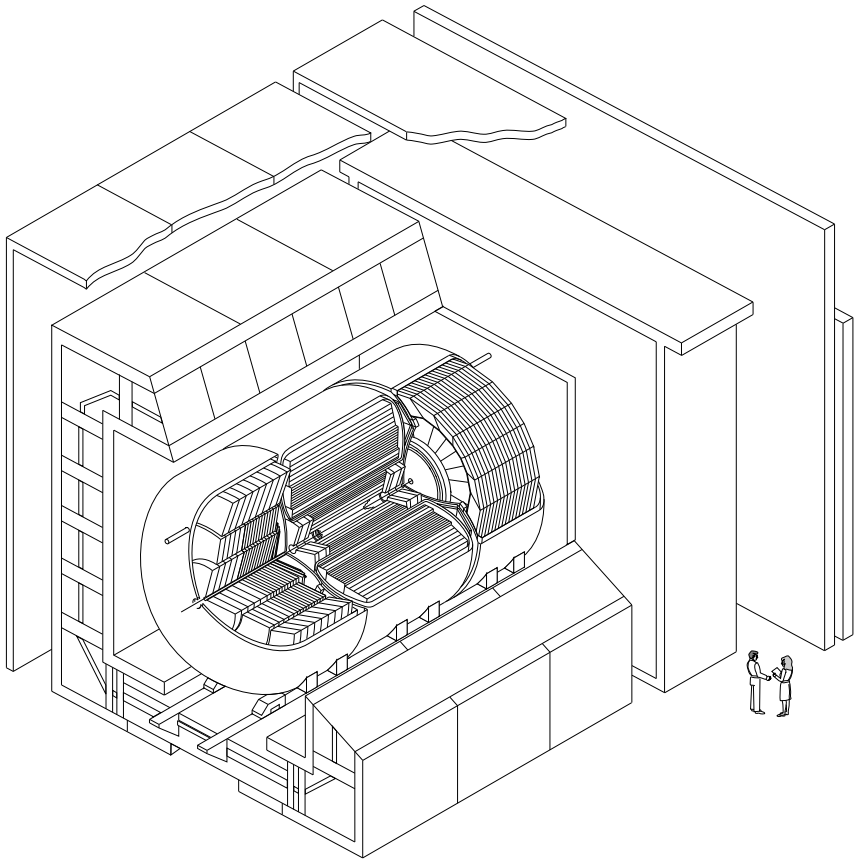

Figure 2.10: The DØ detector shown to scale with two average physicists. The calorimeter is located in the center of the large muon system.

and the two end toroids (EF). The CF magnets cover an η range of $\eta < 1.0$ and weigh in at an impressive 2000 metric tons. The EF magnets cover the range of $1.0<\eta<2.5$ on both side of the detector and each weigh 800 metric tons. A current of 1900 Amps generates a 1.9 Tesla magnetic field in the iron to deflect the muons to allow for momentum measurements.

The SAMUS magnets carry a current of 2000 Amps and have a 2 Tesla magnetic field. The SAMUS has an η coverage in the forward portion of the detector and encompasses the region of $2.5<\eta<3.6$.

As a whole the momentum resolution for the muon system is quite good and given as a function of muon momenta:

$$\left(\frac{\sigma(\frac{1}{p})}{\frac{1}{p}}\right)^2 \approx (0.18)^2 + \left(\frac{0.001p}{1GeV}\right)^2 \tag{2.4}$$

where p is the muons momentum. The constant term of 18% arises due to scattering induced deflections from multiple scatterings in the iron itself. The linear term is due to the position resolution of the muon since the muon position must be well known to determine track bending.

2.2.5 Level 0 Detector

On the face of each EC is a an array or hodoscopes that provide a baseline trigger for the DØ detector. These hodoscopes are collectively called the Level 0 (L0) detectors. Not only do they provide a trigger event for beam crossings but they are crucial in luminosity calculations, the detection of multiple interactions and in the positioning of the interaction vertex.

2.3 Detector Summary

The DØ detector is a highly complex system of smaller detector subsystems difficult to describe in one place. What was given in this chapter should be seen a general overview of the points of interest about the detector. More curious readers should consult more comprehensive discussions of the detector such as reference [16].

Chapter 3

Data

The large rate of interactions at the Fermilab Tevatron along with limited bandwidth and storage capabilities make it is desirable that intelligent choices be made as to whether any given interaction be recorded to tape. The decision making process that the experiment undertakes to reduce the overwhelming input of events (some 350,000 Level 0 events a second) from the detector to the data set is called the trigger. The trigger is a set of online programmable thresholds for determining whether any given event is written to a permanent storage media. DØ uses several different sets of trigger rules to collect events meeting several different physics criteria. The trigger used in the present search is called the JET_2_MISS trigger, which was designed to record events with two (2) hadronic jets and missing energy. The trigger structure as well as the implementation for this study are described in this chapter.

3.1 Triggering at DØ

Three levels of trigger were used in this analysis. Figure 3.1 shows a flowchart for data passing through the DØ trigger framework. Each level of the trigger is described in the following sections.

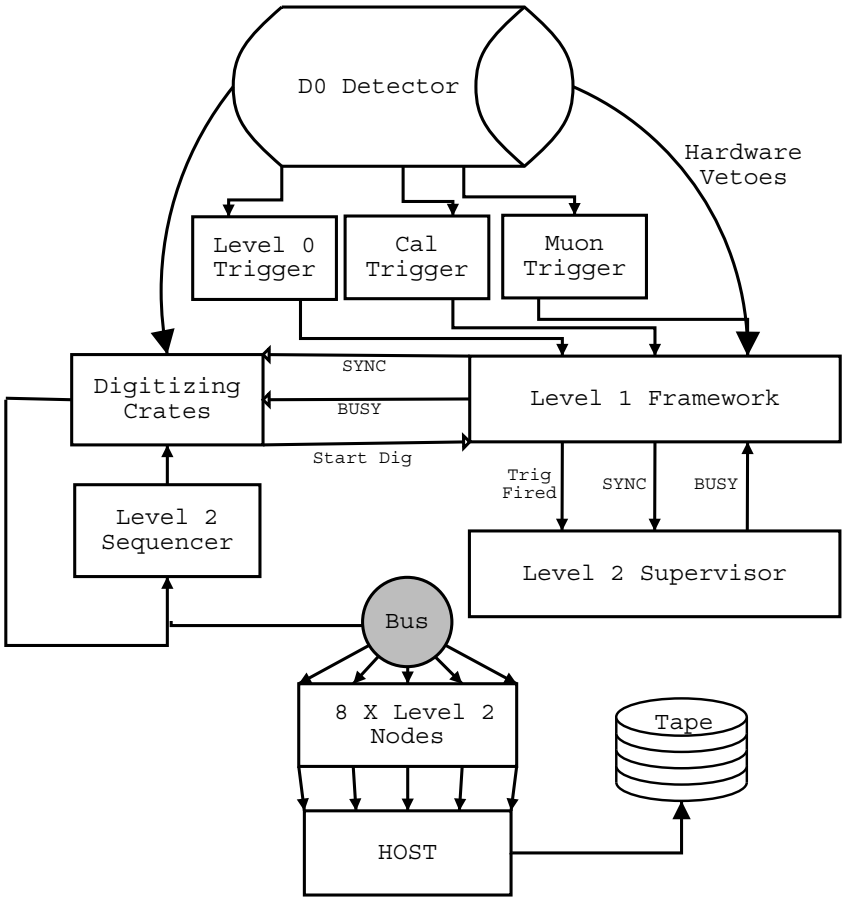

Figure 3.1: Flowchart of the DØ triggers.

3.1.1 Level 0

The Level 0 (L0) detectors (described in section 2.2.5) form the basis of the first triggering mechanism at DØ . The Level 0 scintillator hardware indicates to the experiment that an inelastic collision has occurred in the interaction volume of the detector. Located at the very forward portions of the experiment (partial coverage in ϕ between $1.9 < \eta < 3.9$ and full azimuthal coverage between $2.3 < \eta < 3.9$) the Level 0 detectors are positioned in such a way to intercept the elastically scattered remnant of $p\overline{p}$ hard interactions. (This remnant is comprised of quarks and gluons which did not participate fully in the collision and hadronize into very forward jets. These particles are often called spectator quarks.) The Level 0 hardware also generates an estimate of the z-position of the interaction. This position is passed to the other triggers as an L0 trigger term. A vertex calculated in the first 800ns is reported, called the FastZ, which has a resolution of 15cm. A more reliable value, available 2.1μs after the interaction, called SlowZ, has a resolution of 3cm. Both these vertices are calculated by determining the timing difference between signals reaching opposite ends of the calorimeter. The FastZ is used by calorimeter and muon hardware triggers to calculate estimated E_T and p_T in the event. SlowZ is passed to the Level 2 only if the event is accepted by Level 1. Soft underlying events occurring in the same beam crossing (called a multiple interaction) can make these vertex terms unreliable as the timing becomes somewhat confused. In these cases L0 sets a multiple interaction flag in the event. The L0 system has a timing resolution of 226ps and is greater than 99% efficient for detecting non-diffractive inelastic collisions.

3.1.2 Level 1 (Hardware Trigger)

The Level 1 (L1) trigger framework is a term applied to a very complex system of hardware devices that work in conjunction to set several on/off flags in the trigger. Input into the L1 trigger framework are 256 trigger terms. These terms consists of a binary bit set to yes or no depending on pre-programmed conditions. The majority of these signals come from special L1 processors, but may also consist of signals from particular detector subsystems or from the Tevatron itself (see the following subsections). The 256 trigger terms are then reduced to 32 trigger bits. Each trigger bit was set by combining trigger terms.

The L1 trigger framework also carries the ability to prescale a given trigger. Prescaling allows only a certain fraction of events meeting any given trigger condition to pass. Prescaling was used on the very loose triggers (such as JET_30) since the vast number of events passing these trigger conditions would swamp the available bandwidth and storage devices. As an example, the JET_30 trigger was prescaled such that only 1 in 100,000 JET_30 events were written to tape (even highly prescaled the JET_30 data set contains ~1.5 million recorded events).

The L1 system was designed to operate within the $3.5\mu s$ time between beam crossings. Some L1 triggers required several beam crossings to complete their calculations. These L1 triggers are collectively called the Level 1.5 triggers.

3.1.2.1 Calorimeter Level 1

Adjoining calorimeter cells in $\eta \times \phi$ space are added together to form trigger towers. Separate trigger inputs are provided for the electromagnetic

and hadronic portions of the detector. From the trigger towers are produced seven crucial event variables: Global corrected and uncorrected electromagnetic transverse energy (E_T), global corrected hadronic E_T , global corrected total E_T , missing energy ($\not\!\!E_T$), global uncorrected hadronic E_T , global uncorrected total E_T . The E_T and $\not\!\!E_T$ variables are calculated with respect to the interaction vertex provided by the L0 vertex by summing cell by cell information in the calorimeter. Errors in vertexing at L0 will contribute to errors in L1 values for E_T and $\not\!\!E_T$.

3.1.2.2 Muon Level 1

Although the muon system triggering plays little role in this analysis, the muon L1 trigger is mentioned for completeness. The muon L1 trigger is based on the output of all 16,700 drift cells of the muon system. The output of the muon L1 is comprised of 16 L1 and L1.5 trigger bits. These bits represent the number of coarse muon candidates found within the five distinct trigger regions of the muon system (CF, EF north and south, SAMUS north and south).

3.1.2.3 Main Ring Vetoes

In Run 1 the Main Ring (MR) accelerator beam line physically intercepted the upper portion of the DØ calorimeter (at approximately $95^o < \phi < 108^o$ in the upper portion of the CH calorimeter). Every 2.4 seconds the the MR is used to produce antiprotons in the antiproton source facility. As particles pass through the MR some energy may be spilled into the DØ detector. This energy, not from any interactions within the interaction region of the detector, is erroneous and events containing MR activity must be discarded.

Parameter	L1 Trigger Cut	L2 Trigger Cut
Leading Jet	Three (3) L1 towers	25 GeV
Second Jet	Over 5 GeV total in event	10 GeV
$\not\!\!E_T$	20 GeV	25 GeV
Angle $\not\!\!E_T$ and Leading Jet	No L1 requirement	14.3 Degrees

Table 3.1: JET_2_MISS trigger conditions. The Level 1 trigger conditions on the jets merely requires three level 1 towers in the event. These may or may not be associated with any physics jets in the reconstructed event.

To help facilitate this a MR veto trigger is constructed from trigger bits set via MR detector counters located around the MR beam pipe.

3.2 The JET_2_MISS Trigger

The JET_2_MISS criteria are outlined in table 3.1.

The trigger conditions apply to online physics objects and do not readily relate to reconstructed objects. Thus when off-line criteria is applied to a data set created from an online trigger it becomes necessary to determine at what rate the trigger rejects events meeting the off-line criteria. This rate of rejection is referred to as the trigger turn-on. Each criteria in the trigger will carry its own turn-on and are assumed to be uncorrelated.

Once determined the trigger responses will be applied to simulated Monte Carlo events to weigh each Monte Carlo event by its probability of passing the trigger.

3.2.1 Level 2

After events pass level 1 triggering they are passed onto the level 2 trigger farm. The level 2 trigger is a set of criteria based on filters looking for specific physics signatures. These filters were designed to have good ac-

ceptances of physics events but high rejection against average, uninteresting physics.

The level 2 filters are applied by a "farm" of computers. This farm is comprised of 50 DEC VaxStation 4000/60 and 4000/90 microcomputers. These computers and their associated software perform some limited reconstruction of physics events, enough to allow for intelligent filtering. The level 2 trigger reduces the large level 1 output rate of ~200Hz down to 5Hz, a rate compatible with tape write capabilities.

It is a level 2 that the JET_2_MISS trigger filter is applied to the data.

3.2.2 Jet Trigger Turn-on

The online criteria that was imposed on the event in order to insure two high E_T jets was comprised of both a criteria at level 1 and a separate criteria at level 2. The level 1 criteria required three (3) level 1 towers[1] of at least 5 GeV. The three tower requirement was used as much to reduce backgrounds as to insure large E_T jets.

To determine the acceptance of events with varying off-line jets data taken with various jet triggers (JET_MIN, JET_30, JET_50 and JET_85, see table 3.2)for the trigger conditions of these jet triggers) was used. The large tile requirement for some of these triggers requires a minimum deposit of energy in one quadrant of the detector and makes no requirement on the level 1 towers. These triggers are therefore required to also pass the JET_2_MED trigger.

[1]A level 1 tower is comprised of the electronic readouts of calorimeter cells that align in eta and phi.

Trigger	Level 0	Level 1	Level 2
JET_2_MED		2 (5 GeV Jet towers)	-
JET_MIN		3 GeV Jet Tower	20 GeV Jet Tower
JET_30	Single Interaction	15 GeV Large Tile	30 GeV Jet Tower
JET_50	Single Interaction	15 GeV Large Tile	50 GeV Jet Tower
JET_85		35 GeV Large Tile	85 GeV Jet Tower

Table 3.2: Level 0, 1 and 2 requirements for the Jet trigger samples used in the jet turn-on study. A Large Tile requirement is the demand made on energy deposited in any quadrant of the detector.

The requirement is made that one jet pass the level 1 and level 2 requirements and the rest of the jets in the event are studied to determine the probability of having 2 jets passing the JET_2_MISS jet requirements. This study is performed on three separate portions of the detector that have different calorimeter characteristics and thus different jet response. These sections are the CC, EC and the ICR defined by the eta region of the detector in which the jet propagates. For the trigger studies the CC region was taken to be $\eta \leq 1.0$, the ICR to be $1.0 < \eta \leq 1.5$ and the EC to be $\eta > 1.5$. The tower probabilities are determined as a function of reconstructed jet E_T .

Figure 3.2 shows the probabilities of jets of various offline reconstructed E_T in the event generating 5 GeV level 1 towers. Since our search requires at least two jets the relevant probability is not evident from these plots, but rather a consideration of the cumulative probability given at least two jets. The probability of passing the level 1 jet criteria for a two jet event is given by

$$\wp(trigger) = P_0^1 \cdot P_{3+}^2 + P_1^1 \cdot P_2^2 + P_2^1 \cdot P_1^2 + P_{3+}^1 \cdot P_0^2 + \wp(4+) \qquad (3.1)$$

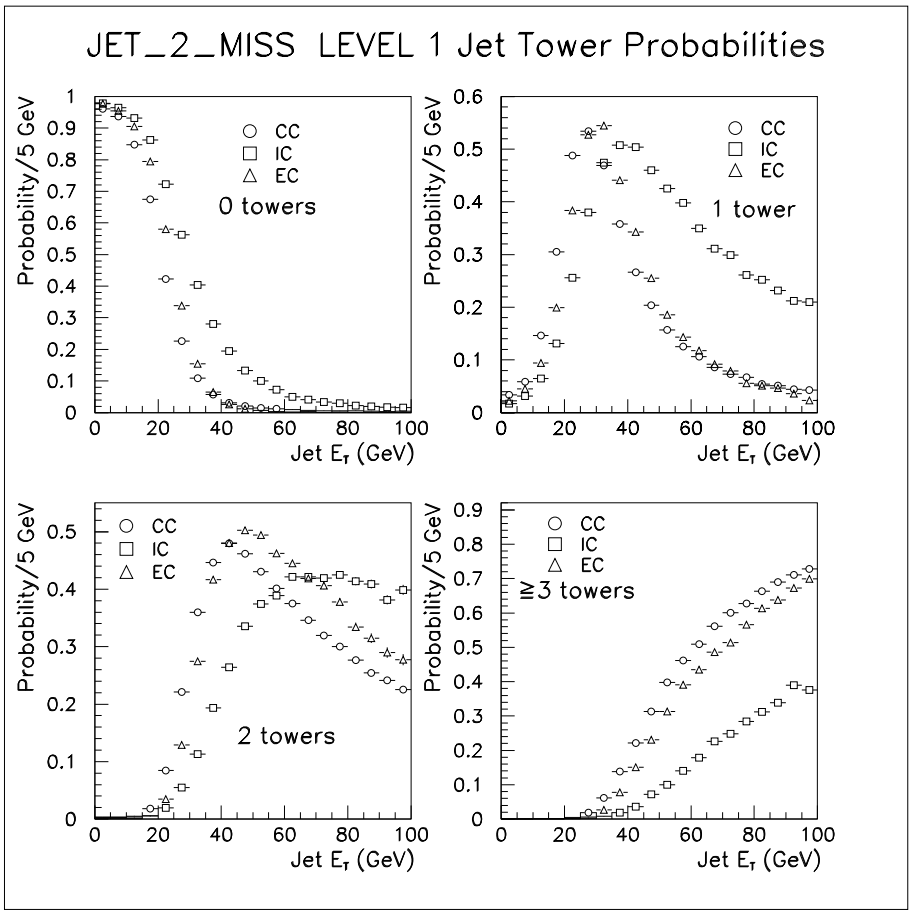

Figure 3.2: Probabilities for jets of various E_T to generate 0, 1, 2 or 3 or more 5 GeV Level 1 towers. Shown in each plot is the probabilities for each portion of the detector.

Using this formula for an event that has two jets in it, we have the Level 1 trigger turn on curve given in figure 3.3.

A large systematic error is introduced into the level 1 efficiency study due to the fact that the there was a bug in the level 1 code that did not correctly account for zero suppression at level 1 [14]. This error places an uncertainty on the actual energy in any given level 1 tower of .25 GeV. The maximal effect of this error is taken into account in the calculation of the level 1 efficiency and is taken to be the dominant systematic error in this method.

The calculation of the level 2 efficiency for the jets was determined using the JET_MIN trigger, again see table 3.2. An additional requirement was made of the JET_MIN events that they contain at least 3 Level 1 towers above 5GeV. At least one jet in the event must pass the Level 2 E_T requirement so that the remaining jets can be studied to determine the Level 2 response for each jets offline reconstructed E_T . This study was also done over the various detector regions with different calorimeter responses. These efficiencies are plotted in figure 3.4.

3.2.3 Angular Trigger Turn-on

The JET_2_MISS trigger was constructed to reduce the influx of un-interesting physics. In earlier searches involving the jets and $\not\!\!E_T$ signature it was noted that common QCD multijet events heavily contaminated the data set when one jet from the interaction region is mismeasured. These events generally had missing transverse energy aligned with or back-to-back to jets in the event. This topological background was so significant that it seemed prudent to do a lose cut on jets back-to-back (in η) with $\not\!\!E_T$ at run time.

This run time cut is expressed in the ACOL (acolinear) cut term in

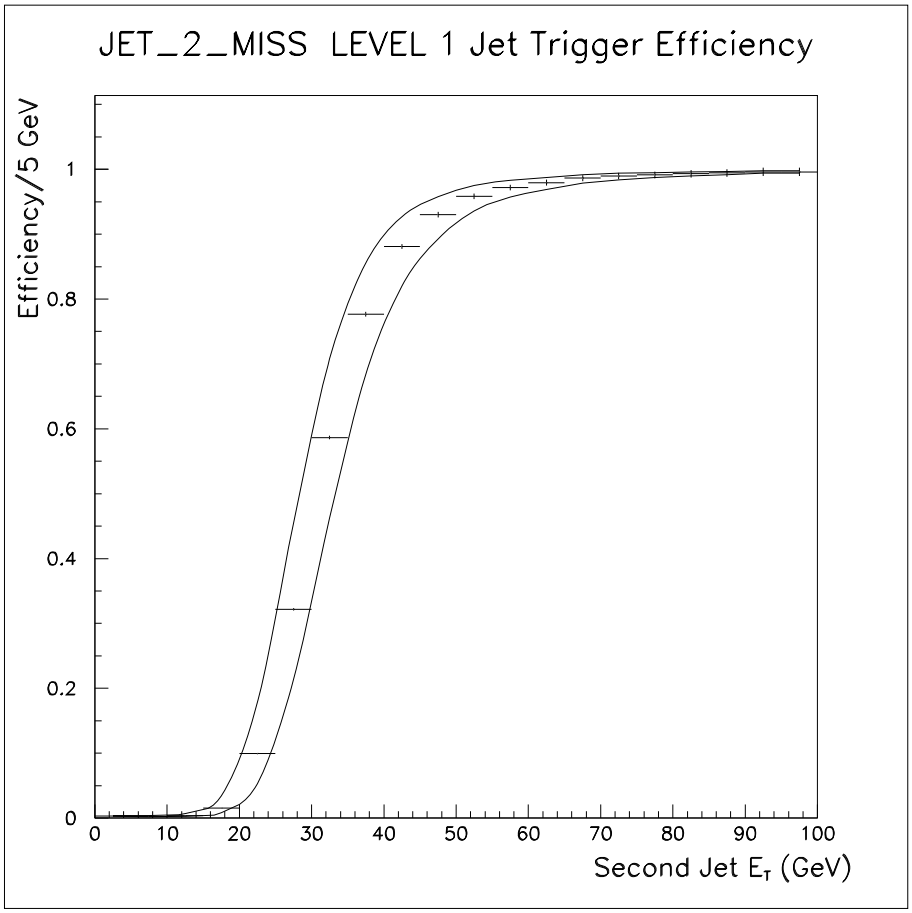

Figure 3.3: The efficiency of the Level 1 trigger term in the JET_2_MISS trigger given a two jet event as a function of second jet E_T .

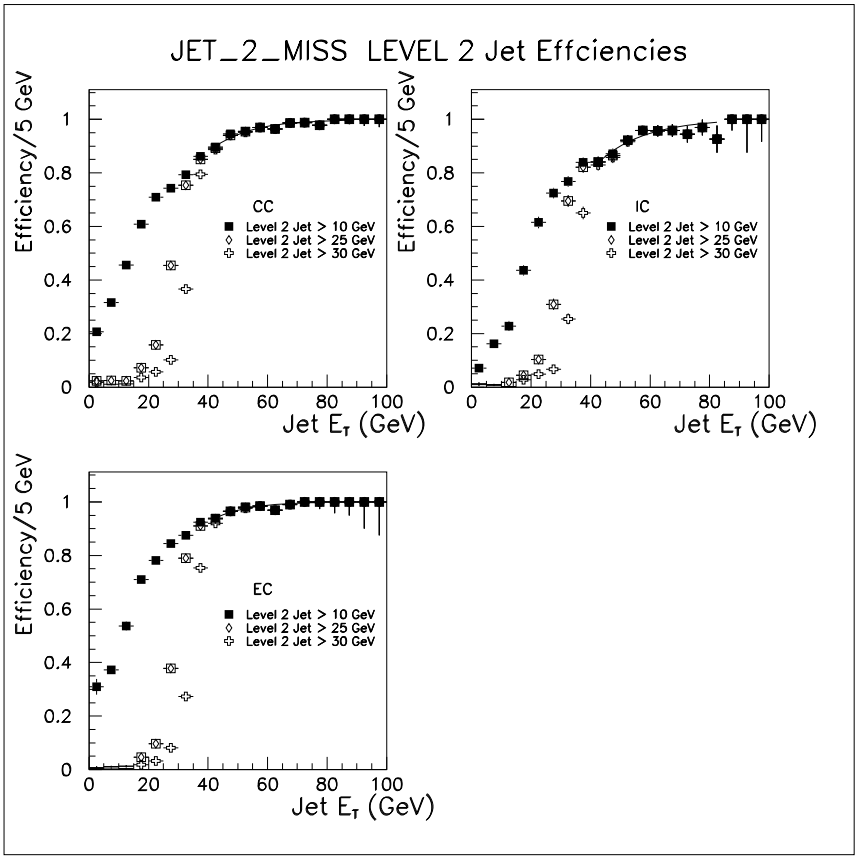

Figure 3.4: Level 2 jet E_T requirements in various portions of the detector. The definitions for the CC, IC and EC regions are the same as used in the level 1 study.

the JET_2_MISS trigger. While this trigger term is very good at cutting down the background the efficiency of trigger term would be very difficult if not impossible to determine. To alleviate this problem a monitor trigger was implemented. The monitor trigger carried all the same criteria except for the ACOL term. This trigger, called the JET_2_MISS_MON trigger, could then be used as a direct measure of the acceptance of the JET_2_MISS trigger. Any event passing the JET_2_MISS_MON trigger would pass the JET_2_MISS trigger and any event not passing the JET_2_MISS trigger would only fail the ACOL term. The acceptance for the back-to-back cut is shown in figure 3.5.

The JET_2_MISS_MON trigger was only implemented during a small subset of the entire Run 1b/1c run time, thus its low statistics preclude its use as the primary trigger for the present search.

3.2.4 Missing Energy Trigger Turn-on

The most difficult trigger turn-on curve to construct is the rejection due to the $\not\!\!E_T$ term in the trigger. $\not\!\!E_T$ is included in the trigger to help filter out events which would be of no use to a search analysis and there-by reduce the overall bandwidth used by the trigger, a resource in short supply at a large collaboration. The $\not\!\!E_T$ trigger terms in the JET_2_MISS trigger is listed in table 3.1. The level 1 and 2 trigger curves can be construct together as a combined data acceptance curve over offline measured $\not\!\!E_T$.

To construct the curve a set of data was produced that had two jets and large missing transverse energy. To accomplish this a trigger sample of JET_3_MON data was selected that contained three large jets[2]. These events

[2]Each jet in the JET_3_MON data had to have jets with $E_T > 20$GeV.

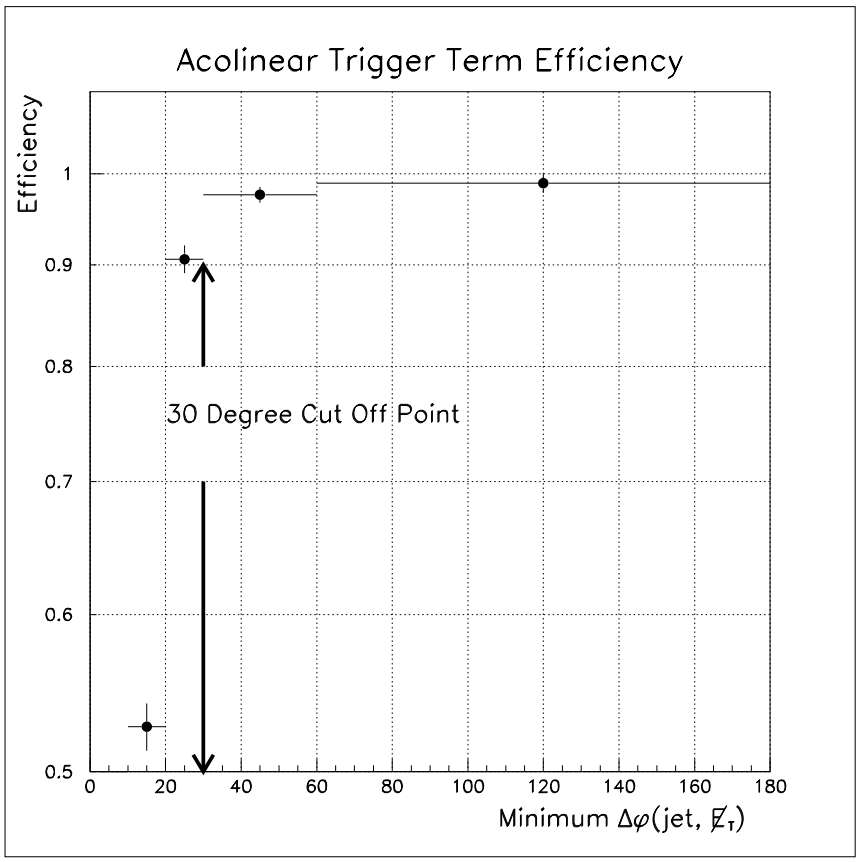

Figure 3.5: The acceptance of the acolinear term of the JET_2_MISS trigger.

were then subjected to an algorithm that effectively erased one of the jets by replacing the output of the cells of the jet with calorimeter noise taken from cells in the event not associated with a jet. Once the cells had been "suppressed" in this manner the events were then resubmitted to RECO for full reconstruction. To remove bias from the sample and to increase statistics in the study the events were recycled so that each event had each of its jets removed creating three simulated events for each real data event. The end results are detector events with a simulated $\not\!\!E_T$ and two healthy jets.

The sample of events are then passed through TRIGSIM, a computer simulation of $\not\!\!E_T$ trigger response. By measuring the number of events passing TRIGSIM versus their reconstructed offline $\not\!\!E_T$ we can determine efficiency of the $\not\!\!E_T$ trigger terms in the JET_2_MISS trigger. The efficiency curve is shown in figure 3.6.

3.3 Reconstruction

A crucial step in experimental high energy physics data analysis is the conversion of the electronic output from the various detector systems to interpreted physics objects. This step, although transparent to the end user, is quite difficult and requires years of work and collaboration from various experts.

The task of reconstruction at DØ is accomplished by a software package called DØRECO or simply RECO. DØRECO interprets the raw data output from the detector (or from simulation of the detector) and converts this output into "high-level" detector objects such as tracks in the tracking, energy clusters in the calorimeters and hits in the muon system. These objects are in

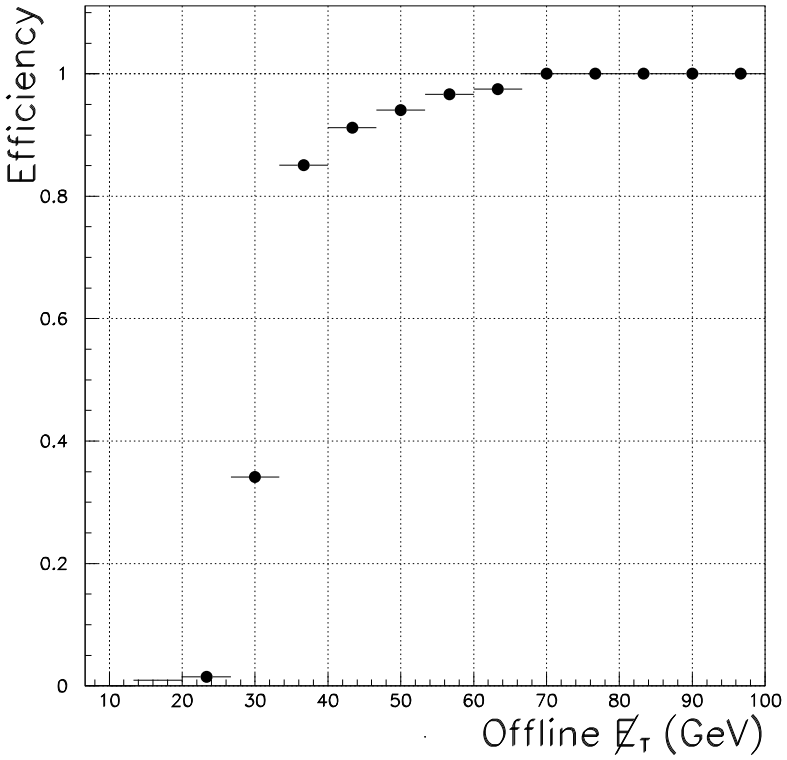

Figure 3.6: The efficiency of the $\not\!\!E_T$ term in the JET_2_MISS trigger (both Level 1 and Level 2).

turn converted in to physics objects such as photons, electrons, muons, jets and missing transverse energy ($\not\!\!E_T$). Certainly DØRECO is much too complex for a comprehensive discussion within this document, however there are several key reconstructions that are needed for an understanding of this analysis in particular.

3.3.1 Jets

Of paramount importance to the search for light stop squarks is the detection of the jets resulting from the hadronization of the charm quarks present in the decay of the stop. Jets are constructed from energy deposited in individual calorimeter cells and combined together via a jet finding (clustering) algorithm. Several algorithms can be employed to find jets within an event however DØRECO uses a method called a "fixed cone" method. The fixed cone uses a fixed cone radius, $\mathcal{R}$. in $\eta \times \phi$ space, where $\mathcal{R} = \sqrt{\Delta\eta^2 + \Delta\phi^2}$. $\mathcal{R}$ describes the maximum transverse radius of the jet. DØRECO reconstructs jets of four various cone sizes $\mathcal{R}$=0.3,0.5, 0.7 and 1.0. The present analysis uses 0.5 cone jets in order to capitalize on data streamed from tapes for use in jet turn on studies which utilized the 0.5 cone jet.

The reconstruction of jets begins with determining energy deposition within the calorimeters. Cells within the detector are assigned indices based on their location within the calorimeter. These indices are based on eta (e), phi (p) and layer (l) locations of the cell with η: -37$\leq e \leq$37, ϕ:1$\leq p \leq$64 and layer:1$\leq l \leq$17. Using this notation, the energy conversion can be expressed as an equation:

$$E_{cell}(e,p,l) = A(d)xW(e,l)xC(e,p,l)xG(e,p,l)xADC(e,p,l) \qquad (3.2)$$

where, A is an overall constant which is dependent on module type (central calorimeter, end cap calorimeter, inter-cryostat detector, central calorimeter massless gap or end cap massless gap detectors). A contains the conversion information from ADC counts to energy in GeV. W is the sampling fraction weight which provides the best energy resolution. W was determined by test beam data. C is all non run dependent corrections such as absorber thickness in the CC and EC, or the ICD minimum ionizing signal corrections. G contains the electronic gain corrections. G is determined from calibration runs. ADC is the digitized cell energy in raw adc counts.

After determining the energy deposited in each cell (as well as whether the cell had any activity at all) the cells are ganged into $\eta - \phi$ towers. This is accomplished by summing over the layer index for all cells. For towers close in proximity to the cryostat boundaries, this sum includes any contributions from the massless gaps and the ICD detectors. These tower energies provide the starting point for jet finding or the *seeds* for the algorithms.

The seed towers, with a minimum of 1GeV of energy, are ordered by decreasing E_T . with the highest E_T seed tower being used as a starting point for preclustering. Smaller E_T seed towers are clustered together with the higher E_T towers that are separated by a distance of 0.3 units in either η or ϕ. After a seed tower is included in a precluster they are then removed from the seed tower list. Any remaining seed towers, starting with the one with the highest E_T , is then used at the starting point for the next precluster. This

process continues until all seed towers are assigned to preclusters. Preclusters are then ordered by their E_T .

To construct the jet cones the E_T weighted centroid of the precluster is identified as the cone axis. All seed towers with in a given cone radius, $\mathcal{R}$, are assigned to the cone cluster. The cone axis is then recalculated using the towers within the cone radius. The cone clusters with an total E_T >8GeV are kept as jets with their jet axis aligned with the cone cluster's E_T weighted axis. After a jet is identified in this manner a process is undertaken to determine if that jet overlays any other. This process is referred to as split/merging.

No jet may contain a calorimeter cell included in any other jet. Thus all jets must be scrutinized to determine if they share cells with other jets. If a jet is found to contain a cell included in another jet the two jets are analyzed to determine if they should be split into two jets or merged into a single jet (thus the term split/merge). First the jet axes of the jets in question are compared. If they are separated by less that 0.01 in $\eta \times \phi$ space then the two jets are considered to be the same jet. If the jets are not found to be the same then the jets are compared by their respective E_T . If the ratio of the E_T of the shared cells is greater than 0.5 (half) the jet's energy then the jets are merged into a single jet. In other words, if the shared cells contain the majority of the jet's energies, then there is considered to be only one jet present. If the majority of energy of the two jets is not contained in the shared cells then both jets are preserved with the shared cells being assigned to the jet that they are closest to in $\eta \times \phi$ space.

Once the population of preclusters have been exhausted the jet properties are assigned to the jet including the jet E_T , θ, η and ϕ.

These constructed jets are not completely correct. There exists an

energy correction method applied to the jets to make up for phenomena such as soft particles in a jet where the energy measurements go non-linear, extensions of the shower outside the jet cone, extra energy deposited in the jet cone from uranium (absorber) noise, spectator events or systematic bias due to zero-suppression of calorimeter readouts. To compensate for these and other errors a technique called Missing Transverse Energy Projection Fraction (MPF) is employed on the constructed jets. To create this correction, events are selected that have a single jet that pass the photon cuts (high electromagnetic content) and a second jet opposite to it in ϕ and no other activity in the event. The EM jet is correct using electron corrections (derived from Z events). The hadronic jet is then corrected so that the $\not\!\!E_T$ in the event goes to zero. Applied over a large number of events a correction factor can be derived that only depends on jet E_T, η, and EM content. Energy out of cone, underlying events and noise were corrected via other studies, mostly using Monte Carlo and minimum bias (loose trigger) events.

This process of jet correction is applied at the NTUPLE level via a software package called NTCAFIX. CAFIX 5.1 was used in the present analysis. It should be noted that NTCAFIX 5.1 repeated corrections already applied to the data. To correct for this error, the correction was removed at the NTUPLE level prior to running CAFIX over the data sample.

3.3.2 Missing Transverse Energy

The parameter of missing transverse energy ($\not\!\!E_T$) is used to identify those object, mostly neutrinos, that escape detection within the detector. The concept is quite simple. Within any collision it is well know that momentum must be conserved. The DØ detector, lacking a magnetic field in Run I, does

not measure the momentum of charged particles nor can the detector measure the momentum of residual particles from the hadronic collision (which are usually very forward). The inability to measure the momenta of particles from the collision in the z-direction and the momentum of charged particles means that DØ must use a parameter similar to momentum, but limited in the scope of the detectors ability. In order to capitalize on momentum conservation DØ approximates this conservation via missing transverse energy. Transverse energy can be defined with the following parameters:

$$\not\!\!E_x = -\Sigma_{e,p,l} E_x(e,p,l) \qquad \not\!\!E_y = -\Sigma_{e,p,l} E_y(e,p,l) \tag{3.3}$$

where $\not\!\!E_x$ and $\not\!\!E_y$ make up the x and y components of a missing transverse energy vector, so that:

$$\not\!\!E_T = |\overrightarrow{\not\!\!E_T}| = \sqrt{\not\!\!E_x{}^2 + \not\!\!E_y{}^2} \tag{3.4}$$

DØRECO computes missing transverse energy as a cell by cell quantity not associating missing transverse energy with any other physics object. $\not\!\!E_T$ in our sample was reconstructed by applying CAFIX 5.1 to the data set and reconstructing the $\not\!\!E_T$ from the energy corrected cells.

3.3.3 Electron Reconstruction

Important to the stop search is the ability to detect electrons so that events containing electrons can be vetoed since the presents of electrons will indicate a presents of a neutrino which would contain a real $\not\!\!E_T$ (more on this in section 5.1).

The showers created in the detector from the presence of an elec-

tron are narrow and deposit the bulk of their energy in the EM layer of the calorimeter, much like photons. The cone algorithm employed in electron reconstruction differs from jet cone reconstruction as it uses a nearest neighbor based algorithm, rather than an E_T based algorithm. The EM towers in a local neighborhood, where a neighborhood is defined as an array of 3x3 towers in $\eta \times \phi$ space, are grouped together into clusters. Towers are included into the neighborhood only if they have an energy of more that 50MeV. Once all the EM towers have been assigned to clusters, they are checked to see if they are an electron candidate. To be an electron (or photon) candidate, the cluster must have the following properties: the total cluster energy must be at least 1.5 GeV, the total transverse energy must also be at least 1.5 GeV, the EM energy fraction ($1 - \frac{E_{hadronic}}{E_{total}}$) must be greater than 90% and the hottest tower must account for 40% of the clusters energy.

Once a electron candidate is identified, DØRECO creates several parameters to help an analysis identify electrons in an event. Without going into much detail, these parameters are the EM fraction, the H-matrix chi-squared, shower isolation fraction and track match significance.

The EM fraction is fairly self explanatory as it is the ratio of the energy deposited in the EM layers divided by the total energy of the jet. Electrons will generally deposit the majority of their energy within the EM layers.

The H-matrix is a fairly complicated parameter constructed by a shower shape analysis that capitalized on the fact that electrons and photons can be characterized by their longitudinal and transverse profiles. The H-matrix is constructed on a shower by shower basis based on a study of Monte Carlo showers passed through the DØ geometry. The χ^2 of the shower basically gives a powerful tool for determining the presence of electron and photon

showers.

The shower isolation provides discrimination between electrons from W and Z events and electrons produced in other physics processes. EM showers occur mostly within a cone of $\mathcal{R}$ =0.2, the isolation fraction variable is defined by:

$$f_{iso} = \frac{E_{total}(0.4) - E_{EM}(0.2)}{E_{EM}(0.2)} \tag{3.5}$$

where $E_{EM}(0.4)$ is the energy in an isolated cone of $\mathcal{R} = 0.4$ and $E_{EM}(0.2)$ is likewise the energy deposited in a cone of $\mathcal{R} = 0.2$.

Finally, electrons are identified by a method of track matching whereby a track present in the tracking lines up with the EM cluster.

3.3.4 Vertex Reconstruction

Of great significance to the analysis presented here is the presence of $\not\!\!E_T$ in the event. $\not\!\!E_T$ is a tricky signal and can be introduced into an event sample by circumstances not related to any interesting physics. One of the more common causes is merely mis-identifying the vertex in the event, the point from which the primary physics objects emanate. A good knowledge of how the vertex is constructed on an event-by-event basis is needed to allow for corrections to the technique to be made.

For the most part the x and y location of the beam in the accelerator is located within a $40\mu m$x$40\mu m$ region that only shifts to a different position due to accelerator realignments and maintenance and it does not change significantly from store to store. The large uncertainty in the vertex location comes from the z position. This position is reconstructed on an event by event basis

since the beam may collide at any point within the detector along the z-axis (although the vertex positions of a large number of events form a Gaussian about z=0).

Although a fast and slow vertex are constructed from the Level 0 information for triggering purposes, a more sophisticated vertex is constructed in RECO using the CDC and FDC tracking chambers. CDC tracks in the event are projected back toward the beam axis and are given a z position of origin based on their closest approach to the beam pipe. If no CDC tracks are present in the event, FDC tracks are used. A clustering algorithm groups tracks that originate from the same point along the z axis. A group of tracks is only classified as a cluster if it has at least three (3) tracks (save in the case where only a single cluster is found). The z position of all the CDC tracks in the clusters are then stored in a histogram, see figure 3.7 for an artists rendition of this process. These histograms are then fit with a Gaussian curve and its mean is taken as the position of the cluster's vertex. The cluster with the most tracks is taken to be the primary vertex if more than one cluster is found in the event. At no time during this process is the calorimeter examined to see if there are energy deposits that can be associated with the tracks. The primary vertex reconstructed in this manner is then used to calculate physics object parameters that depend on the vertex such as E_T , p_T and $\not\!\!E_T$.

In general the vertex identification and reconstruction is very good. If a single CDC track is used in this process a vertex resolution of 2 cm is obtainable. Even if no CDC tracks are present and FDC tracks are used a resolution of 10 cm is reached. If electrons are present in the event and leave tracks in the tracking the vertex resolution and identification is very good, a fact that will be exploited later in the analysis.

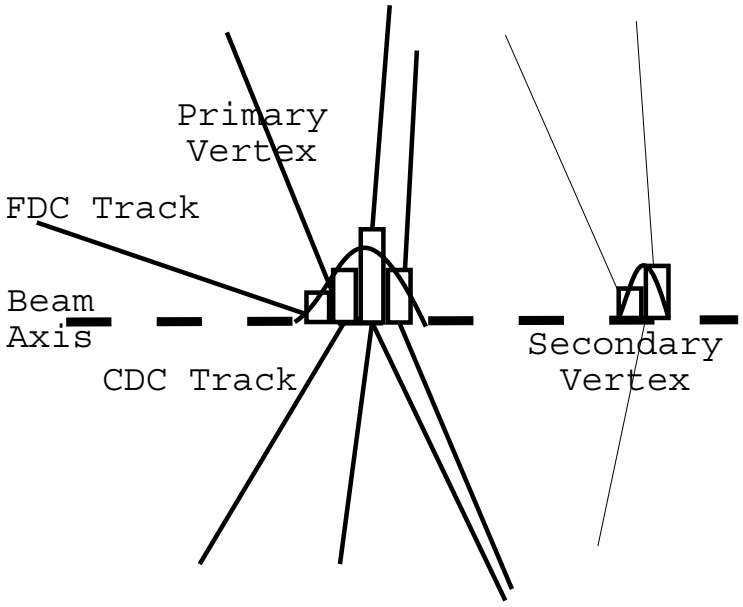

Figure 3.7: Artist's conception of tracks pointing back to the vertex in an event. Shown are two vertices, a primary and a secondary along with an array of tracks and an overlay of their corresponding histograms.

After events are reconstructed via RECO they are ready for analysis.

Chapter 4

Data Cleanup

The sensitivity of the $\not\!\!E_T$ trigger to mismeasured energy in any reaction readily lends itself to contaminating the sample with events that do not contain interesting physics. Great care was taken to remove these events without biasing the data against our signal and to fully understand the effect of this removal has on acceptances, both for signal and background.

4.1 Misvertexing

Since DØ did not contain a central magnetic field, the experiment cannot measure an emitted particles momentum (p_T), also since the particles in the collision are composite particles (protons) it is impossible to determine the true momentum of the actual collision participants. To compensate DØ defines a transverse energy vector, E_T . E_T is simply defined as

$$|E_T| = Esin\theta \tag{4.1}$$

Where θ is the angle take between the direction of energy deposition from the object and z axis (see figure 2.3). The sum of all the E_T within an event should be zero if all the emitted particles from the interaction are detected correctly. This is simply a fact that the momentum in the transverse direction

(to the beam) is zero. $\not\!\!E_T$, arises if a particle is not detected or if there is a mismeasurement of the interaction products by the detector.

If the vertex of the event is mistakenly placed in a different position within the detector volume the E_T of the object would be mismeasured. This mismeasurement of E_T gives rises to an artificial $\not\!\!E_T$. Since the JET_2_MISS trigger preferentially selects events with high $\not\!\!E_T$ misvertexing is a significant source of errant data.

In the previous DØ stop search the problem of misvertexing was removed by requiring a single interaction point. In runs 1b and 1c this technique is simply not feasible. The instantaneous luminosity of the events comprising the run 1b set is much higher than the instantaneous luminosity of the run 1a. This makes the probability of having an underlying event much higher. Requiring a single interaction, in the same manner as in the run 1a analysis, would result in a reduction in the integrated luminosity by as much as 80%. Thus a new method for determining a primary vertex had to be constructed to take advantage of the increased luminosity of runs 1b/1c.

During event reconstruction the vertex was chosen by using a clustering algorithm that groups tracks from the CDC back to the beam pipe. The CDC tracks are not associated with any physics objects that are observed in the final reconstructed event. An improved technique would be to use only tracks that are associated with a jet in the event.

Rather than reconstructing the vertex from scratch, the primary vertex is merely confirmed by the CDC tracks. This is done by utilizing only CDC tracks that are associated with central jets. CDC tracks are first tested to insure that they lie within a .4 $\eta \times \phi$ cone of a reconstructed central ($\eta < 0.8$) jet whose E_T is greater than 20 GeV and passes the standard good jet cuts (see

Jet Parameter	Cut
Absolute value of jet eta	Less Than 1.1
Fraction of jet energy in the EM layer	More than 10% or Less than 90%
Fraction of jet in the coarse hadronic	Greater than 40%
Fraction of jet E_T located in hot cell	Less than 10%

Table 4.1: The good jet cuts made on jets to be used in that tracking algorithm. Tracks associated with jets not passing these cuts are not considered in determining the vertex position.

table 4.1 for a description of a good jet). Those CDC tracks which lie within a good jet's cone are then projected back to the beam pipe and an average z position is calculated using these tracks. The average vertex is then compared to the z position of each track used by calculating the χ^2 of that track. If the χ^2 of a single track is greater than 12.08[1] the track is ignored. All tracks with a χ^2 of less than 12.08 are then used to calculate a new average vertex

The average vertex calculated using the tracks and the primary vertex reconstructed in the event are then used to calculate a new χ^2. If this χ^2 is less than 2[2], then the event is kept.

To determine the effect this cut has on the data a clean sample of $W \rightarrow e\nu$ (WENU) events were studied. The WENU events are useful in that the electron gives excellent vertex resolution (~2cm). To ensure a W event is present a cut is made on the electron and $\not\!\!E_T$ invariant mass such that the mass lies between 70 and 110 GeV. Since these events give a "known" vertex, provided by the electron, an efficiency of the technique can be determined from the sample. Losses in efficiency may occur when at least two tracks are not associated with the central jets. Table 4.2 gives the efficiencies for the data

[1] A χ^2 of greater than 12.08 corresponds to a difference between the track's z position and the average vertex being greater than 20 cm.

[2] A χ^2 of less than 2 in this case is a separation of 7 cm between the primary vertex and the average track vertex.

Jet pointing	Efficiency
Vertexing Efficiency with Jets in ICR	78.2%±2.0%±1.5%
Vertexing Efficiency, Leading Jet central no Jets in ICR	79.51±1.57±1.50%

Table 4.2: Vertex Efficiency

set, the loss of efficiency due to the multi-track per jet is folded in.

4.2 Main Ring

The Run 1 DØ detector was pierced via the Main Ring (MR) accelerator (in Run II the MR will no longer be utilized). Although great pains were taken to reduce the noise generated by incidentals in the MR, the sensitivity of the JET_2_MISS trigger to $\not\!\!E_T$ almost insures that events where there is energy deposited in the MR will contaminate the sample. The online Level 1 triggers carry two trigger terms that were set to indicate that there is activity in the MR. MICRO_BLANK is set to true when the accelerator underwent injection and transition. MRBS_LOSS was set true when protons were passing through the detector. Even with JET_2_MISS requiring these be false, some MR noise escapes veto and is present in the data set.

To remove events passing into the trigger sample via MR activity a main ring cut was utilized over the entire data sample. The cut demands that the absolute value of the E_T deposited along the MR be no greater than 10 GeV.

It may seem odd to also remove negative energy deposition about the MR, however this is to allow for events contaminated by preamp recovery. When there is significant energy deposited in the detectors about the MR it may be several beam crossings before the electronics that read out those detectors recover. In the event that a particular event has 10 GeV in negative

energy accumulated about the MR pipe, the event is discarded. Thus a cut on the absolute value of the QCD_WZ NTUPLE [12] variable MRSUMET of 10 GeV is made on the whole of the data.

The efficiency of this cut was made by studying a portion of the calorimeter not permeated by the MR. Main Ring cells are defined to be cells in the coarse hadronic calorimeter within the detector eta less than 1.4 and $1.6 \leq \phi \leq 2.0$. The amount of jets meeting the same criteria in another portion of the detector can be determined by determining the survival rate for the MR cut in a "control" region where eta remains less than 1.4 but where $3.1 \leq \phi \leq 3.5$. The removal of events having 10 GeV of energy in the MR region removes jet acceptance from the data set. A jet sample, such as those used to calculate the trigger efficiencies (see table 3.2) where a jet has at least 50 GeV of energy in the control region was used to determine the efficiency of the Main Ring cut. The efficiency of this cut is 94.0±1.0% and NO jet in the control region was found to have less that -15 GeV of energy nor more than 200 GeV. To determine the loss of luminosity because of MRBS_LOSS and MICRO_BLANK, these trigger terms were applied to zero bias events recorded every 1/100th of a beam crossing (without bias). The loss of luminosity, 0.24±0.17%, leaves $85.2 \pm 3.7 \text{pb}^{-1}$ from which to search for new physics.

4.3 Cosmic Rays

High energy cosmic rays incident on the detector can deposit energy in the calorimeter that can be erroneously reconstructed as a jet and the imbalance of energy that results from this ray not originating from a $p\overline{p}$ collision gives a false $\not\!\!E_T$. In order to pass the 2 jet portion of the trigger the cosmic

ray would have to radiate a photon in two distinct portions of the detector. To remove events passing the JET_2_MISS trigger that arise from cosmic ray energy deposition the EM fraction of the jet is checked to ensure that it is not consistent with a photon (or electron). Examining typical jet data, acquired using the triggers in table 3.2, the EM fraction of well behaved jets can be determined and compared to those present in the JET_2_MISS trigger sample. The EM fraction, the ratio of the amount of energy in a jet deposited in the EM layer of the detector and the total energy of the jet, of a "well behaved" jet is greater that 10% and less than 95%.

Chapter 5

Analysis

5.1 Backgrounds

With the general conditions that a light stop decay would consist of 2 Jets and $\not{E}_T$ it is very likely that any data selection criteria would contain other events that meet that criteria. These other events could pass the 2 Jets + $\not{E}_T$ conditions due to one of three reasons; these events could be irreducible physics processes which also have a physics signature of 2 Jets + $\not{E}_T$, these events could be physics events which normally do not have 2 Jets + $\not{E}_T$, but due to some mismeasurement of a particular part of the event are mistaken for such or, lastly, the event may pass solely due to gross detector mismeasurement. The prediction of each class of background is discussed in this section.

5.1.1 Monte Carlo Backgrounds

The easiest background to account for in the 2 Jets + $\not{E}_T$ signal are those physics events which share this distinctive detector signal which can readily be simulated from our understanding of standard model interactions. These events arise from the production of vector bosons and contain no charged lepton in the decay or contain a tau which decays into a jet. This category of

event is called irreducible since no set of physics or detector signal cuts will remove these events from the sample.

Another set of backgrounds that can be easily predicted from Monte Carlo are those events which contain a leptonic decay whose leptons are either not detected or fake a jet. Any such event arising from a W boson decay will also contain neutrinos which escape detection. These backgrounds are due, mostly, to the decay of Vector Bosons (VB)

- $W \to e\nu + jets$
- $W \to \mu\nu + jets$
- $W \to \tau\nu + jets$, $\tau \to \ell\nu$
- $W \to \tau\nu + jets$, $\tau \to hadrons$
- $W \to \ell\nu$, $Z \to anything$
- $W \to \ell\nu$, $W \to q\overline{q}$
- $Z \to \nu\overline{\nu} + jets$
- $Z \to \tau\tau + jets$

A VB decay that produces a neutrino and jets where the charged lepton is lost is part of this background. A VB decay that produces a tau and the tau is mis-identified as a jet will be in this sample.

To model the VB backgrounds Monte Carlo generators were employed to create simulated events and then passed though a detector simulator to determine the DØ response to each event. The Monte Carlo package utilized to produce W and Z bosons with a single jet was the PYTHIA (version 6.127)

package from CERN. PYTHIA has within it the ability to hadronize the jets associated with the tree level decay and thus PYTHIA events are passed straight to GEANT (version 3.15), the detector simulation package from CERN.

To produce W and Z events that produce 2 jets[1], the simulation package VECBOS (Version 3.0) was utilized. VECBOS does not have the ability to hadronize its tree level jets so an intermediate piece of software must be used to provide the jets. For this task ISAJET (version 7.37) was used. If any Tau leptons are produced by any of the decays from either the 1 or 2 jet sample the package TAUOLA simulates the tau decay.

Once the decays are produced from the respective software packages the jets from ISAJET and PYTHIA are then passed through PJET to build hadronic jets and impose initial E_T requirements on the jets. Without this initial requirement on the jets, all the events would be passed through the detector simulator (the slowest of the packages) thus monopolizing large amount of CPU time. These initial E_T requirements allow filtering of events needed to pass through GEANT.

Full DØ GEANT takes large amount of resources to process a single event. To facilitate the reconstruction of Monte Carlo jets a large library of jets were produced by the collaboration. This library of jets, SHOWERLIB, gives detector responses for jets requiring only the event vertex, the η, ϕ momentum of the jet and the particle originating the jet.

Once the detector response is modeled by DØ GEANT, the event is

[1]It should be noted that initial state radiation produced by PYTHIA can also create a VB event with 2 or more jets thus giving rise to double counting. To eliminate this double counting the lepton in the event is used to separate the two samples. We only accept W events from the PYTHIA sample when their lepton "fakes" a jet. Thus if the lepton generated in the events is very close to a jet ($0.3>\Delta R$) then the event is kept, likewise if the lepton in the VECBOS sample is near a jet, the event is discarded.

reconstructed by the reconstruction software, DØRECO . DØRECO then takes the output of GEANT and produces the physics objects as they would appear to experimenters. DØRECO has contained within it the Anomalous Isolated Deposit Algorithm (AIDA) which removes "hot cells" from the events. Since GEANT does not model hot cells any cell flagged by the AIDA algorithm was actually present in the event and removal would not be appropriate. Any AIDA flagged hot cell is restored to the nearest jet and the event is passed through the Monte Carlo version of CAFIX to correct jet energies. In data, any event that contains an AIDA flagged event is removed from the data sample before analysis begins.

5.1.1.1 Vector Boson Plus Jets Monte Carlo

It is not a simple task to relate the generated W and Z events to actual physics events, nor is it obvious how often jets will be produced along with the W and Z. To weigh each Monte Carlo event so that it represents a single physics event produced at the corresponding luminosity, the cross section for the reaction has to be determined. This calculation is made by looking at actual DØ W and Z data and measuring the cross sections for W and Z production with 1 or 2 jets.

The triggers utilized for the W and Z cross section study all required a high E_T EM cluster in level 1 and high EM fractions in the level 1.5 trigger. These triggers were designed to accept events containing leptons. The triggers used are outlined in table 5.1.

The EM2_EIS2_HI trigger requires 2 EM objects meeting the EIS requirement (based on shower shape and isolation) and to have a high E_T . In a similar naming convention the EM2_EIS_ESC requires the same (2x)EM

Trigger	Level 1	Level 2
EM2_EIS2_HI	2x(E_T >7 GeV)	2x(E_T >20 GeV, EIS)
EM2_EIS_ESC	2x(E_T >7 GeV)	E_T >20 GeV,1xEIS; E_T >16GeV, 1xESC
EM1_EISTRKCC_MS	E_T >10GeV	E_T >20GeV, EIS, TRKCC; $\not\!\!E_T$ >15GeV

Table 5.1: The triggers used in the W/Z cross section determination. Not listed is a level 1.5 requirement on the EM fraction so that the EM fraction of a jet being greater that 85% and the E_T of that jet being greater than 12 GeV. The TRKCC term indicates that a track is associated with the electron.

and EIS conditions, but requires an "escape" (ESC) electron that does not have the shower shape and isolation requirements. The EM1_EISTRKCC_MS trigger requires a single EM object to pass the EIS conditions and to have a track associated with the electron and a missing energy (MS). This missing energy requirement carries with it "Good Calorimeter" conditions. This was accomplished by vetoing Main Ring (MR) activity flagged by activity in the veto counters located around the MR pipe.

Offline electron identification was made by making requirements on the EM fraction, χ^2 shower shape, track match significance, the $\frac{dE}{dx}$ along the track and on the energy deposited in the transition radiation detector (TRD). These five individual conditions are combined in a single parameter called the electron five variable likelihood (5vl). We also use the electron isolation fraction to identify electrons. Using a sample of $Z \rightarrow ee$ the thresholds for the 5vl and electron isolation can be studied.

The Z boson can be a highly useful tool for experimenters since it can decay to two electrons whose invariant mass is the mass of the Z. From this useful fact the electron efficiency of the DØ detector can be determined (as well as the thresholds for the 5vl and electron isolation cuts) and from there the cross-section of Z+jets and W+jets background events. To produce a sample

of Z→ee events the following requirements were made on the electron trigger sets:

- One Central EM cluster ($|\eta_{detector}| \leq 1.1$), Far from detector crack (see figure 5.1
- Central EM cluster has $E_T \geq$25 GeV
- Central cluster passes EIS, TRKCC trigger term, 5vl and EM fraction identification cuts
- Second EM cluster either in central (as before) or forward ($1.5 \leq |\eta_{detector}| < 2.5$with $E_T \geq$25 GeV
- Invariant mass of the 2 clusters is within 10% of Z mass pole, 82 GeV $\leq M_{ee}*c^2 <$100 GeV.

Once this is set is identified the background of the sample needs to be determined so the electron efficiency can be calculated. The background across the Z pole is, to good approximation, linear and can be accounted for by integrating the number of events on either side (73 to 82 GeV and 100 to 109 GeV) of the peak, see figure 5.2. The survivors of this criteria are used to determine the efficiencies for the 5vl and electron isolation fraction cuts. These are shown in figures 5.3 and 5.4 along with the cut used for selection of electrons in the data.

5.1.2 Z Cross Section

The sample is now distinguished by the second EM cluster. Events having two central EM clusters are designated CC-CC and those containing

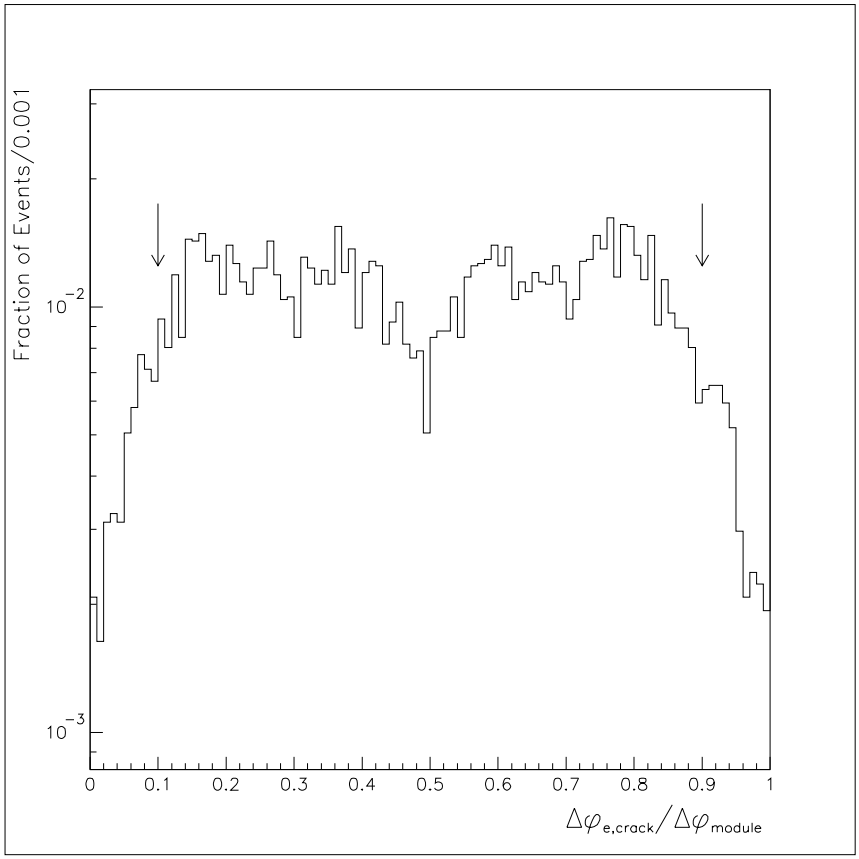

Figure 5.1: Distance from EM cluster to nearest detector crack. Events with $10\% \leq \frac{\Delta\phi_{e,crack}}{\Delta\phi_{module}} \leq 90\%$ were cut from the Z sample. The fraction in the y-scale merely indicates binning.

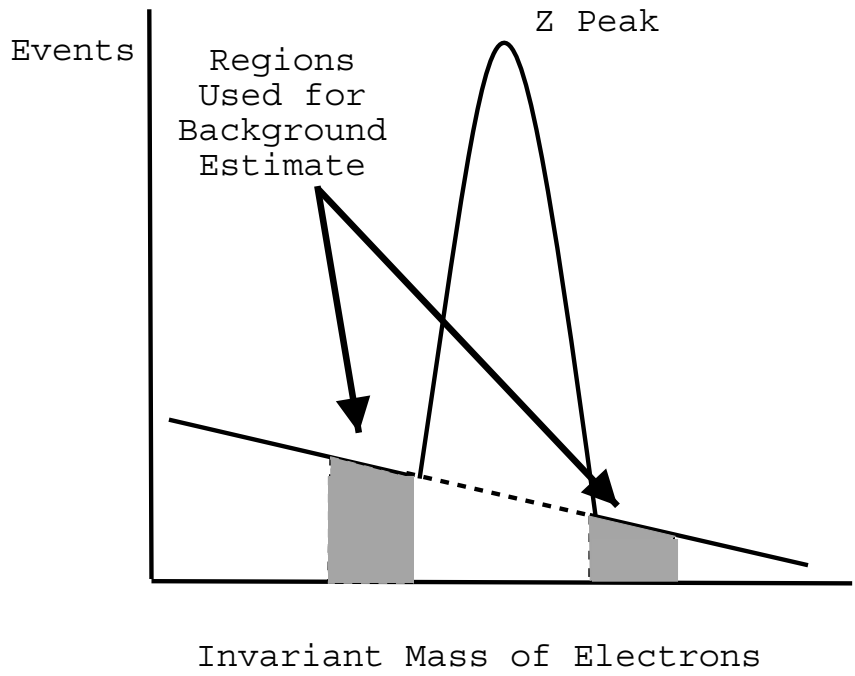

Figure 5.2: Artist's conception of the Z boson mass peak with backgrounds. To calculate the backgrounds to the Z->ee signal one merely needs to count the number of events in the shaded areas.

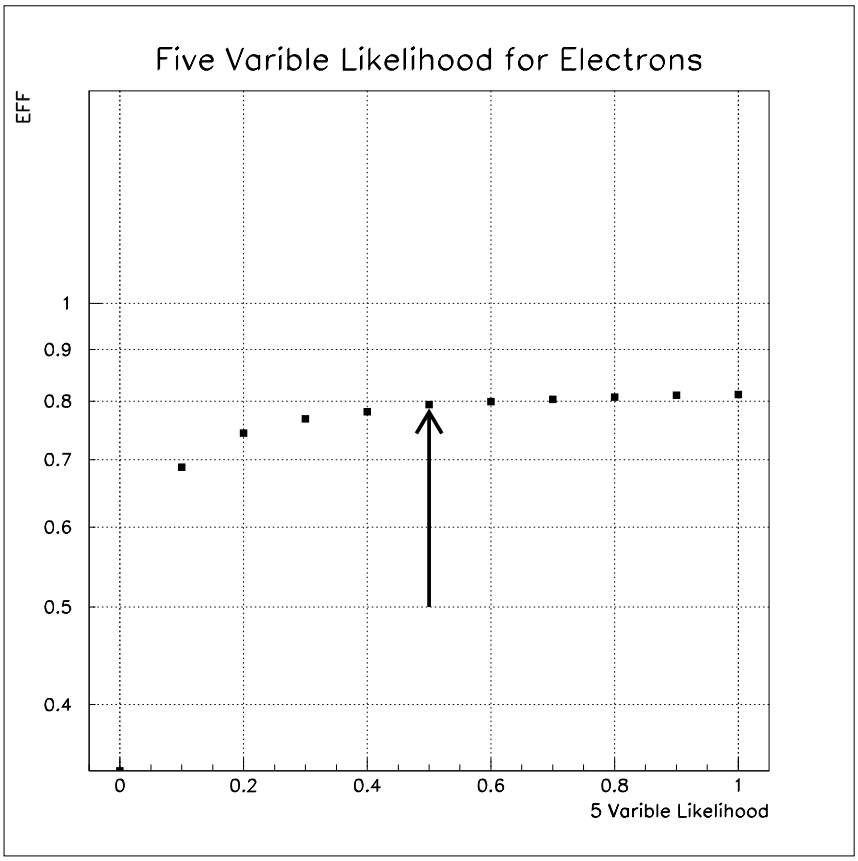

Figure 5.3: The efficiency for an electron to have a given five variable electron likelihood (5vl).

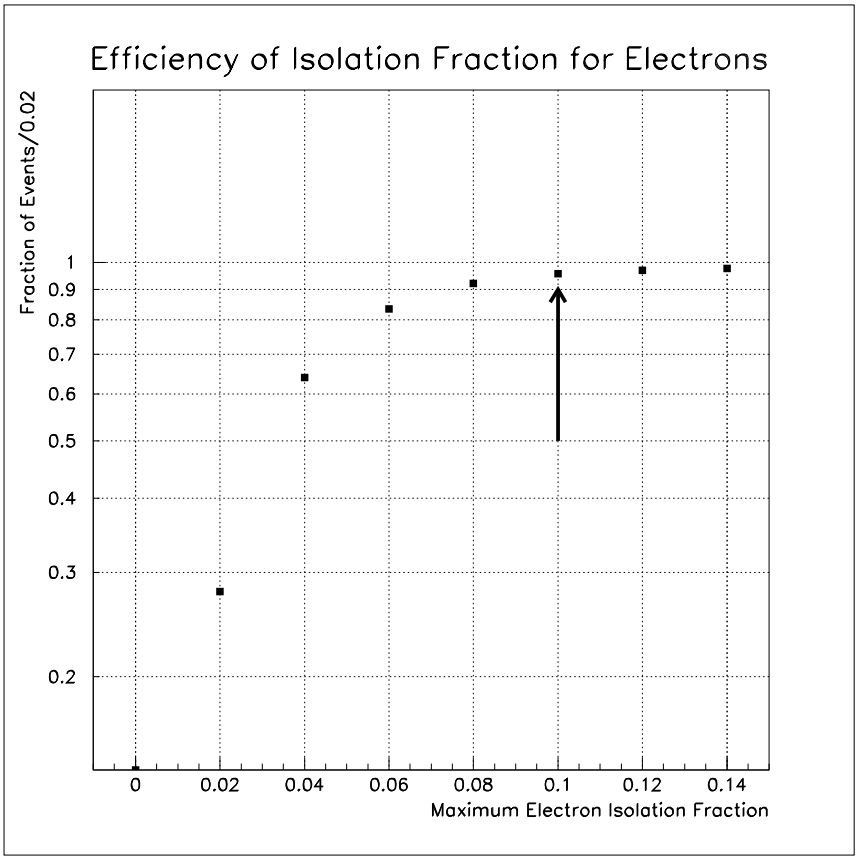

Figure 5.4: Electron isolation fraction efficiency.

Number of Jets	N_1	N_2	Id Efficiency (%)
1 or More	141	131	65.0±2.4
2 or More	21	14	57.1±7.1

Table 5.2: Electron efficiencies for Z samples with at least 1 or 2 jets.

one central and one forward are designated CC-EC. These two samples are used to calculate the electron identification efficiency for the DØ detector, trigger and software. This efficiency, ϵ_{id}, is determined via the relationship:

$$\epsilon_{id} = \frac{2(N_2)}{2(N_2) + (N_1)} \tag{5.1}$$

where N_1 and N_2 are the number of events that contain one or two electrons that pass the identification requirements respectively. Simply put this is the ratio of events where both electrons were identified over the total number of events containing at least a single electron. This technique gives the electron identification efficiencies found in table 5.2. Noted are the efficiencies if there are 1, 2 or more jets in the event besides the electron "jets".

Cuts are now made on the Z and W samples so that they have jets whose E_T is greater than 25 GeV, have EM fraction between 0.1 and 0.95 and CH fraction less that 40% (to remove Main Ring activity since these samples lack the MICRO_BLANK and MRBS_LOSS trigger cuts that would remove MR noise). The cuts are applied to Monte Carlo and the Z + jets(s) cross section is calculated via the relationship that:

$$\sigma x BR = \frac{\frac{N_{CC-CC}}{(\epsilon_{id}^{CC})+2\epsilon_{id}^{CC}(\epsilon_{L2}^{CC}-\epsilon_{id}^{CC})} + \frac{N_{CC-EC}}{\epsilon_{id}^{CC}\epsilon_{L2}^{EC}}}{Acceptance \cdot \mathcal{L}} \tag{5.2}$$

where $\mathcal{L}$ is the luminosity, the Acceptance refers to the acceptance in Monte Carlo, ϵ_{L2}^{CC} and ϵ_{L2}^{EC} refer to the measured Level 2 electron efficiencies in the CC and EC, (98.3±0.2)% and (99.3±0.2)%, respectively. ϵ_{id}^{CC} is the electron

Number of Jets	N_{CC-CC}	N_{CC-EC}	Accpt. (%)	σXBR (pb)
1+	259	114	3.06±0.08±0.11	140±10±9
2+	33	14	1.85±0.07±0.13	32.0±6.1±2.5

Table 5.3: Cross sections of the Z + Jets background at the DØ detector.

identification efficiency in the CC and N_{CC-CC} and N_{CC-EC} are the number of events with 1 and 2 CC electrons. The measured luminosity of (111.9±4.8)pb^{-1} gives the Z cross sections as shown in table 5.3. To ensure that the Monte Carlo indeed models Z events well the Z+2 jets sample is compared with the Z data. These comparison plots are shown in figure 5.5, see caption for variable details.

5.1.3 W + Jets Cross Section

Using 84.5±3.6 pb^{-1} of data acquired via the EM1_EISTRKCC_MS trigger the W + jets cross section can be calculated. W events are required to pass MRBS_LOSS and MICRO_BLANK trigger conditions as well as having greater than -10 GeV of energy in the CH region of the detector. All of these conditions help to reduce main ring contamination of the sample. The event is required to have $\not\!\!E_T$ greater than 25 GeV and the EM object in the event must meet the EM cuts outlined for the Zs.

Background is present in this set mostly of the form of multijet (QCD) events. In order for non-W events to have passed one of the hadronic jets would have had to been mistaken for an electron and energy mismeasurement simulates the $\not\!\!E_T$. To measure the amount of background present in the sample the electron cuts are reversed so as to pick out events that are probably not electrons. These "anti-electron" cuts require that the 5vl, ϵ_5 be greater than 5 and the isolation fraction, f_{iso} be more than 10%. This constructed QCD sample is then normalized to the W sample using the low $\not\!\!E_T$ (less than 15

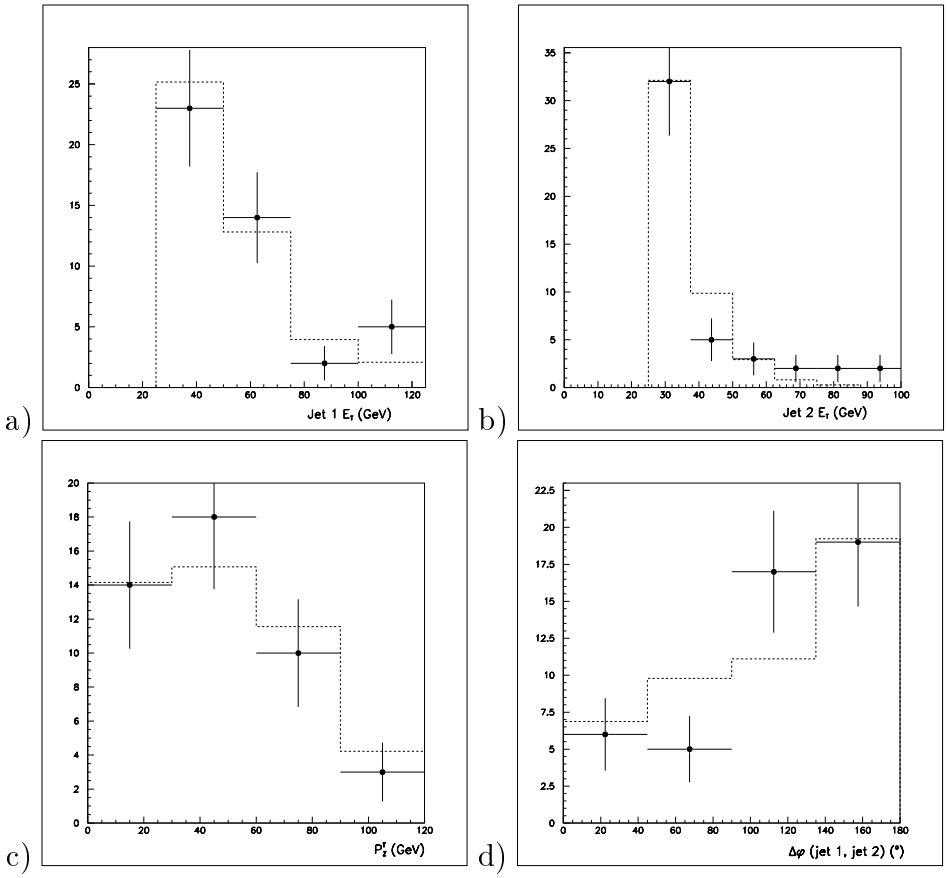

Figure 5.5: Z + 2 jets Monte Carlo (dashed) compared to EM trigger data (points). Starting from the upper left and going clockwise the plots are a) leading jet, b) second jet, c) the p_T of the Z d) angle between the first and second jets.

Number of Jets	Events	Accpt. (%)	σXBR (pb)
1+	2986	7.20±0.12±0.29	755±34±44
2+	381	2.44±0.09±0.14	324±45±23

Table 5.4: Cross sections of the W + Jets background at the DØ detector.

GeV) events from the EM1_ELE_MON single electron trigger. From this the ratio of QCD events passing the electron cuts to those passing anti-electron cuts. In the W + 1 Jet sample, 3284 events, 298 are predicted to be due to QCD background. In the W + 2 Jet sample, 469 events, 66 are predicted to be QCD.

HERWIG (a particle generator) and the DØ measured cross sections for top production is used to predict the number of background events in the W sample due to top-> W+b decays. 22 events in the W + 2 Jets sample are predicted to come from top production and decay.

The W + jet(s) cross section is given in table 5.4. The Monte Carlo was again compared to data, as shown in figure 5.6.

The cross sections calculated here will allow for the prediction of vector boson survivors left in the JET_2_MISS data set after a given cut criteria is constructed.

5.2 Top Background

Top quark production can create a significant background to the Jets + $\not\!\!E_T$ signal. If produced in pairs the top and anti-top quarks can decay to leptons and jets. If the leptons are lost or mis-identified as jets the event can pass all the analysis physics cuts. The physics Monte Carlo generator HERWIG 5.7 was used to produce 29,557 $t\bar{t}$ pairs which were passed through GEANT 3.15 (a particle detector simulator) and CAFIX 5.1 (the DØ energy correction).

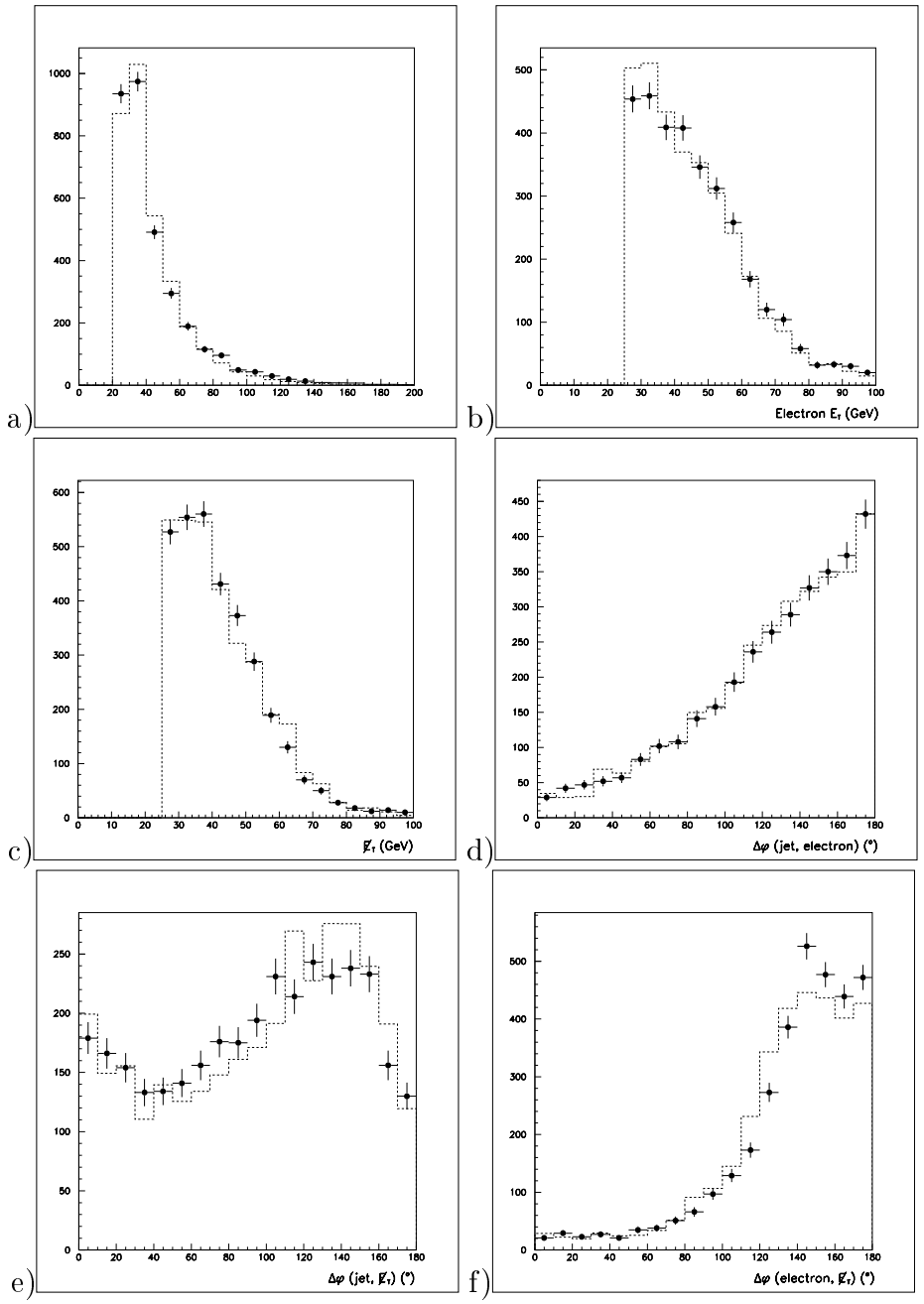

Figure 5.6: W + 1 jet Monte Carlo (dashed) compared to data (points). a) Jet E_T , b) E_T of the electron, c) $\not\!\!E_T$ distribution, d)angle between the jet and the electron, e) angle between $\not\!\!E_T$ and the jet f) angle between electron and $\not\!\!E_T$.

The selection cuts, trigger efficiencies and top cross sections are applied to the sample to determine the top quark's contribution to the background.

5.3 Multi-jet Background

Probably the most difficult background to predict in the jets + $\not\!\!E_T$ signal set are events that pass the physics cuts but are simply due to detector mismeasurements of common multi-jet events, often referred to as the QCD background. Many of the physics cuts used in the present analysis (and the trigger) are designed to reduce the number of multi-jet events passing into the surviving data set. The angular cuts, the high jet E_T cuts and the high $\not\!\!E_T$ cut all help to eliminate the QCD background. However, the large luminosity of the Run 1b/1c datasets and the long tails of the QCD distributions ensure that almost no set of cuts can retain any signal and eliminate all QCD background.

To predict the QCD contamination in the surviving JET_2_MISS data set two different techniques were used and then combined to obtain the results in table 5.12.

5.3.1 QCD Predicted by the JET_30 Trigger

To remove the JET_2_MISS trigger bias from any prediction of QCD contamination a trigger with significantly looser cuts was taken as a baseline set. The first trigger used in this analysis was the JET_30 trigger. JET_30 is a very loose trigger requiring only a large deposition of energy in a quadrant of the detector[2] . The large bandwidth required for a trigger of this nature made it necessary to *pre-scale* the sample. Pre-scaling a trigger merely indicates that a known percentage of the events are discarded without bias. The JET_30

[2]See table 3.2 for a comparison of jet triggers

trigger is heavily pre-scaled so that a very small integrated luminosity of events are available on tape for analysis. The full sample of JET_30 trigger events ($0.23pb^{-1}$) was examined for the behavior of the $\not\!\!E_T$ as our physics and detector cuts were applied.

Very light physics cuts were used to determine a mathematical fit to the $\not\!\!E_T$ distribution, allowing for large statistics to guide our choice of function. The function chosen needed to model the $\not\!\!E_T$ over a large range of values. This was to insure a good fit to the most important portion of the distribution, the tail of the function. The function used is a three (3) parameter function given by

$$f(x) = \exp(p1 - p2 * \sqrt{x} - \frac{p3}{(x+1)}) \tag{5.3}$$

The function fit to the JET_30 data for various tightness of cuts are shown in fig 5.7. To determine the number of events that may contaminate the JET_2_MISS sample, we extrapolated the curve out to our $\not\!\!E_T$ cut point and integrate the curve out to infinity. Since the JET_30 sample comprises only 1/800th of the integrated luminosity of the JET_2_MISS (mostly due to heavy pre-scaling of the trigger) it is reasonable to question both the validity of this method and to demand a cross check with a secondary method (see the section 5.3.2 for that discussion).

To estimate the errors on this method, we utilized the errors reported from the MINOS error generator reported via the MINUIT package in PAW[3]. See table 5.5 for the errors reported by Paw/MINUIT

The errors on the fit parameters can give one pause since the function

[3]PAW is the Physics Analysis Workstation software written by the CERN physics collaboration. See reference [17] for details.

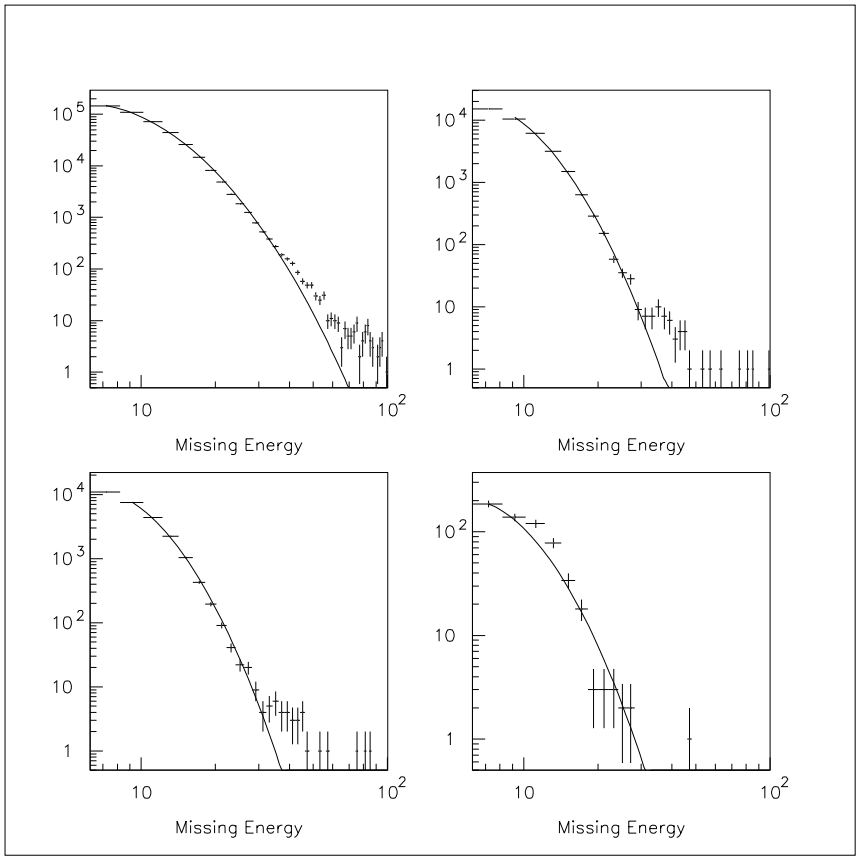

Figure 5.7: Functional fits to the $\not\!\!E_T$ remaining in the JET_30 data. The bottom right plot shows the remaining events after all physics cuts save the $\not\!\!E_T$ cut has been made.

Parameter	Nominal Value	MINUIT Estimated Error
P1	13.47	1.38
P2	2.254	0.304
P3	18.79	4.26

Table 5.5: Reported fit parameters from PAW for QCD $\not\!\!E_T$ distribution.

Technique for QCD estimation	Expected QCD
Leptoquark Search DØ Note 3769	162.1 ± 23.7
Using the Technique JET_30 Technique	149.7 ±69.3

Table 5.6: Estimates of the QCD contamination of the 30-40 GeV bin in the JET_2_MISS sample with cuts outlined in [18].

has an exponential form. To estimate the variance and standard deviation of the QCD background within this fit model the total number of events was predicted by using a simple Monte Carlo method and the parameters were varied within their errors. A simple normal probability across the errors was used to determine the variance on the number of total QCD events contaminating the sample. Shown in figure 5.8 is the distribution of the predicted events in the JET_2_MISS sample extrapolated from JET_30 given the errors on the functional fit. The nominal QCD multi-jet contamination expected in the JET_2_MISS trigger is given in table 5.12.

This technique was Compared to one utilized in a similar experiment carried out at DØ . Reference [18] outlines a technique for using the 30 to 40 GeV bin in the $\not\!\!E_T$ distribution with lighter cuts. The results of this comparison are outlined in table 5.6.

5.3.2 QCD Predicted by the JET_3_MON Trigger

Due to the relatively small luminosity of JET_30 sample available it seems prudent to estimate the QCD contamination of the sample using a method arising from a different trigger sample.

In order to obtain the trigger turn on curves for the $\not\!\!E_T$ trigger term, a set of events with constructed $\not\!\!E_T$ was created. This set was created using events passing the JET_3_MON trigger criteria which contained at least 3

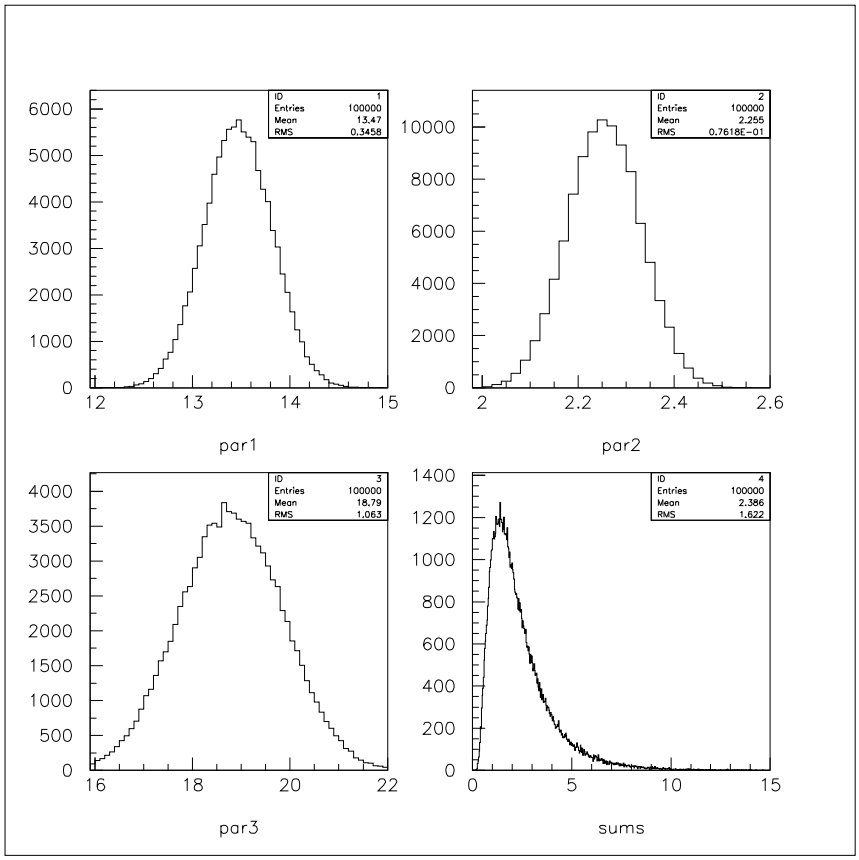

Figure 5.8: Parameters generated by MINUIT for fitting the JET_30 sample (shown with smeared errors). The bottom right plot shows the total number of events predicted by the JET_30 sample with smeared parameter errors taken into account for 100000 random choices of errors.

jets with E_T of at least 20 GeV. To create the $\not\!\!E_T$, one jet was removed from the each event by replacing the jet cells with calorimeter noise taken from non-jet cells in the event and then passing the events back through the RECO software. Three (3) sets of events were created by systematically removing the leading jet, then the second jet and finally the third jet. In this manner a large set of 2 jet events with artificial $\not\!\!E_T$ was created. This set also represents a class of events where one major jet has escaped detection and would not be removed via angular cuts. This would seem to be a good set to use to predict multi-jet background that would contaminate the JET_2_MISS sample.

Since the set was created from events whose only criteria was the existence of 3 large E_T jets, the event distributions do not mirror any relation to real event likelihoods in the detector. To correct this, each event in the set was weighted via the jet distributions to the JET_30 sample (without cuts). Thus a functionality was placed on the distribution of the leading and second jet. This creates a more realistic distribution for the $\not\!\!E_T$, the parameter of choice, see figure 5.9.

To normalize the set to the JET_2_MISS sample the jets were weighted according to a real physics distribution. The events with $\not\!\!E_T$ in the range of 30 to 40 GeV were normalized to the same bin in the JET_2_MISS sample (minus VB and Top backgrounds predicted using the Monte Carlo samples). This predicted value was compared to the value that would have been obtained had only the leading jet been removed in order to give an estimate on the error of this method.

The results of these two techniques are consistent within errors and were combined to get the expected QCD multi-jet contamination in the JET_2_MISS data, for these results, see table 5.12.

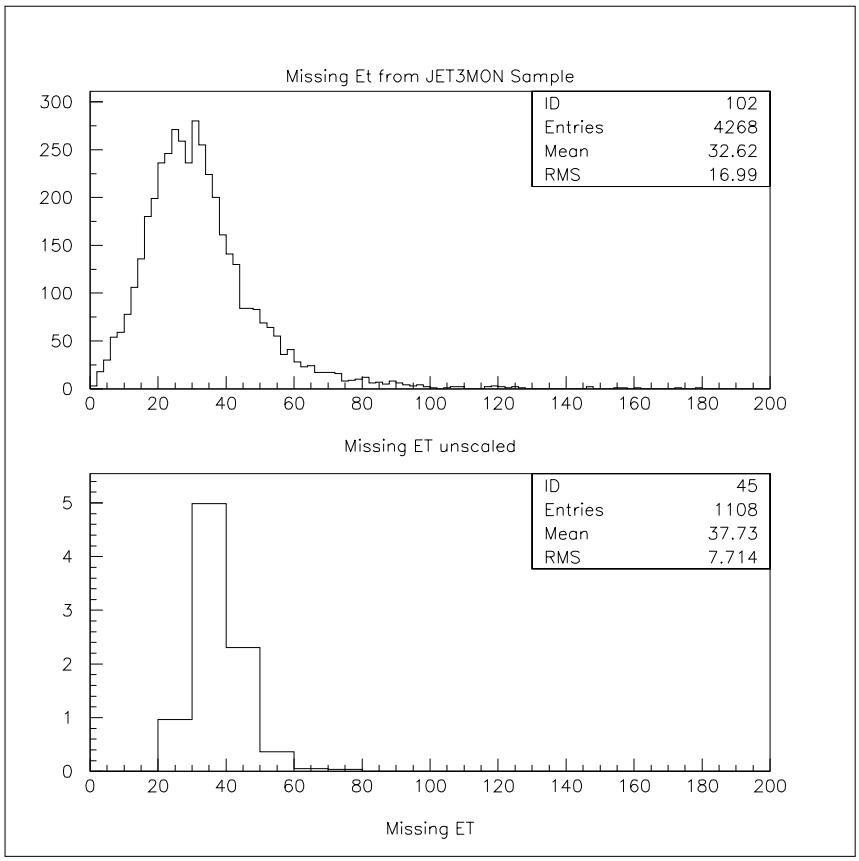

Figure 5.9: The constructed missing energy curves from the JET_3_MON sample a) without scaling, b) with jet scaling, trigger turn-ons and JET_2_MISS normalization.

Cut Condition	Surviving Events
JET_2_MISS Trigger	503,557
Removed Bad Runs & Main Ring Cut	487,715
Leading Jet $E_T > 50$ GeV	207,854
Second Jet $E_T > 50$ GeV	106,728
$\not\!\!E_T > 40$ GeV	13,825
Vertex Confimation	5918
Lepton Rejection	3227
$30 < \lvert\Delta\phi(\text{Jet}, \not\!\!E_T)\rvert < 160$	219

Table 5.7: Initial Criteria and the reduction of overall trigger set in the JET_2_MISS sample.

Once the background samples and prediction techniques are in place and well understood the analysis can take place. This chapter outlines the data analysis and final results.

5.4 Initial Cuts

To insure the integrity of the data and our ability to predict the background initial cuts were made on the data and compared to the background predicted. A breakdown of the number of surviving events from each additional cut to the data is made in table 5.7. The number of background events were predicted using the techniques outlined in the previous chapter. The distribution of the predicted background and the surviving data events was then constructed to ensure good agreement prior to final cuts being applied.

With a total of 219 candidate events surviving the initial cuts the vector boson and top Monte Carlo was subjected to the same cut criteria and plotted with respect to the surviving data events. This plot shows that the tails of the physics distributions are very consistent with the data but the lower portions of the distributions are not. This large excess of events is evidence

Sample	Survivors
VB and Top MC	158.3±27.9
QCD Predicted Using JET_30	80.3±44.58
Total Background	235.7±47.1

Table 5.8: The total number of events from background samples predicted in the JET_2_MISS sample using the initial cuts. 219 events actually survived the cuts, compatible with the project number.

of a type of event not accounted for in the sample, either signal or a major background. Using the technique outlined in section 5.3 the background arising from multijet mismeasurement can be estimated. Using those techniques gives a QCD prediction of 80.3±44.6 events, see table . The QCD mismeasurement accounts for the data excess. The large errors on the QCD estimate makes the reduction of QCD events into the sample a priority.

5.5 Removal of ICR Jets

The DØ detector is not a perfectly hermetic detector. Engineering the massive construct makes complete isotropic 4π coverage impossible. It is reasonable to conclude that there may be a portion of the detector that does not respond with the same accuracy the rest of the detector enjoys. The portion of the detector that often receives attention is the Inner Cryostat Region (ICR), the portion of the detector where the central cryostat meets with the end cap cryostats. This region is instrumented to the best of the physicists ability with the ICD and Massless gap detectors, but its response can induce mismeasured jets. Examining the Jet_30 trigger sample (a trigger not biased for or against events having $\not\!\!E_T$) for events containing any $\not\!\!E_T$ it is easy to see that when jets are located in the ICR the event carries with it $\not\!\!E_T$, see figure 5.11. As this analysis is sensitive to these mismeasurements, this region was studied for

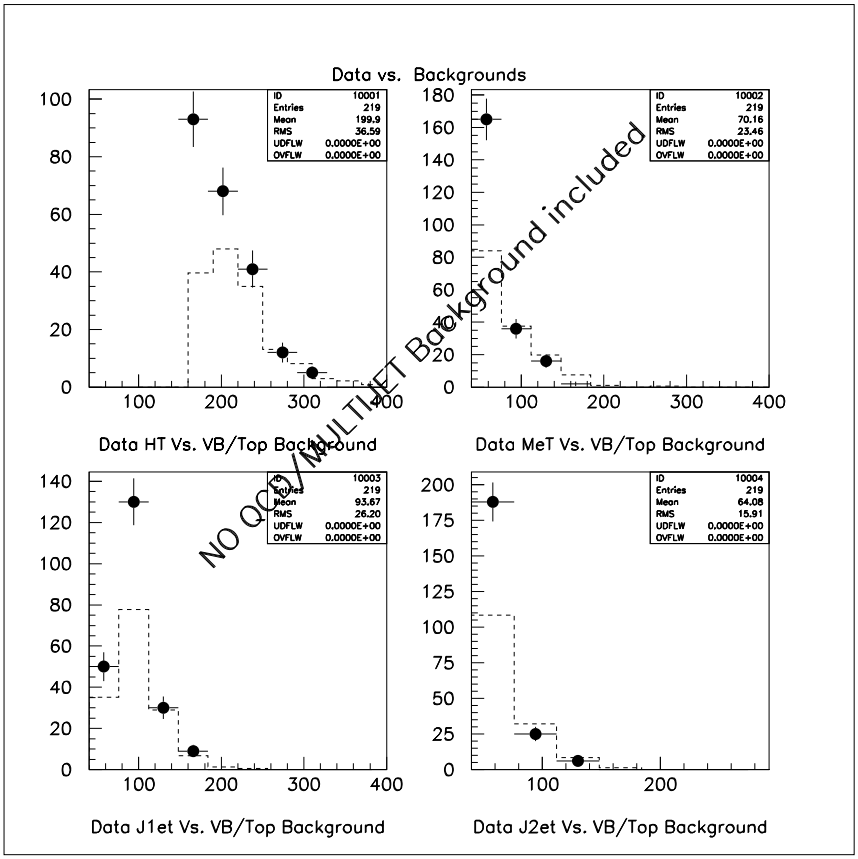

Figure 5.10: Data (points) vs. Background (bars) surviving the loose cuts outlined in table 5.7. No QCD Multijet background has been added to the overall background.

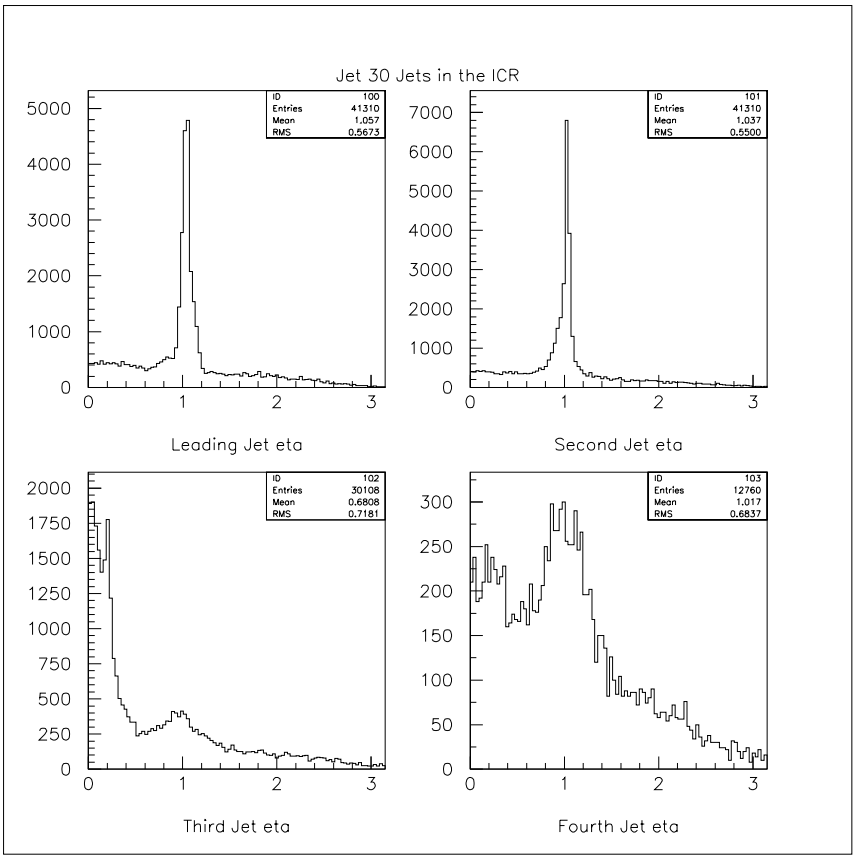

Figure 5.11: The detector η of jet_30 jets. The only requirement on this set is that the event has 25 GeV of $\not\!\!E_T$. The large bulges in the jet detector η plots shows a large bias for $\not\!\!E_T$ when jets are in the ICR.

removal.

The removal of events having any reconstructed events in the ICR carries with it the weight of having an adverse impact on acceptances of signal events. The cuts were also deemed necessary since there sometime appeared events that had extremely large (20+ GeV) amount of energy deposited in the massless gap detectors. The veracity of such a measurement could not be determined.

Cuts on the the size of the ICR were investigated iterating the ICR in sizes of 0.1 units of η. Although QCD events could be statistically eliminated from the sample by cutting any event having jet η in a range of $.8 \leq |\eta_{detector}| \leq 1.5$, stop signal Monte Carlo was too heavily reduced by such cuts as to warrant a softer cut of $.8 \leq |\eta_{detector}| \leq 1.2$, as figure 5.11 would indicate as appropriate.

Since Monte Carlo models jet location well, a special study to determine the background reduction of SM background was determined to be unnecessary as the same cut would be applied to the Monte Carlo during SM background prediction, thus removing their acceptance.

5.6 Signal Monte Carlo

To understand the effects that physics cuts have on a signal a large number of simulated signal events need to be generated. These generated events are then subjected to the same cuts as the dataset to determine the acceptance of the signal. Stop events were generated by using the simulation software package ISAJET (version 7.13) with its implementation of ISASUSY. The generated stop events were then passed through a simulation of the DØ

trigger (VMS_FILTER). To construct the jets created by the partons within the event the library of jets SHOWERLIB was used (as it was in the construction of the VB backgrounds). The events were then passed through DØ GEANT and reconstructed by DØRECO (version 11.19). These event samples were checked against samples made by earlier versions of ISAJET (version 7.0) and various versions of DØRECO (versions 10.12, 10.13 and 11.19) to insure that there was no dependence on the software versions. A sample data distribution is show in figure 5.12. These events show strong leading and secondary jets as well as a wide distribution of $\not\!\!E_T$ ranges.

The theoretical cross sections for stop production only depend on the mass of the stop squark, not on the mass of the LSP. The cross sections for stop production from ISASUSY are shown in figure 5.13. The leading order cross section calculation shows a kink at about 95 GeV. The next-to-leading order (NLO) calculation is smooth along the entire Stop mass. The NLO cross section is used to calculate our limit.

5.7 Final Cuts

To produce a limit that has searched the largest available phase space the final physics cuts must balance acceptance of signal versus rejection of background. The inability to produce the QCD backgrounds in way that is independent from trigger data greatly inhibits use of automated optimization tools such as neural net algorithms. To optimize the cuts to allow for good signal acceptance and reducing backgrounds an iterative method was employed to examine signal and background acceptances over varying cuts sets with preferences set toward cut sets that limited hard to model QCD.

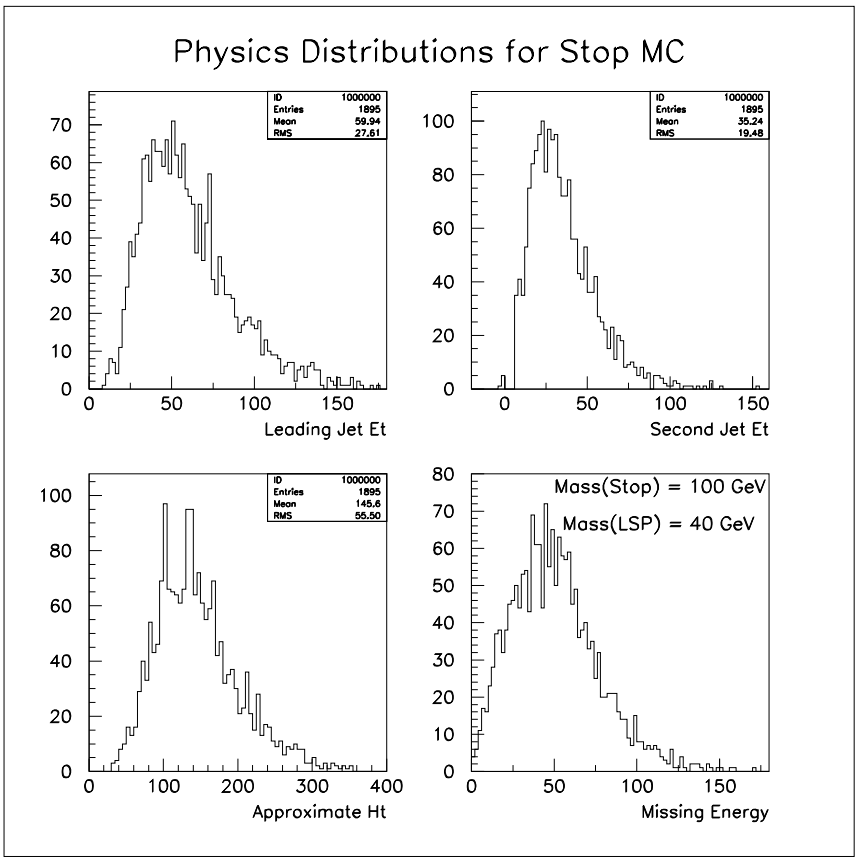

Figure 5.12: Distribution of leading jet, second jet, Ht and missing energy physics parameters for a typical stop sample set. Here Ht is defined by the sum of the E_T for the first two jets and the $\not\!\!E_T$. The only criteria made on this set was that it contain two reconstructed jets.

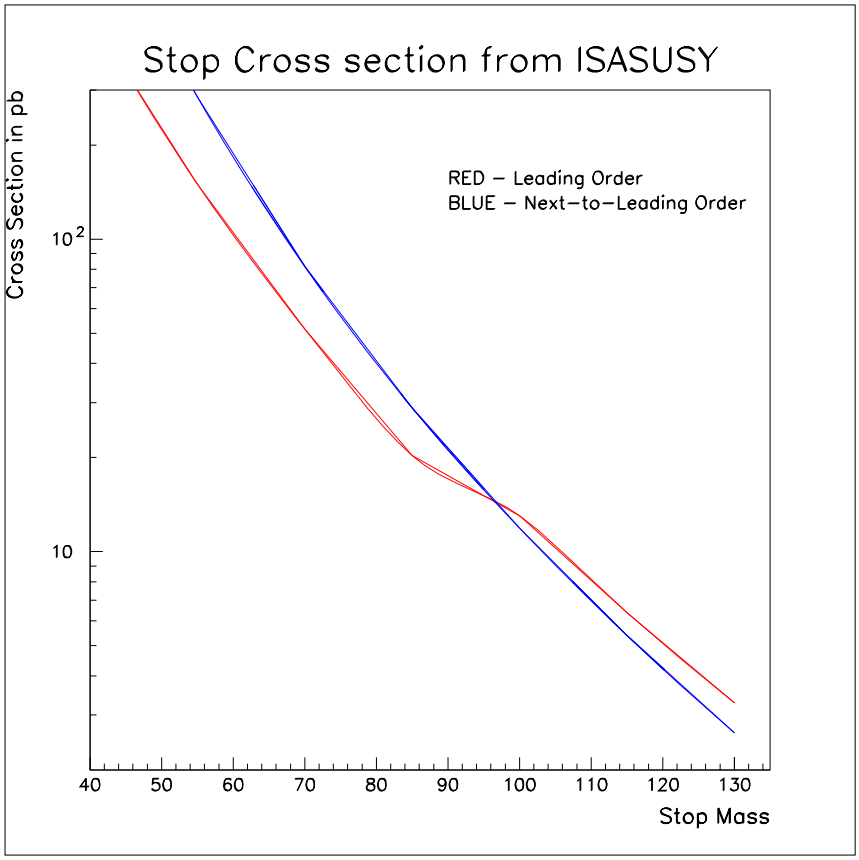

Figure 5.13: The theoretical cross section for stop squark production.

The set of cuts examined for optimization was limited to leading jet E_T , second jet E_T , $\not\!\!E_T$, the sum of all the jets E_T and $\not\!\!E_T$ in the event (often called H_t).

$\not\!\!E_T$ was of crucial importance to the sensitivity of the search and was limited to values allowing for maximal phase space coverage. A value of 35 GeV on $\not\!\!E_T$ would have been preferable, however in order to construct the QCD background from JET_3_MON the cut was increased to 40 GeV. $\not\!\!E_T$ cuts varying by 5 GeV intervals were investigated up to a value of 75 GeV. A final $\not\!\!E_T$ cut of 40 GeV was chosen.

Jet cuts were investigated in increments of 5 GeV. The motivation for higher jets cuts was to reduce the influx of QCD mismeasured jets as well as to optimize against W$\rightarrow\tau$ events which came in as the dominant background. Asymmetric jet cuts were chosen to help optimize stop acceptance. Events with a leading jet having less than 100 GeV E_T were cut as were events with second jets having less than 60 GeV of E_T .

The very large jet and moderately large $\not\!\!E_T$ cuts made cutting on H_t unnecessary. H_t cuts were designed to be heavily biased against QCD events, a background handled well by the large jet E_T cuts.

After the final cuts were selected, the stop acceptance was plotted for several mass points in stop. This plot is shown in figure 5.14. The x axis in this plot represents differing stop/LSP mass points and are labeled using the convention $M_{stop}\_M_{LSP}$.

The final selection cuts are outlined in table 5.13, the predicted QCD contamination of this set is located in table 5.12 and a plot showing the data events versus predicted VB background is shown in figure 5.15.

The acceptance of top events as well as a nominal number expected

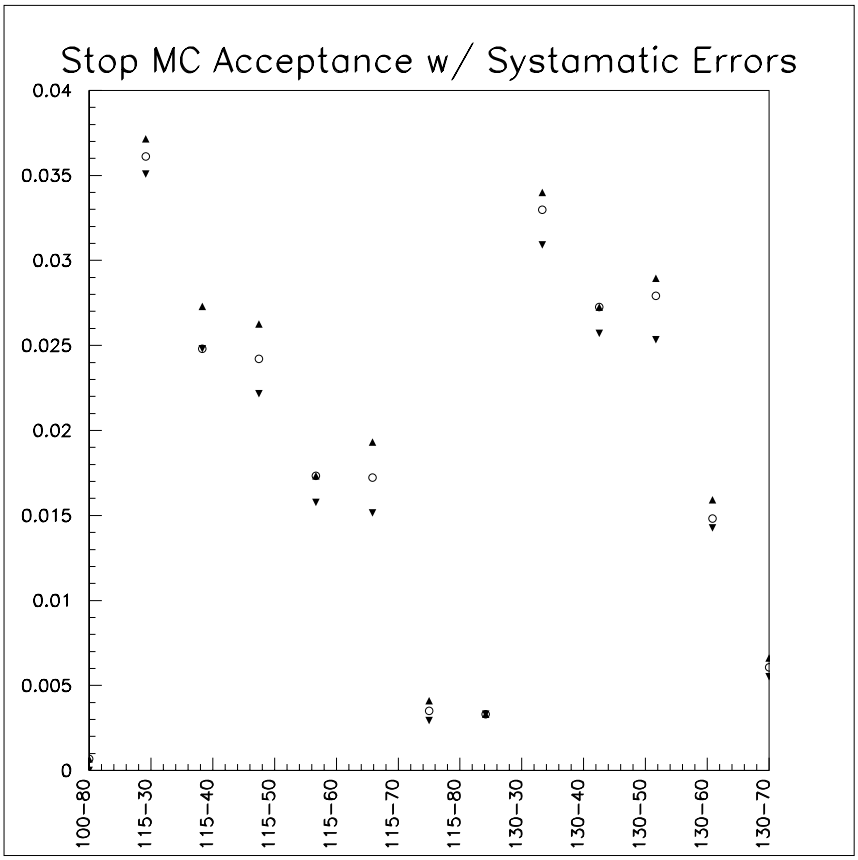

Figure 5.14: Acceptance of Monte Carlo Stop signals for the cuts in table 5.13 and the systematic error associated with the energy scale. The x axis is labeled by Stop mass-LSP mass. (Note that points between labled points on the x axis are incremented by 5 GeV in LSP mass.)

Vector Boson Background	Acceptance $\times 10^{-5}$	x$\sigma BR(pb)$
$W \to \tau + \nu + 1jet$	2.82±.009± $^{0.14}_{0.025}$	755±34±44
$W \to \mu + \nu + 2Jets$	2.30±0.013± $^{0.50}_{0.49}$	324±45±23
$W \to \tau + \nu + 2Jets$	13.4±0.076± $^{0.63}_{2.4}$	324±45±23
$Z \to 2\nu + 2jets$	19.1±0.0996± $^{0.62}_{2.4}$	192±37±15
$Z \to 2\tau + 1jet$	0.82±.0026± $^{.038}_{.014}$	140±10±8
$Z \to \mu\mu + 2jets$	8.43±.044± $^{0.32}_{0.21}$	32.0±6.1±2.5
Nominal Total		9.58

Table 5.10: VB backgrounds remaining in JET_2_MISS sample after applying the cuts in table 5.13.

Background & cuts	Acceptance x 10^{-3}	$\sigma \times BR$ (pb)	Nominal # predicted
$t\bar{t} \rightarrow l + jets$	$4.29 \pm .023 \pm \begin{matrix} .070 \\ .0026 \end{matrix}$	$2.1 \pm 0.4 \pm 0.4$	0.77

Table 5.11: Number of events from top pair production using the cuts in table 5.13.

to survive the cuts are given in table 5.11.

The background predictions show that the data is consistent with no new physics. However, the results can be used to set a limit on just what masses of stop and LSP can be excluded from further searches.

5.8 Setting Limits – Bayes' Theorem [15]

When searching for a new particle often a null result is reached. In these cases it becomes the job of the physicist to make a statement as to what he has not found. The technique employed to report the amount of phase space searched by this analysis is given as a 95% confidence exclusion curve. The construction of this curve requires the use of Bayes' Theorem (also called the Principle of Inverse Probability)[4].

When predicting the number of events expected in data, μ, it is easy

[4]The notation used in this discussion is as follows: For a given (discrete) outcome A, we define P(A|B) to be the probability of A given that situation B is true. For a continuous parameter x, we define the *probability density,* P(x|B)dx, as the probability of getting a result X between x and x+dx, given B.

Multi-jet Sample	Number of events expected in the JET2MISS Sample
JET30 Sample	2.4 ± 1.6
JET3MON	2.7 ± 0.5
Total Expected QCD	$2.67 \pm .47$

Table 5.12: QCD multi-jet contamination predicted using the two different techniques. The combination of these results is via the technique outlined in reference [19, Page 21ff].

Physics Parameter	Requirement	Mean Background
Leading Jet E_T	>100.0 GeV	
Second Jet E_T	>60.0 GeV	
$\not\!\!E_T$	>40.0 GeV	
Angle between ANY jet and $\not\!\!E_T$	>30 Degrees	
Eta of Leading jet	<0.8	
Eta of ANY JET	NOT (.8<|eta|<1.2)	
J2MISS EVENTS surviving Cuts	12	12.81 ± 1.77

Table 5.13: Final physics cuts for stop analysis

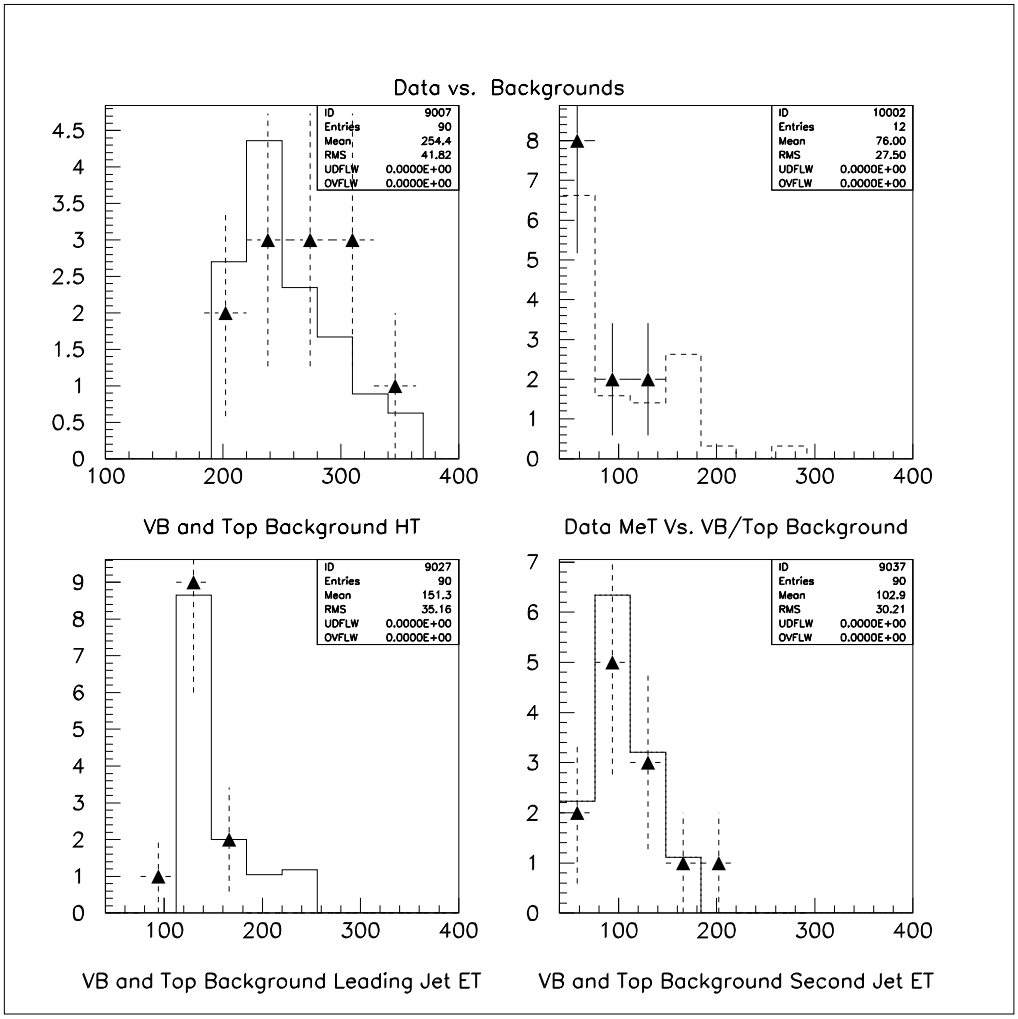

Figure 5.15: Comparison of data remaining after optimized cuts versus background predicted in the JET_2_MISS sample.

to see that

$$\mu = b + \mathcal{L}\epsilon\sigma \tag{5.4}$$

where b is the expected background and $\mathcal{L}$ is the luminosity, ϵ is the acceptance of any cuts on the data and σ is the cross section of the process in question. In the present analysis, b is replaced with a set of backgrounds from the vector boson backgrounds and the QCD enumerated backgrounds. In a counting experiment such as this analysis, the accepted likelihood function for the data is a Poisson distribution with a mean value (μ) such that the probability of observing k events, given a mean μ is:

$$P(k|\mu, I) = \frac{e^{-\mu}\mu^k}{k!} \tag{5.5}$$

where I merely indicates all the information used to build μ and depends on selection criteria. Using equations 5.4 and 5.5 it is easy to see that likelihood function of observing k events, given σ, $\mathcal{L}$, ϵ, and b is:

$$P(k|\sigma, \mathcal{L}, \epsilon, b, I) = \frac{e^{-(b+\mathcal{L}\epsilon\sigma)}(b + \mathcal{L}\epsilon\sigma)^k}{k!} \tag{5.6}$$

The trouble with 5.6 is that the parameter of interest is σ, not the probability of k. To extract the cross section of the process from the above Bayes' Theorem is employed. Bayes' theorem states[19, Page 102ff]:

$$P(H_l|A) = \frac{P(A|H_l)P(H_l)}{\sum_{j=1}^{k} P(A|H_j)P(H_j)} \tag{5.7}$$

Where H_l denotes a set of k systems. Bayes' Theorem gives the probability of having a system H_l if we perform an experiment and get result A. We can

rewrite 5.7 as:

$$P(A|BC) = \frac{P(B|AC)P(A|C)}{P(B|C)} \tag{5.8}$$

where A is the signal cross section between a given σ and dσ, B is the number of events from our experimental data, k, and C is all relevant prior knowledge, including (but not limited to) σ, $\mathcal{L}$, ϵ and all model assumptions giving us the probability:

$$P(\sigma, \mathcal{L}, \epsilon\, b|k, I) = C\frac{e^{-(b+\mathcal{L}\epsilon\sigma)}(b+\mathcal{L}\epsilon\sigma)^k}{k!}P(\sigma|I)P(\sigma, \mathcal{L}, \epsilon\, b|k, I) \tag{5.9}$$

where C is determined by normalizing P, i.e:

$$\int_0^\infty d\sigma \int_0^\infty d\mathcal{L} \int_0^1 d\epsilon \int_0^\infty dbCP(\sigma, \mathcal{L}, \epsilon\, b|k, I) = 1 \tag{5.10}$$

The limit on the cross section determined by the experiment is calculated by integrating 5.9 over the known parameters and their errors.

$$P(\sigma|k, I) = \int_0^\infty d\mathcal{L} \int_0^1 d\epsilon \int_0^\infty dbP(\sigma, \mathcal{L}, \epsilon\, b|k, I) \tag{5.11}$$

In the present analysis the functionality of Bayes' Theorem was performed by Monte Carlo software written by Marc Paterno[20]. This program takes as its inputs the results from table 5.10, table 5.11 and table 5.12 as well as the acceptance of signal in Monte Carlo and the luminosity of the data set and all associated errors.

Chapter 6

Future Stop and SUSY Searches

Often after a null result is arrived at from a search inevitable questions arise as to what to do next. Does the result rule out a model or a theory? How could the search be done better?

In his book *From Eros to Gaia*, Dr. Freeman Dyson stated that there were three avenues or "frontiers" for discovery in science; Precision, Statistics and Energy. Dyson's main thrust of the book was his opposition to the construction of the Super-conducting Super Collider (SSC) in Texas for fear that big science could never separate itself from the murky undercurrents of political gamesmanship. As misguided as that theory may be, his itemization of techniques for discovering new physics was very much right on. To discuss the future of SUSY searches, one can follow the Dyson model and examine each "frontier" individually and determine how progress can be made.

6.1 The Near Future, Improved Statistics

Hadron colliders have the best chance for discovery of new particles due to their wide range of energies searched and very large center of mass energies (compared to those achievable by electron/positron colliders). The Fermilab Tevatron has recently begun taking new data, Run II. Run II at the

Tevatron will only have a marginal increase in its center of mass energy over Run1 (a full 2.0 TeV, rather than the 1.8 TeV of Run I), but will have a vastly improved luminosity. Run IIa is slated to last 2 years and deliver an integrated luminosity of $2fb^{-1}$ with plans for a Run IIb to deliver $13fb^{1}$[22]. These large luminosities will provide the basis for a large number of new SUSY searches powered by the newly upgraded CDF and DØ detectors.

Monte Carlo studies have been done to determine the reach of Run II given different models[23]. Monte Carlo samples were examined with CDF Run1 responses used as a benchmark for reconstruction and efficiency. Several models were examined, but of interest to the present analysis is their prediction to how far Run II can extend the exclusion curve in the stop-mass/LSP space. The limits for stop production, both stop to charms and stop to b quarks and leptons are shown in figure 6.1. Studies have also been done to determine background reduction techniques [24] in Run II and show great promise that Run II can extend the light stop search limits.

6.2 The Next Step, The Energy Frontier

Statistics alone can rarely do what brute force can accomplish. Higher energy hadronic beams and collisions may well prove the best avenue for discovery. Currently CERN is preparing for the next generation of hadronic runs at a facility called the Large Hadronic Collider (LHC). The LHC will feature $p\overline{p}$ collisions at a center of mass energy of 14 TeV. The primary goal of the LHC (and its associated detector experiments) will be to confirm the existence of the Higgs boson and determine the nature of the Higgs sector (thereby completing the standard model) however the LHC also provides physicists with an

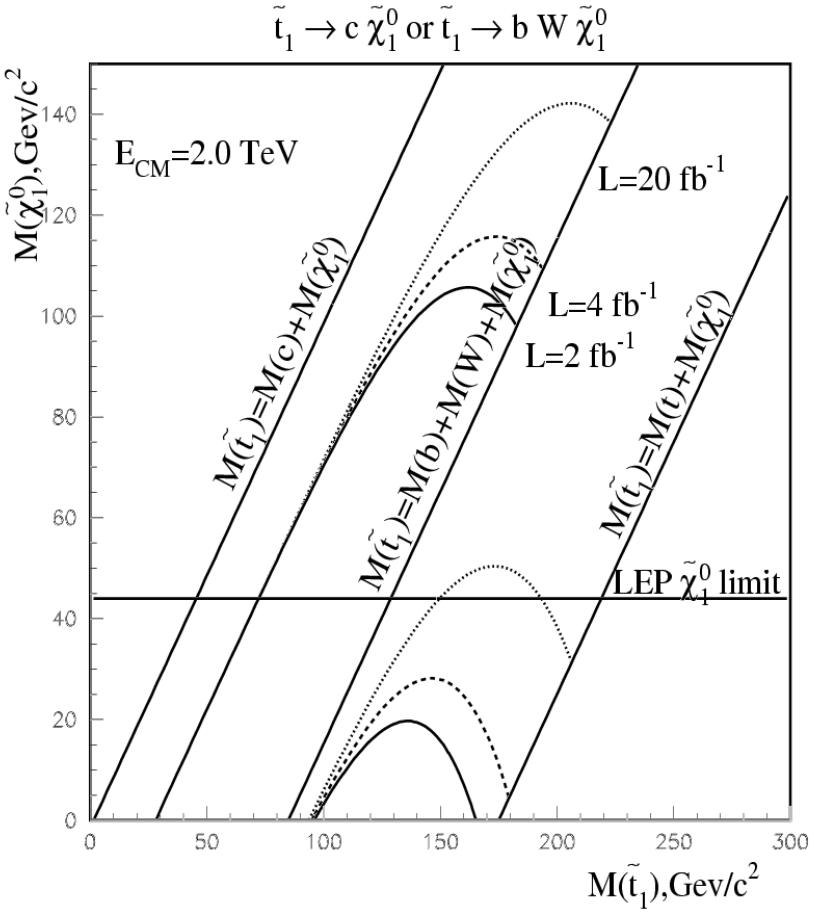

Figure 6.1: Predicted stop limits produced at various integrated luminosities. The solid lines are representative of the luminosity expected from Run IIa. Figure extracted from reference [23].

excellent platform for SUSY discovery.

The main process for superparticle production at the LHC would be from quark-antiquark or gluon-gluon fusion[25]. At low squark/gluino masses the superparticle pair each will decay to a quark and photino/LSP state. (Assuming R-parity conservation the final particles in the decay chain must have a SUSY particle). This would produce the jets and $\not{E}_T$ signature in the detector. This direct decay chain is not the dominant signal at the high LHC mass regions of interest (>100GeV, the Tevatron already limits squark and gluino mass to > 180GeV[26]) and the long cascade chain from the decay of the SUSY particles would wash out the $\not{E}_T$ and jets signal resolution. This loss of primary signal would be compensated by the arise of a plethora of multilepton signals. These multilepton signals would allow for a squark/gluino 5σ discovery mass reach of ~800GeV at "low" luminosity (10fb^{-1}) and up to ~1.2 TeV at "high" luminosity (100fb^{-1})[27]. Regardless of the relative mass of the stop with other squark masses, the LHC should either discover SUSY or rule it out as an answer to the hierarchy problem.

6.3 After discovery, the Precision Frontier

Hadronic colliders provide an excellent platform from which to operate general purpose experiments and searches. The downside of hadronic colliders is the composite nature of the colliding beams. The quarks and gluons within a hadron that take part in a collision all carry some fraction of the hadron's momentum. The amount of the momentum carried by each element of the particle is not known apriori, thus the actual momentum of the colliding particles is not truly known on an event by event basis. Lepton colliders make

a much more precise instrument from which to "tune" experiments to particular resonances and to do precise measurements of particle properties. The next generation of collider construct under consideration by the physics community is the muon collider. The muon collider may provide an excellent test bed from which to study Higgs and SUSY properties.

Without straying too far in the technical challenges that face engineers when asked to accelerate muons, its safe to say that muon colliders would provide a challenge to build, but once constructed would allow for highly tuned physics measurements. Muon colliders would present an improvement in precision over hadron colliders, but also over electron colliders in that a) the much heavier muon does not suffer synchrotron radiative limits on their circular acceleration making a multi-TeV beam feasible, b) muon beam energy would not be smeared out by beamstrahlung radiation[1] , c) the larger Yukawa couplings of muons allow for Higgs production as an "s-channel" resonance make very precise studies of the Higgs possible[28]. This makes possible very precise studies of stop and Higgs couplings.

[1]"Beamstralhung" radiation occurs when high energy electron and positron beams collide head-on. The moving charges within the beams create a magnetic field, when the beams pass through each others magnetic field the beams emit bremsstrahlung radiation.

Chapter 7

Conclusion

This search did not find evidence of light stop production at the DØ detector at Fermilab. Using available predictions of backgrounds and the survival rate of trigger events a limit on the mass of the stop squark for a given LSP mass was set, see figure 7.1.

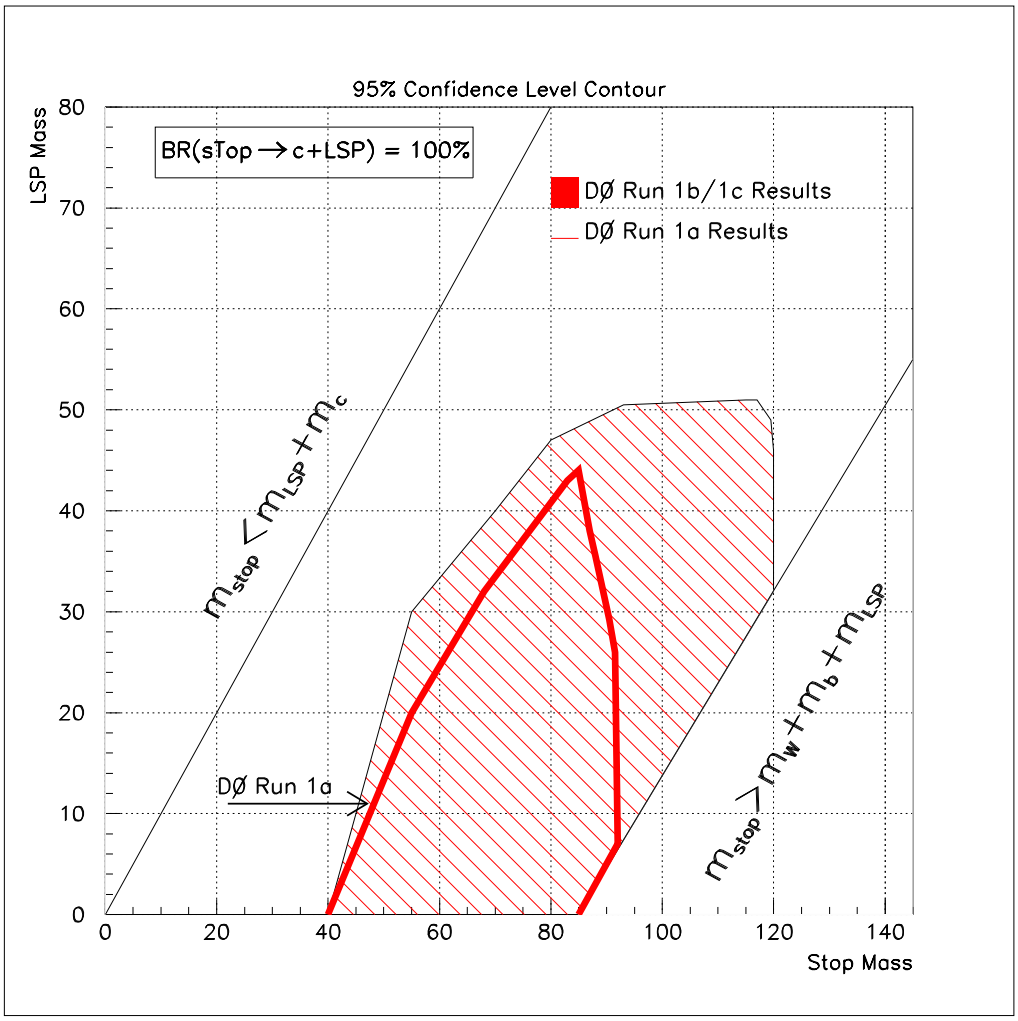

Figure 7.1: The region of Stop/LSP mass space excluded by this analysis is shown as the shaded region. The previous DØ analysis exclusion is shown as the solid line.

Bibliography

[1] J. Thompson, "Introduction to Colliding Beams at Fermilab", Fermilab Technical Memo. TM-1909, October 1994

[2] J. L. Lopez, Rep. Prog. Phys. **59**, 819 (1996)

[3] Particle Data Group, *Phys. Rev.* **D 54**, 1996 1.

[4] P. Smith *et. al.*, *Nucl. Phys.* **B144** (1979) 525; *Nucl. Phys.* **B206** (1982) 333; E. Norman *et. al., Phys. Rev. Lett.* **58** (1987) 1403; T. Hemmik *et.al.*, Phys. Rev. D41 (1990) 2074

[5] K. Gottfried, V. Weisskopf *Concepts of Particle Physics*, Volume I (1984)

[6] D. Griffiths, *Introduction to Elementary Particles*,(1987)

[7] S. Dawson "Susy and Such", *hep-ph/9612229* v2, (1997)

[8] CDF Collaboration, T. Affolder *et. al.*, Phys. Rev. Lett, **84**, 5704 (2000)

[9] ALEPH Collaboration, CERN EP/98-76; Phys. Lett. **B 373** 246 (1996) Updates reported in CERN OPEN-99-330 (1997)

[10] B. Lee, C. Quigg, and H. Thacker, *Phys. Rev.* **D16** (1977) 1519; D. Dicus and V. Mathur, *Phys. Rev.* **D7** (1973) 3111.

[11] A.R. Clark et. al. (DØ Collaboration), Nucl. Instr. and Methods **A315** (1992) 193.

[12] Casey D., Joffe-Minor T. *et. al.* QCD/WZ Ntuples DØ internal note 3124

[13] S. Abachi et. al., Nucl. Instr. and Methods **A338** (1994) 185.

[14] K. Frame, et al., DØ Note 3165, (1997)

[15] I. Bertram, G. Landsberg et. al., DØ Note 2775, (1995)

[16] DØ Collaboration, S. Abachi *et al.*, Nucl. Instrum. Meth A**338**, 185 (1994)

[17] The Physics Analysis Workstation, *http://wwwinfo.cern.ch/asd/paw/,* (1996)

[18] C. Hays,"A Search for New Physics with the 2 Jets + $\not\!\!E_T$ Final State Using Data from Runs 1B + 1C", DØ Note 3769, (2001)

[19] Byron P. Roe, *Probability and Statistics in Experimental Physics*, (1992) Springer-Verlag New York Inc.

[20] Marc Paterno, Guoliang Wang, *http://www-d0.fnal.gov/~clundst/limit.f* (1995)

[21] S. Abachi et. al. "Search for Light Top Squarks in $p\overline{p}$ Collisions at $\sqrt{s}$=1.8 TeV", FERMILAB Pub-95/380-E

[22] http://www-bd.fnal.gov/hq/DOE_2000_McGinnis/DOE_McGinnis/ Slides from a report from the Tevatron beams division to the department of energy.

[23] R. Demina, J. Lykken, K. Matchev, A. Nomerotski "Stop and Sbottom Searches in Run II of the Fervilab Tevatron", FERMILAB-Pub-99/259-T (1999)

[24] S. Ambrosani *et. al*, "Report of the Beyond the MSSM Subgroup for the Tevatron Run II SUSY/Higgs Workshop", hep-ph/0006162 v2 (2000)

[25] G.L. Kane and J.P. Leville, Phys. Lett. **B112**, 227 (1982); P.R. Harrison and C.H. Llewellyn-Smith, Nucl. Phys. **B213**, 223 (1983)

[26] DØ and CDF collaborations: R. Culbertson, Fermilab-Conf-97-277-E, Proc. SUSY97

[27] D.P. Roy, "Higgs and SUSY Searches at LHC", hep-ph/9803421 (1998)

[28] S.Y. Choi, Jae Sik Lee, "S-channel Production of Minimal Supersymmetric Standard Model Higgs Bosons at a Muon Collider with Explicit CP Violation", hep-ph/9909315 v3 (2000)

[29] V. Barger "Supersymmetry vis-a-vis Muon Colliders", hep-ph/9802355 (1998) An invited talk at the Workshop on Physics at the First Muon Collider and at the Front End of a Muon Collider, Fermilab (1997)